A nanophotonic platform for quantum optical integrated circuits

Siampour Ashkavandi, Hamidreza

Publication date:
2019

Document version:
Final published version

Document license:
Unspecified

Citation for pulished version (APA):
Siampour Ashkavandi, H. (2019). *A nanophotonic platform for quantum optical integrated circuits*. Syddansk Universitet. Det Tekniske Fakultet.

A nanophotonic platform for quantum optical integrated circuits

A dissertation presented

by

Hamidreza Siampour Ashkavandi

to

The Faculty of Engineering

in partial fulfillment of the requirements

for the degree of

Doctor of Philosophy

in the subject of

Functional Materials and Nanotechnology

University of Southern Denmark

Odense, Denmark

April 2019

Printed by Print & Sign, University of Southern Denmark, Odense.

Thesis supervisor

Professor Sergey I. Bozhevolnyi

Author

Hamidreza Siampour Ashkavandi

A nanophotonic platform for quantum optical integrated circuits

Abstract

The evolution of the field of computing from electromechanical relay to vacuum tubes, electronic transistors and finally integrated circuits, where billions of transistors can be packed into a single chip, has exponentially sped up the power of information processing. As the age of miniaturization of semiconductor electronic devices is getting closer to the end, new opportunities appear with quantum computing that are not available in the paradigm of classical integrated circuits. This thesis explores new avenues for the implementation of nanoscale functional quantum devices by development of material platforms and nanofabrication techniques for monolithic integration of quantum light sources in chip-based optical circuitry.

First, a top-down nanofabrication technique is developed for deterministic coupling of individual quantum emitters (QEs) into plasmonic waveguide modes. Secondly, a nanophotonic platform based on dielectric-loaded surface plasmon polariton waveguides (DLSPPWs) is demonstrated for investigation of the coupling of QEs embedded in nanodiamonds into plasmonic circuitry from the viewpoint of realizing bright and efficient single-photon sources integrated on a chip. Moreover, new atom-like QEs based on germanium-vacancy centers isolated in crystalline nanodiamonds is investigated, featuring bright zero-phonon optical lines with remarkable energy splitting in the ground state. The large energy split in the ground state implies a potentially longer spin coherence time due to the suppressed phonon-mediated transitions between the lower and upper branches. Finally, a chip-integrated DLSPPW-based cavity is demonstrated to enhance spontaneous emission rate of single photons at the zero-phonon line, opening thereby new perspectives for realizing on-chip quantum-optical networks.

Recommendation

It is the unanimous opinion of the evaluation committee that this work justifies as a suitable basis for the award of the PhD degree.

Date 11th June 2019

Prof. Dr. Oliver Benson	Prof. Dr. Stefan Maier	Dr. Jonas Beermann

Resumé

Den teknologiske udvikling inden for behandling af binær data - fra elektromekaniske relæer til vakuumrør, elektroniske transistorer og endelig integrerede kredsløb, hvor milliarder af transistorer kan pakkes ind i en enkelt chip - har allerede eksponentielt fremskyndet regnekraften i informationsbehandling. I takt med at miniaturiseringen af halvledertransistorers ende kommer nærmere, fremkommer der nye muligheder med kvantecomputere, der ikke er til rådighed i klassiske integrerede systemer. Denne afhandling udforsker nye veje til implementering af funktionelle kvanteanordninger på nanoskala ved udvikling af materialeplatforme og nanofabrikationsteknikker til monolitisk integration af kvantelys-emittere i chipbaserede optiske kredsløb.

Indledningsvis udvikles en top-down nanofabrikationsteknik til deterministisk kobling af individuelle kvanteemittere (QEs) i plasmoniske bølgeleder-tilstande. Næst demonstreres en nanofotonisk platform baseret på dielektrisk ledet overfladeplasmon polariton bølgeleder (DLSPPWs) til undersøgelse af koblingen af QEs indlejret i nanodiamanter i plasmoniske kredsløb for at realisere lyse og effektive enkeltfotonkilder integreret på en chip. Derudover undersøges nye atomlignende QEs baseret på germanium-defekter isoleret i krystallinske nanodiamanter med lyse nulfonon optiske linjer med bemærkelsesværdig energisplitning i grundtilstanden. Den store energisplitning indebærer en potentielt længere spin-sammenhængstid på grund af de undertrykkede fonon-medierede overgange mellem de nedre og øvre grene. Endelig demonstreres et chip-integreret DLSPPW resonans-hulrum for at forbedre spontan emissionsrate for enkeltfotoner på nulfononlinjen, hvorved der åbnes nye perspektiver for kvante nanophotonik generelt og for at realisere sammenkobling mellem enkeltfotoner og spin qubits.

Acknowledgements

I would like to thank my principal supervisor, Prof. Sergey I. Bozhevolnyi, for his support and encouragement. It was certainly a privilege to be his student. He was a powerhouse of positivity with the ability to address difficult workplace situations immediately and keep me fully motivated to deliver results on a regular basis.

I would like to thank Prof. Fedor Jelezko who supervised my project on GeV color centers during my research stay at Ulm University.

I would like to thank Prof. Yaping Dan who supervised my project on single-atom electronics during my studies at Shanghai Jiao Tong University before joining SDU.

Thanks to Prof. V. A. Davydov and Prof. V. N. Agafonov for supplying the nanodiamond samples.

Thanks to Drs. Y. Chen, S. Kumar, S. K. H. Andersen, and A. S. Roberts for the laboratory training sessions in the beginning of my PhD work at SDU Nano Optics. Thanks also to Ms. O. Wang and Dr. P. Siyushev for their assistance in the low-temperature measurements during my visit in Ulm. Thanks to Dr. V. A. Zenin for his input in the near-field measurements. Thanks to Mr. S. Boroviks for supplying the crystalline gold samples. Thanks to Drs. Y. Yang and F. Ding for the valuable discussions in numerical simulations. Thanks to Mr. J. Linnet for his help to translate the abstract to Danish. Thanks also to Ms. J. Holst for her administrative support.

I would also like to thank all of my colleagues at SDU Nano Optics for creating a productive research environment and for all of the inspiring discussions.

Finally, I would like to thank my family for the generous support and beautiful patience during the years away from home.

List of Acronyms

2D/3D	Two-dimensional/three-dimensional
Ag	Silver
APD	Avalanche photodiode
Au	Gold
BS	Beam splitter
CCD	Charge coupled device
CMOS	Complementary metal-oxide-semiconductor
CPP	Channel plasmon polariton
DC	Directional coupler
DLSPP (W)	Dielectric-loaded surface plasmon polariton (waveguide)
DM	Dichroic mirror
EBL	Electron beam lithography
FDTD	Finite-difference time-domain
FEM	Finite-element method
FM	Flip mirror
FWHM	Full width at half maximum
GeV	Germanium-vacancy
GPP	Gap plasmon polariton
HBT	Hanbury Brown Twiss
HOM	Hong-Ou-Mandel
HPP	Hybrid plasmon polariton
HSQ	Hydrogen silsesquioxane
IMI	Insulator-metal-insulator
MIBK	Methyl isobutyl ketone
MIM	Metal-insulator-metal
MOSFET	Metal-oxide-semiconductor field-effect transistor
NA	Numerical aperture
ND	Nanodiamond
NV	Nitrogen-vacancy
PAH	Polyallylamine hydrochloride
PBS	Polarizing beam splitter
PbV	Lead-vacancy
PMMA	Polymethyl methacrylate
QD	Quantum dot
QE	Quantum emitter

QED	Quantum electrodynamics
QE-PW	Quantum emitter-plasmonic waveguide
RBG	Reflecting Bragg gratings
SEM	Scanning electron microscopy
SiO_2	Silicon dioxide
SiV	Silicon-vacancy
SNOM	Scanning near-field optical microscope
SnV	Tin-vacancy
SPP	Surface plasmon portion
TEM	Transmission electron microscopy
TiO_2	Titanium dioxide
TM	Transverse magnetic
VG	V-groove
ZPL	Zero-phonon line

Contents

List of Figures

Citations to Previously Published Work

Portions of Chapters 1-4 have appeared in the following articles:

- "Unidirectional single-photon emission from germanium-vacancy zero-phonon lines: Deterministic emitter-waveguide interfacing at plasmonic hot spots", H. Siampour, O. Wang, V.A. Zenin, S. Boroviks, P. Siyushev, Y. Yang, V.A. Davydov, L.F. Kulikova, V.N. Agafonov, A. Kubanek, N.A. Mortensen, F. Jelezko and S.I. Bozhevolnyi, *arXiv:1903.05446* (2019);

- "On-chip excitation of single germanium vacancies in nanodiamonds embedded in plasmonic waveguides", H. Siampour, S. Kumar, V.A. Davydov, L.F. Kulikova, V.N. Agafonov and S.I. Bozhevolnyi, *Light: Science & Applications* **7**, 61 (2018);

- "Chip-integrated plasmonic cavity-enhanced single nitrogen-vacancy center emission", H. Siampour, S. Kumar and S.I. Bozhevolnyi, *Nanoscale* **9**, 17902-17908 (2017);

- "Nanofabrication of plasmonic circuits containing single photon sources", H. Siampour, S. Kumar and S.I. Bozhevolnyi, *ACS Photonics* **4**, 1879-1884 (2017);

- "Si nanowire phototransistors at telecommunication wavelengths by plasmon-enhanced two-photon absorption", H. Siampour and Y. Dan, *Optics Express* **25**, 4601-4609 (2016).

Chapter 1: Introduction

1.1 Background

Miniaturization of semiconductor electronic devices has been a continues trend in the past 50 years, cramming more components onto a chip at a rate of doubling approximately every two years as described by Moore's law[1,2]. That means computer hardware today is around 2^{31} (2 billion) times as powerful for the same cost, and memory chips store 2 billion times as much data as in 1965. As the size of a miniature electronic component (e.g., transistor) becomes smaller, the intrinsic gate delay (i.e., the time required to switch transistor on or off) becomes shorter and therefore the operating speed of the transistor itself improves[3]. However, the interconnect delay (i.e., the time spent for a signal to propagate from the source to its destination in a chip) increases due to the inherent resistance of the metal interconnects and the capacitance of the dielectric in between the lines (so called RC delays)[4]. Scaling down to the feature sizes below 0.5 μm, the delay time associated with the metal interconnects dominates over the gate delay[4,5], as shown in Figure 1-1. As a result, the operating speed of the electronic devices is limited mainly by the metal interconnects.

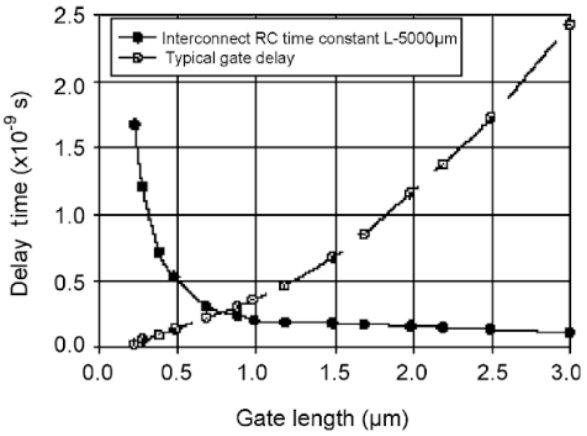

Figure 1-1 Interconnect bottleneck. Contributions of delay times associated with metal interconnects and gate delay for different gate lengths (from ref 4)

One promising solution is to replace the metal interconnects, particularly the metal buses, with on-chip optical waveguides, turning the electronic circuitry into a mixed photonic and electronic system[5,6]. Photonic interconnects offer an enormous bandwidth as compared to metal interconnects, however, the diffraction limit of light in dielectric photonic components prevents the same scaling as in electronics. Utilizing nanoscale photonic components based on plasmonics (a branch of optics that deals with surface plasmons in metals) has a great potential to circumvent the issues associated with the sizing mismatch between conventional photonic waveguides and electronic circuits (see Figure 1-2)[7,8].

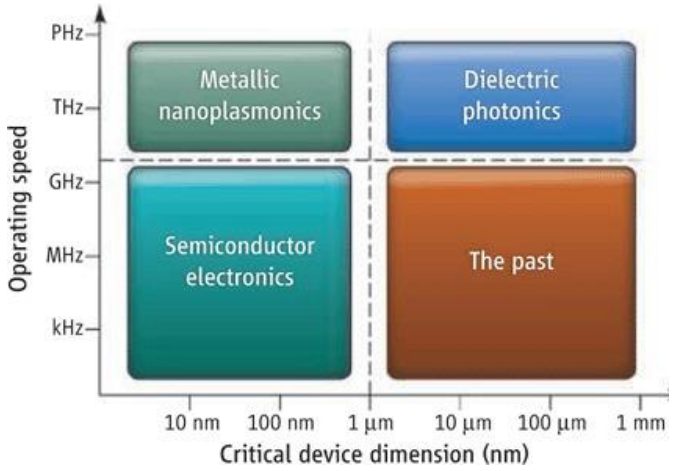

Figure 1-2 Different technologies for chip-scale integrated circuits (from ref 8)

1.1.1 Surface plasmon polaritons – an overview

Surface plasmon polaritons (SPPs) are collective charge oscillations occurring at the metal-dielectric interface due to the interaction between light and free electrons. SPPs enable to confine light to the scales far beyond the diffraction limit, bridging microscale optics to nanoscale electronic components on a chip[7,9,10]. As a simple example, one can consider an infinite flat interface that separates bulk regions of a metal and a dielectric, as shown in Figure 1-3. Following the wave equation in classical electrodynamics[11], one can derive a transverse magnetic (TM) wave propagating along the *x*-axis with the transverse component of the electric field ($\boldsymbol{E}_z$) being $\boldsymbol{E}_z = \boldsymbol{E}_{0z}\exp[i(\beta x - \omega t)]\exp(i\delta|z|)$, where the modulus $|z|$ represents the absolute value of z, $\boldsymbol{E}_{0z}$ is the electric field at $z = 0$, ω is the angular frequency, and δ denotes a complex number with positive imaginary part. The complex wave vector along the direction of propagation is determined by the dispersion relation, with the complex-valued wavenumber being $\beta = k_0\sqrt{[\varepsilon_d\varepsilon_m]/[\varepsilon_d + \varepsilon_m]}$, where ε_d and ε_m are the relative permittivities of the dielectric and metal half spaces, respectively[12]. The propagation length of the guided SPPs, i.e. the length that SPPs propagate along *x*-axis before the power decays to 1/e of its original value, can be obtained as $L_p = 1/[2\mathrm{Im}(\beta)]$, in which $\mathrm{Im}(\beta)$ is the imaginary part of the SPP wavenumber.

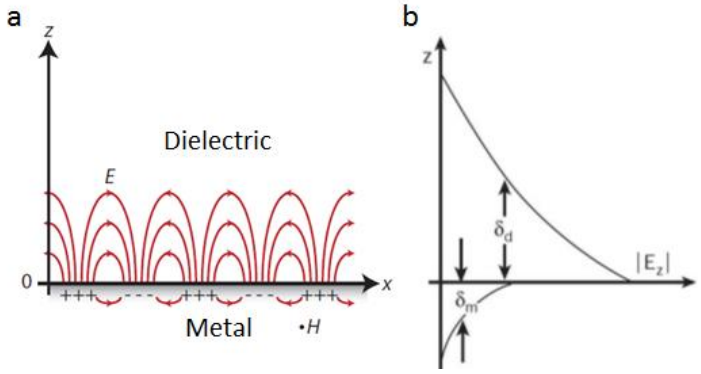

Figure 1-3 Propagating SPPs at the metal-dielectric interface. (a) Electromagnetic TM wave associated with propagating SPPs at the metal-dielectric interface. (b) The field amplitude $|E_z|$ decays exponentially away from the interface.

According to the Drude model, the frequency dependence of the relative permittivity of the metal (ε_m) is given by $\varepsilon_m = 1 - \omega_p^2/[\omega^2 + i\omega\gamma_p]$, where ω_p is the plasma frequency and γ_p is the frequency collision characterizing material losses. Using a simpilfied Drude approximation by ignoring the losses ($\varepsilon_m = 1 - \omega_p^2/\omega^2$), one can imidiately conclude that at frequencies below the plasma frequency ($\omega < \omega_p$), the permittivity of metal is negative, and therfore the electromagnetic wave can not propagate in the bulk metals. With such approximation, the dispersion relation of guided SPPs, i.e. $\beta = k_0\sqrt{[\varepsilon_d\varepsilon_m]/[\varepsilon_d + \varepsilon_m]}$, is derived and shown in Figure 1-4 (red line). The dispersion relation of light in dielectric ($k_d = \frac{\omega}{c}\sqrt{\varepsilon_d}$) is illustrated with a dashed line.

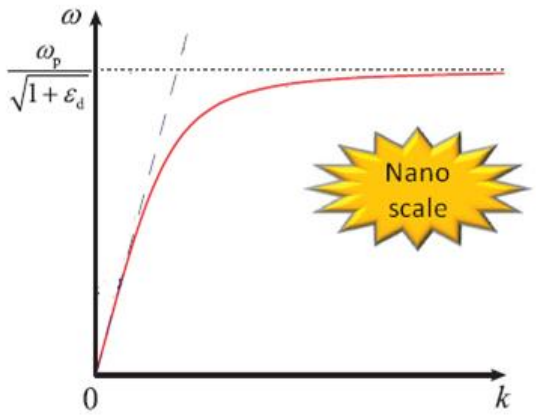

Figure 1-4 SPP dispersion and properties. Surface plasmon dispersion relation for a flat interface (red line). The dispersion relation of light in dielectric is illustrated with a dashed line. The dispersion curve is shown with red line and lies to the right of the dashed line, indicating guided SPP modes. The unique dispersion relation of SPPs, yields extremely high wavenumbers (β) capable of producing nanoscale optical fields.

1.1.2 Plasmonic device-based integrated circuits

Turning the electronic circuitry into a mixed photonic and electronic system requires integrating high-performance photodetectors with complementary metal-oxide-semiconductor (CMOS) transistors for optical and electronic signal conversion. It is known that nanosized photodetectors can achieve high speed but often suffer from low photosensitivity due to the ultra-scaled volume for light absorption. Nanoscale photodetectors integrated with plasmonic antennas can overcome this issue to achieve

high speed and high photosensitivity[13]. The field concentrating abilities of surface-plasmon antennas and nano-sized electronic components ensuring high speed information processing as shown in Figure 1-5(a, c). The advance of such technology requires core-shell pn junctions (see Figure 1-5(b)) formed by self-assembled monolayer doping[14]. The monolayer doping for the Fin structured three-dimensional (3D) metal-oxide-semiconductor field-effect transistors (MOSFETs) is the new technology trend because it can form ultra-shallow junctions to relieve the short channel effect in sub-10 nm MOSFETs[15].

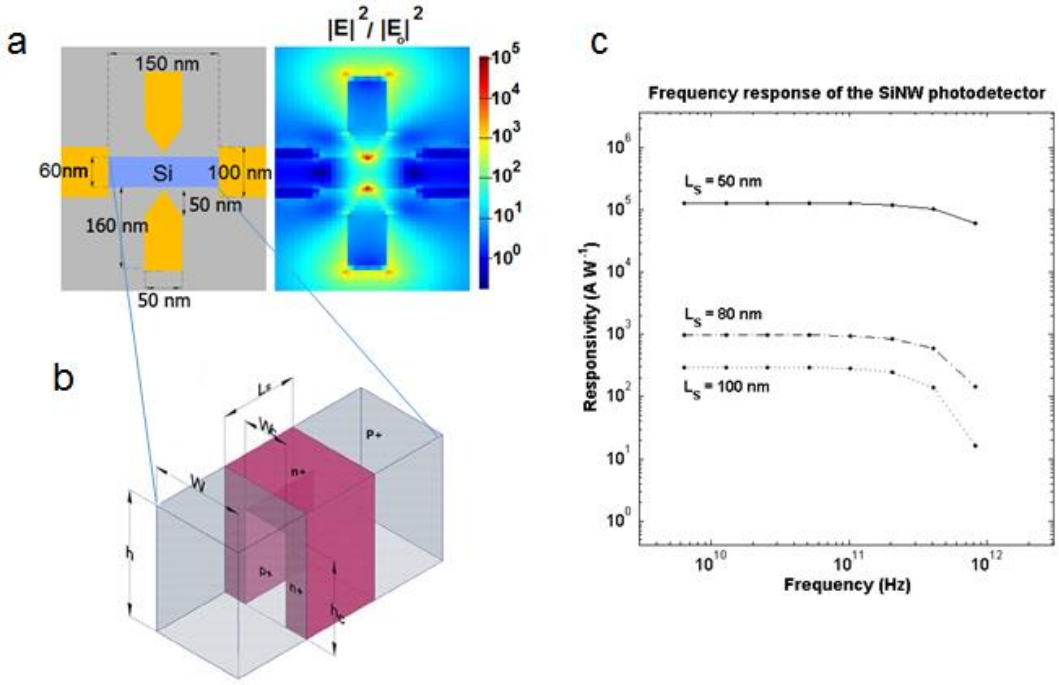

Figure 1-5 Plasmonic antenna enhanced silicon nanowire photosensitivity for high-speed application. (a) Geometrical parameters of the nanowire detector (left); Distribution of normalized light intensity $|\mathbf{E}_2|^2/|\mathbf{E}_0|^2$ at the half thickness of the nanowire, where $\mathbf{E}_0$ is the electric field intensity of the incident light. (b) Schematic of the core-shell silicon nanowire phototransistor. The n-type shell and p-type core structure makes a weakly depleted p-channel inside the nanogap. (c) Frequency response of the silicon nanowire phototransistors. The incident light intensity is 0.1 mW cm^{-2} and the bias voltage is fixed at 2 V (from ref 13).

1.1.3 SPP-based waveguides

With the ever-increasing demands for miniaturization of photonic components and circuits on a chip, various types of SPP-based waveguides, such as insulator-metal-insulator (IMI)[16], metal-insulator-metal (MIM)[17], dielectric-loaded surface plasmon polariton (DLSPP)[18-21], gap plasmon polariton (GPP)[22], channel plasmon polariton (CPP)[23], wedge SPP[24,25], and hybrid plasmon polariton (HPP)[26,27], have been proposed for demonstrating radiation guiding at the nanoscale[28] (see Figure 1-6). Realization of highly integrated plasmonic circuits requires confinement of guided SPP modes to the subwavelength cross sections (mode area) and with low dissipations (propagation loss)[29,30]. In order to accommodate as many plasmonic devices as possible within a certain work plane, one should also consider the lateral crosstalk and bending loss. In order to have a direct relation to the maximum number of components that can be integrated on a chip within an area limited by the propagation length (L_p) associated with SPP waveguide mode, one can define a figure of merit (FOM) as FOM = $[\lambda_0 L_p^2]/[n_e w_0^3]$. This definition, takes into account the lateral mode width, w_0, effective mode index (n_e) as well as the guided mode wavelength (λ_0/n_e)[28]. The possibility of strong subwavelength localization of SPP waveguide modes makes these structures particularly useful for the future design and development of highly integrated and efficient optical signal-processing devices, all-optical switches and integrated photonic circuitry[28].

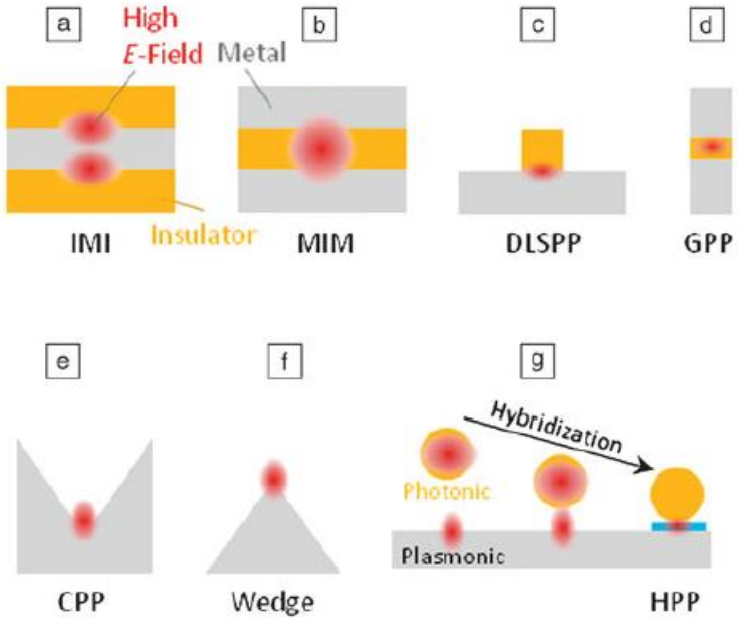

Figure 1-6 Various types of plasmonic waveguide configurations for highly integrated optical circuitry. (a-g) The waveguide cross-sections are shown, and the SPPs propagate in the third direction (from ref 31).

1.1.4 Quantum optical circuitry with surface plasmons

As the age of miniaturization of semiconductor transistors is getting closer to the end (as we cannot make a transistor smaller than an atom), new opportunities appear with quantum computing that are not available in the classical paradigm of integrated systems (as shown in Figure 1-7)[32]. In this new paradigm, the computations are carried out based on the quantum principles of matter. The key ingredients of quantum information processing are coherent superposition of states and entanglement, for which we have access to a larger information space in between simple 0 and 1 classical bits, and whereby we can process information in a parallel fashion, offering an exponential speed-up for certain computational problems (so called quantum speed up)[33]. In order to have this new technology being chip-based, similar to what we have in the case of electronics, we would like to make our functional quantum optical devices as small as possible and this will bring us to the field of quantum plasmonics[34-37].

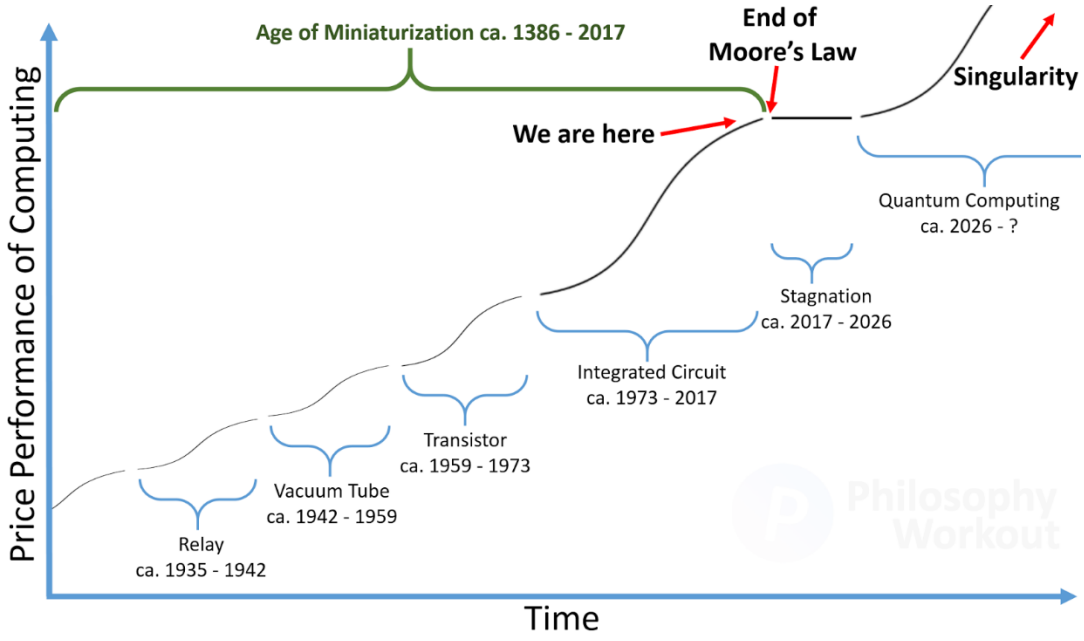

Figure 1-7 Computing beyond Moore's law (from ref 38)

It has been shown that strongly confined SPP modes can be efficiently excited by quantum emitters (QEs)[35,36,39-43]. Moreover, the quantum information encryption survives the photon-to-plasmon conversion, plasmon propagation and plasmon-to-photon conversions[42,44-46]. This has been demonstrated for single photons[44], entangled photons[45] and quadrature squeezed light[46]. Plasmonic circuitry has also been utilized for quantum interference and observation of Hong-Ou-Mandel (HOM) effect[47]. A number of plasmon-based platforms such as V grooves, wedge waveguides, slot waveguides that have been demonstrated for quantum optical circuitry are illustrated in Figure 1-8.

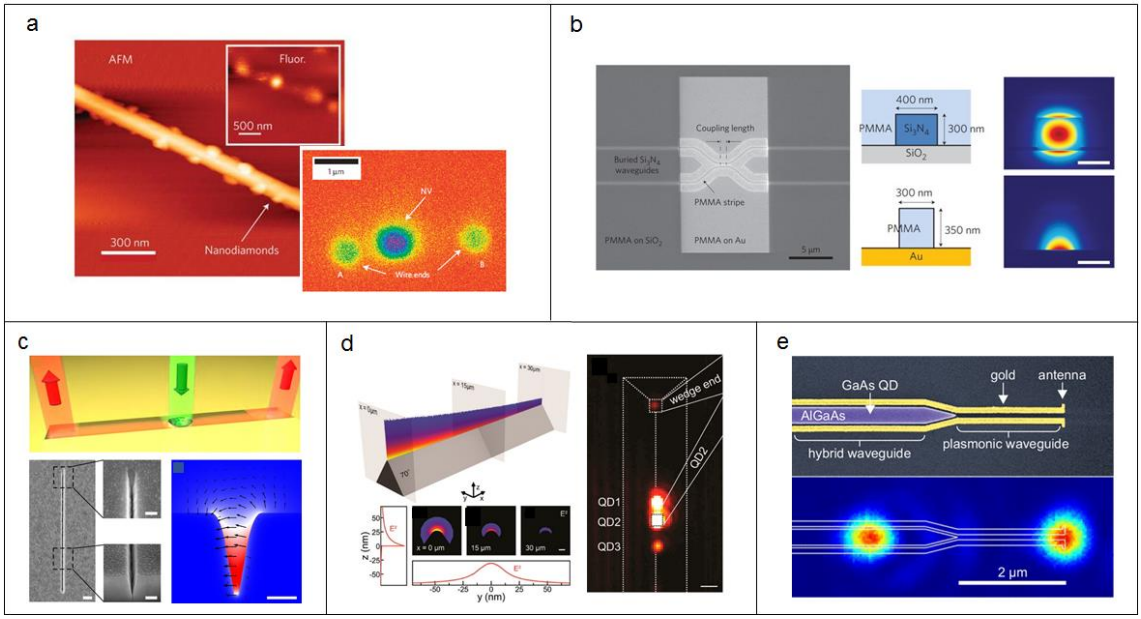

Figure 1-8 Plasmon-based quantum optical circuitry. (a) Wave-particle duality of single plasmons excited by a single nitrogen-vacancy (NV) center in nanodiamond (ND) coupled to a metallic nanowire (from ref 41). (b) The HOM experiment with surface plasmons (from ref 47). (c) Coupling of single NV centers to channel plasmons (from ref 43). (d) Quantum dots (QDs) coupled to plasmonic wedge waveguides (from ref 48). (e) Single-plasmon nanocircuit driven by a self-assembled QD (from ref 49).

The most important challenge in exploiting nanoplasmonic circuitry for quantum-optical networks is inevitable SPP propagation loss by absorption (ohmic loss). High transparency of dielectric waveguides facilitates information transport over long distances but the corresponding waveguide modes are diffraction-limited in their cross sections[8]. DLSPP waveguides that confine SPPs laterally by using dielectric ridge waveguides patterned on a flat metal film support guided modes and can also serve as a bridge between nanoplasmonic components and dielectric waveguides[19,21,50,51]. In addition, DLSPP waveguides can be fabricated using standard lithography process, as opposed to V-groove based plasmonic waveguides supporting CPPs or wedge waveguides that can have similar low losses, but require advanced fabrication techniques, such as focused ion beam milling[43,48,52]. Furthermore, to accurately position QEs in the vicinity of plasmonic structures or high-index dielectric waveguides, scanning probe

manipulation is often used, which can be time-consuming and difficult in incorporation of several single emitters in an integrated circuit[43,53-56].

1.2 Outline of thesis

The thesis is divided into five chapters. After this introduction and problem formulation, Chapter 2 explores the major lines of research on diamond color centers and their abilities for scalable implementation in solid-state configurations while insuring long coherence times in atomic systems. In particular, new atom-like QEs based on single germanium-vacancy (GeV) centers isolated in crystalline NDs is presented, featuring bright zero-phonon optical lines with remarkable energy splitting in the ground state. In Chapter 3, a top-down nanofabrication technique is proposed and demonstrated based on DLSPPW platform, allowing for efficient coupling of individual QEs in NDs on a single chip. The ability of this system to realize efficient single-photon transmission is quantified by a figure of merit (FOM) and compared with other hybrid quantum optical plasmonic systems. In Chapter 4, a chip-integrated photonic crystal cavity based on DLSPPWs is demonstrated, enabling to enhance the spontaneous emission rate of single photons at the zero-phonon line (ZPL), and improving spectral purity of the coupled emitters. The cavity structure is employed to modify NV, silicon-vacancy (SiV) and GeV emissions. Finally, Chapter 5 recapitulates the major findings of the thesis, and frames them into the perspective of potential future investigations.

Chapter 2: Solid-state sources of single photons

2.1 Single photon qubits

Single photon sources are central building blocks for future quantum technologies such as quantum computers, information processing, communications, and sensing[57]. The quantum state of single photons can be stored[58,59], read out[60], manipulated[61] and transmitted[62] in the form of qubits that are defined as the quantum analog of the bits in a classical computer[63,64]. Unlike a classical binary bit that is characterized by one of two levels of a semiconductor transistor output as either 0 or 1, a qubit can be a coherent superposition of both levels simultaneously[63]. A quantum superposition can be physically realized with a two-state system (e.g., the polarization of a single photon in which the two states can be taken to be the vertical polarization and the horizontal polarization), or a two-level system (e.g., the spin of the electron in which the two levels can be taken as spin up and spin down). In quantum theory, because of entanglement, a general superposition of 2^n levels may be represented in n two-level systems. Thus, the amount of the physical resource (that defines the levels) will grow only linearly with n (i.e. the number of two-level systems). This is opposite to the case of classical states for which the amount of the physical resource needed will grow exponentially with n, offering an exponential speed-up for certain computational problems in quantum algorithms over

classical algorithms[65-67]. Furthermore, quantum entanglement ensures the security of communications because any attempt to intercept the photons in transit would be immediately obvious to those monitoring the state of the other photons in each pair[68].

2.2 Photon antibunching and indistinguishability

An ideal single-photon source emits exactly one photon at a time and all photons are identical (indistinguishable photons)[69]. As a result, if a single photon beam is split between two paths can only be detected in one of them. This fact has been used in a Hanbury Brown Twiss (HBT) experiment to characterize single-photon sources. As shown in Figure 2-1, the HBT setup consists of two photon detectors placed at equal distances behind a 50/50 beam splitter (BS). In this experiment, the autocorrelation function, defined as $g^{(2)}(\tau) = \langle I_1(t) I_2(t+\tau)\rangle / \langle I(t)\rangle^2$, determines at which rate multiple photons are emitted with respect to the rate at which single photons are emitted. In the relation, $I_i(t)$ denotes the intensity at time *t* and at place *i*, and the brackets represent the average over time. The degree of antibunching can be measured by the equal-time intensity autocorrelation factor (zero delay time $\tau = 0$), which is related to the photon number (n) statistics[70] according to $g^{(2)}(0) = \langle n(n-1)\rangle / \langle n\rangle^2$. Light is said to be bunched if $g^{(2)}(\tau) < g^{(2)}(0)$ (i.e. for the field to be classical), and antibunched if $g^{(2)}(\tau) > g^{(2)}(0)$ (nonclassical light). For a true single photon source we have $g^{(2)}(0) = 0$.

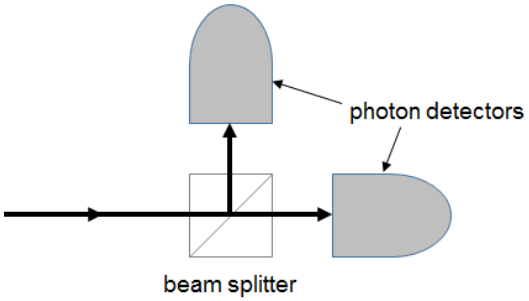

Figure 2-1 The HBT setup for characterization of single-photon sources.

The experiment to test indistinguishability of photons consists of a Michelson interferometer setup as shown in Figure 2-2. If two indistinguishable photons enter a

50/50 BS from opposite sides both photons need to leave the BS together according to the quantum mechanical prediction[71,72]. This effect is reffered to as the 'bunching' of photons, in contrast to the HBT experiment for measuring $g^{(2)}(0)$ (antibunching experiment) in which photons are supposed to leave the single photon emitters one by one[72-74].

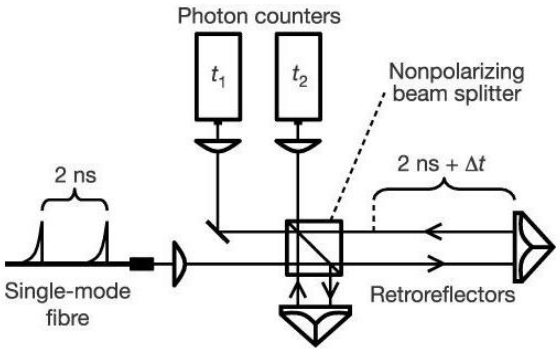

Figure 2-2 The Michelson interferometer setup for testing indistinguishability of photons. The long arm on the right is 2 ns longer than the short arm on the bottom. When the first photon follows the long arm and the second photon follows the short arm of the Michelson interferometer, both should leave to one of the photon detectors (i.e., they should bunch), leading to two-photon interference (from ref 71).

2.3 Quantum coherence and environmental disruptions

The length of time that a quantum superposition state can survive called the quantum coherence time. When a quantum system is not perfectly isolated, coherence is shared with the environment and appears to be lost with time, a process called quantum decoherence[75]. The key challenge here is the environmental disruptions that cause a quantum superposition to dissipate, similar to energy that appears to be lost by friction in classical mechanics[76]. Scientists are therefore exploring different approaches whereby a quantum state lives longer than it takes to perform an operation or experiment. One approach is to design complex containers that completely isolate quantum states from the surroundings, while still allowing for state manipulation. For example, the use of isolated atoms in ultra-high vacuum chambers can protect a quantum state from the destructive environment[74,77]. Another way is to remove the environmental disruptions by cooling

down to cryogenic temperatures and thereby freeze out much of the noisy surroundings in solid-sate systems[78].

2.4 Atom-like quantum emitters in diamond

Combining isolated atoms with nanophotonic systems is a powerful approach to strongly enhance the atom-photon interaction due to a large cooperativity associated with nanoscale photonic devices, although trapping atoms in tightly focused laser beams (optical tweezers) imposes serious technical challenges[79-81]. Alternatively, an all solid-state approach has been developed, in which naturally trapped "atoms" (e.g., QDs) are coupled, created and multiplexed on a single chip[82]. Despite the progress made for deterministic positioning of QDs on a single chip[42,83-85], some challenges remain due to a relatively short coherence time available with QDs (in nanosecond range)[86], resulting in the quantum information being typically lost before reaching distant quantum nodes. Further search for configurations insuring long coherence times in atomic systems and allowing for scalable implementation in solid-state systems led to the exploration of diamond crystals containing artificial "atoms" (so-called color centers)[87]. Starting with a NV center (i.e., substitutional nitrogen-atom impurity next to a diamond lattice vacant site as shown in Figure 2-3(a)), remarkable coherence time (in millisecond range)[88] has been reported, making it an ideal emitter for spin physics and metrology[89]. NV centers are known to be stable and bright single-photon sources that also have an optically accessible electron and nuclear spin that can be used as qubits[69,89-91]. Figure 2-3 shows schematic of the three level structure of the NV center in diamond lattice. The negatively charged state NV center forms a spin triplet in the orbital ground state, and allows for optical initialization and readout at room temperature[89].

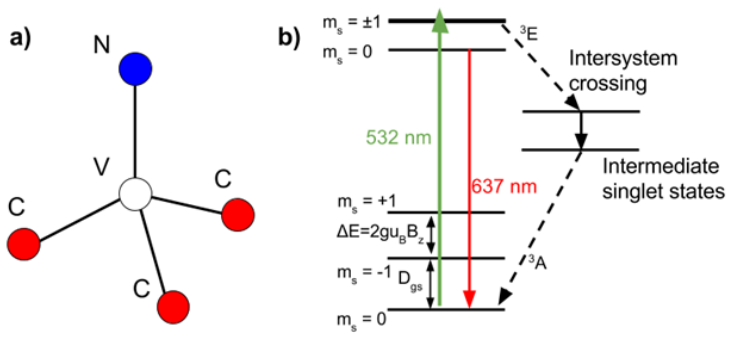

Figure 2-3 NV center in diamond. (a) Structure of the NV defect center in diamond. (b) The energy level scheme (from ref 92).

Using confocal fluorescence microscopy (see setup in Appendix A.2), optical characterizations performed at room temperature for a ND containing a single NV center. Florescence spectrum, autocorrelation and lifetime measurements shown in Figure 2-4 indicated a single NV center in ND. The lifetime data and $g^2(\tau)$ function were fitted to a double exponential function as explain in ref 91.

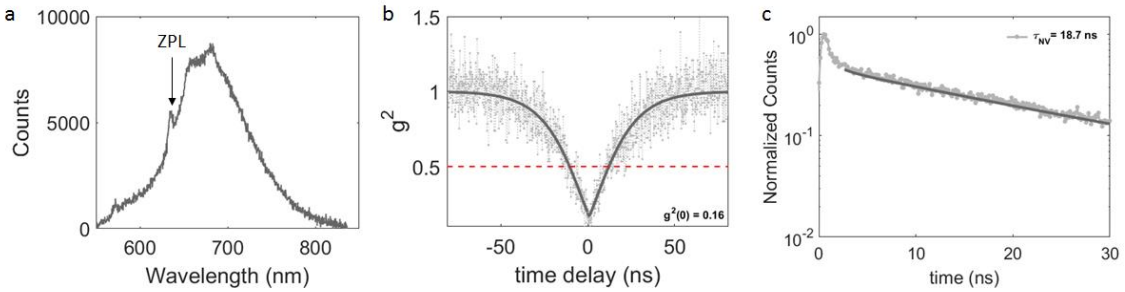

Figure 2-4 Measurement results for a single NV center embedded in ND. (a) Florescence spectrum, (b) autocorrelation and (c) lifetime measurements.

As shown in Figure 2-4(a), the coherent part of the NV emission is limited severely, with the emission to the ZPL (637 nm) being only 4%. Furthermore, a lack of symmetry in NV molecule structure (shown in Figure 2-3(a)) makes the frequency of optical transitions being very sensitive to the environment due to the non-zero permanent electric dipole of obital states in the NV system[93,94]. Replacing nitrogen with larger atoms of group IV in the periodic table (e.g., with a silicon atom that is ~1.5 times larger in size than a carbon atom) enabled to circumvent the issues associated with symmetry

arguments[95-100]. For the new system, due to the inversion symmetry as shown in Figure 2-5(a), orbital states have vanishing permanents dipole and therefore optical transitions (shown in Figure 2-5(b)) are insensitive to external E-field. This opened a way toward demonstrations of indistinguishable solid-state QEs (without the need for electric field tuning) with spectral stability and large ZPLs[94,101]. Schematic of the zero-phonon optical transition lines for a SiV color center is shown in Figure 2-5(b). Internal transitions of B and C are parallel in polarization and orthogonal to the external transitions of A and D, resulting in an emitter with two orthogonal dipoles[99,102].

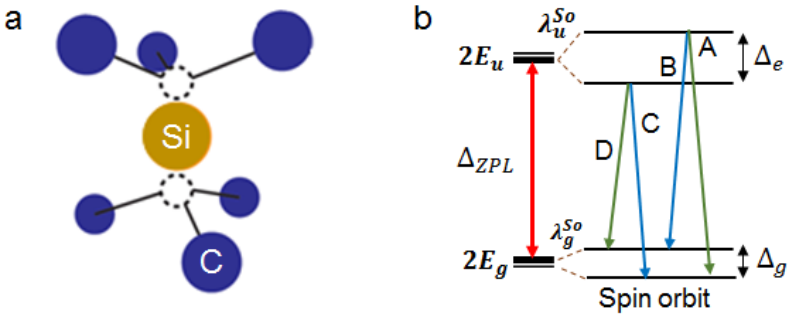

Figure 2-5 SiV center in diamond. (a) The Si atom is located in the middle of two empty lattice sites, which includes inversion symmetry. (b) Electronic structure and optical transitions of the SiV center. Optical transitions B and C have polarization axes parallel to the symmetry axis of the system, and transitions A and D are perpendicular to the symmetry axis, indicating that the SiV emitter has two orthogonal dipoles[99,102].

The structural symmetries in SiV leads to spectrally narrow emission as shown in Figure 2-7(b), with a large zero-phonon emission (70%) at 737 nm. However, phonon-mediated transitions between the lower and upper branches in the ground state limits the spin coherence time of the SiV emitters at room temperatures and even at 4 Kelvin. Further cooling down to the sub-Kelvin regime, or strain engineering has been reported for potential solutions[103-105]. Another approach is to use larger atoms of group IV such as germanium[96,104], tin[97], or lead[106] atoms to achieve a longer spin coherence time even at a high temperature due to a larger energy split in their ground states as shown in Figure 2-6.

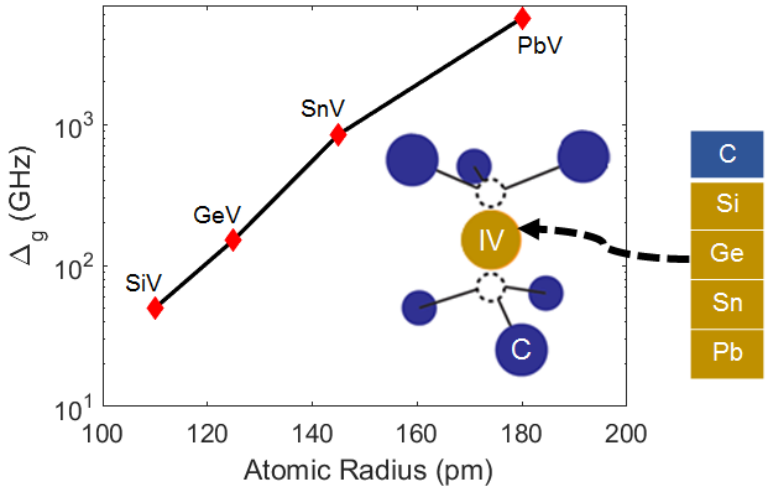

Figure 2-6 Color centers in diamond crystals with structural symmetries. The defect atom in group IV (silicon, germanium, tin, or lead) is placed between two diamond lattice vacant sites, resulting in a split-vacancy color center (SiV, GeV, tin-vacancy (SnV), or lead-vacancy (PbV)) with spectral stability as a result of its inversion symmetry. The larger atom exhibits larger energy split in the ground state (Δ_g) for group IV color centers in diamond and potentially a longer spin coherence time. The values of Δg for color centers in bulk diamond, including SiV[99], GeV[96], SnV[97] and PbV[106], were adapted from the experimental results reported for the corresponding vacancies.

2.5 Color centers in nanodiamonds (NV, SiV and GeV)

Due to a high refractive index of diamond ($n \sim 2.4$), the efficiency of photon out-coupling from diamond color centers in bulk crystals is very limited[87,96,97,107-109]. Having such single-photon sources in NDs is particularly important since it can enable engineering of hybrid quantum plasmonic systems. The SiV centers exhibit an optical transition at a longer wavelength (ZPL at 737 nm) operating with smaller SPP loss in the metal[110]. At the same time, the SiV excited state decay is dominated by the nonradiative relaxation, causing lower quantum efficiency for SiV centers[111]. More recently, GeV centers in diamond, with zero-phonon emission at 602 nm (Figure 2-7(b)), have shown stronger coupling between emitters and photons than SiV due to their higher quantum efficiency and larger absorption cross section[96].

Progressing towards bright and efficient nanometer-sized solid-state single-photon sources, a new investigation of atom-like QEs based on GeV centers isolated in crystalline

NDs is presented in this thesis. Diamond crystals were grown at the scale of nanometer, under a high-pressure high-temperature (HPHT) condition. Ge defect atoms were added during the growth in a hydrocarbon metal catalyst-free system based on homogeneous mixtures of naphthalene $C_{10}H_8$ with tetra-phenylgermanium $C_{24}H_{20}Ge$ (see details in Appendix A.1). A scanning electron microscopy (SEM) image of the GeV nano and microdiamonds in the 'raw' sample after HPHT synthesis is shown in Figure 2-7(a). The inset shows a transmission electron microscopy (TEM) image of the GeV-NDs of different sizes (from 20 to 120 nm).

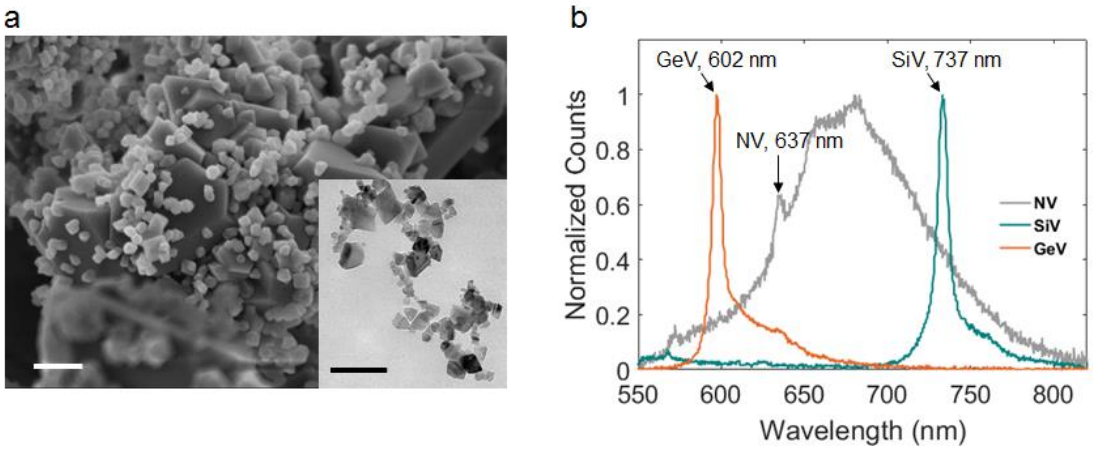

Figure 2-7 Color centers in NDs. (a) SEM image of the GeV nano and microdiamonds performed on the 'raw' sample (after HPHT synthesis). Inset shows a TEM image of the GeV-NDs of different sizes taken after the chemical and ultrasonic treatment. The scale bars are 100 nm. (b) Fluorescence spectrum taken from a GeV-ND at room temperature compared with NV- and SiV-NDs.

In the experiment, the synthesized GeV-NDs were spin coated onto a Ag-coated silicon substrate. A 1-nm layer of polyallylamine hydrochloride (PAH) was put on the Ag layer to improve the distribution and attachment of the NDs to the Ag surface[112]. The sample was then raster scanned using confocal fluorescence microscopy. In Figure 2-9(a-d), Flurescence spectrum, lifetime, autocorrelation, and saturation curve measurement results are shown at room temperature for the single GeV-NDs on the Ag film. The results indicate ultrabright, spectrally narrow and stable single photon sources in the NDs. In Figure 2-8(c), the polarization characteristics of a single GeV-ND is illustrated. An analyzer in the detection pathway was used to determine the projection of polarization

axes of single photons emitted on the surface plane (see the experimental setup in Appendix A.2). The measured polarization data are well-fitted to the model of two orthogonal dipoles, following the polarization characteristic of the group-IV colour centers[95,99].

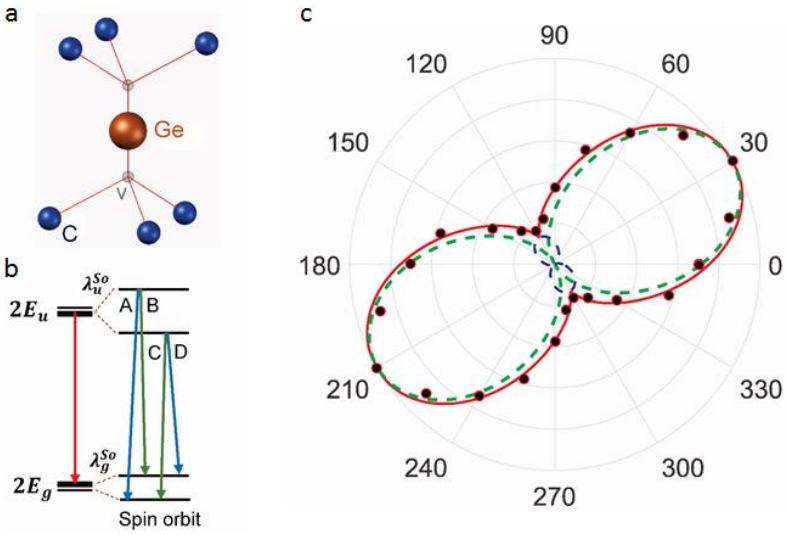

Figure 2-8 GeV in diamond. (a) The Ge atom is located in the middle of two empty lattice sites, which includes inversion symmetry. (b) Electronic structure and optical transitions of the GeV center. Optical transitions B and C have polarization axes parallel to the symmetry axis of the system, and transitions A and D are perpendicular to the symmetry axis, indicating that the GeV emitter has two orthogonal dipoles. (c) Normalized photon rate for a single GeV-ND on the Ag plane versus analyzer angle, measured (dot) and model fit (solid). Dashed curves indicate contributions of the two orthogonal dipoles.

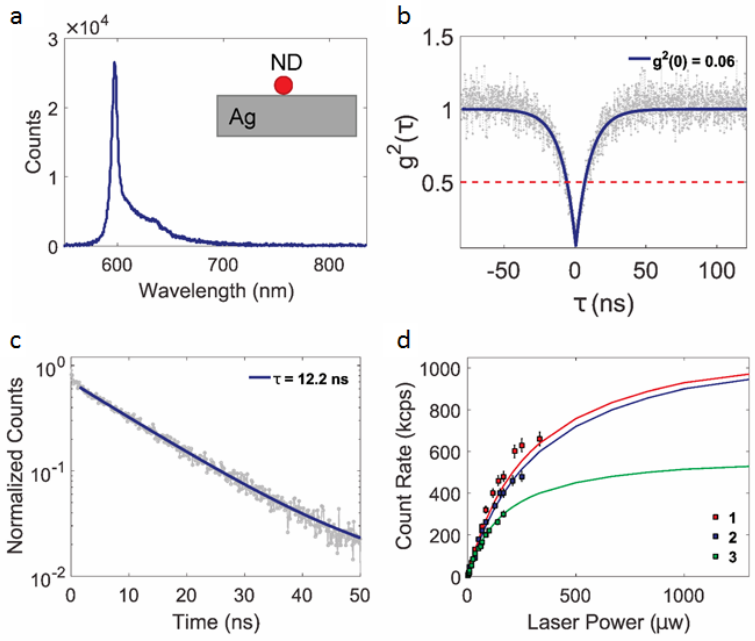

Figure 2-9 Characterization of GeV-NDs. (a) Fluorescence spectrum, (b), second-order correlation (c) and lifetime (g) measurement results taken for a single GeV-ND. The integration time on the spectrum is 300 s, and the excitation power is 10 μW. (d) Saturation curves are taken for three different single GeV-NDs on the Ag-coated substrate that are fitted to the model of $I=I_\infty \cdot P/(P+P_\infty)$, where I_∞ and P_∞ are saturated intensity and saturated power, respectively. The measured data indicate ultra-bright single photon sources based on GeV centers in NDs.

For the experiment at low-temparatures, colloidal gold (Au) crystals were grown on a silicon substrate using a thermolysis synthesis technique[113] (see details in Appendix A.3). The GeV-NDs were deposited on the substrate afterwards. The sample was then loaded on the cold-finger of a continuous flow helium cryostat, which was cooled to 4.7 K for confocal microscopy measurements (see cryogenic setup in Appendix A.2, Figure A-4). Fluorescence image was taken from a crystalline Au flake on which NDs containing single GeV centers were deposited. A single GeV emitter was selected based on fluorescence spectrum and autocorrelation measurements.

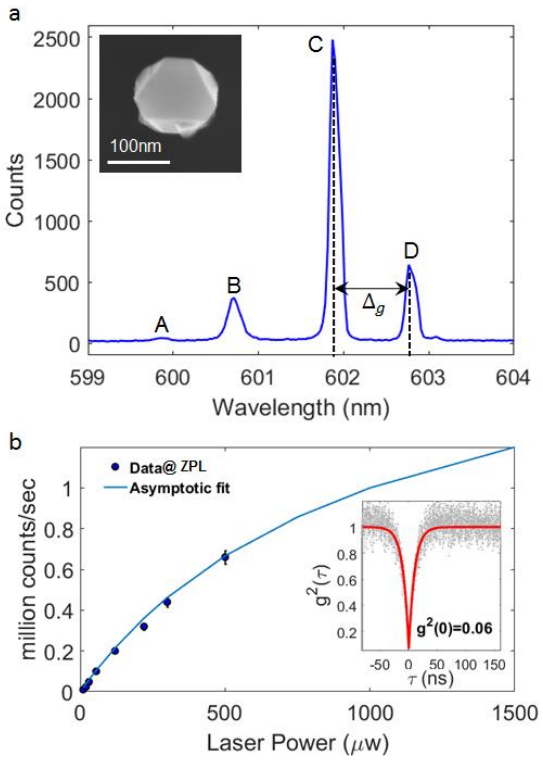

Figure 2-10 Cryogenic characterization of a single GeV in ND. (a) Spectrum taken at a cryogenic temperature exhibits four-line fine structure at around 602 nm similar to bulk crystals, but with ~6 times larger ground state splitting of Δ_g=870 GHz (c). Inset shows SEM image of the ND. The temperature of the ND was calculated to be ~40 K using Boltzmann statistics[114], which is higher than the temperature of the cryostat cold finger due to the limited thermal conductivity of the substrate (silicon). (d) Power dependency measurements indicates ultrabright ZPLs (exceeding 1 million counts per second at 1mW). Saturation curve was fitted to an asymptotic function, indicating a 15-fold enhancement in the brightness compared to those reported for bulk diamonds[115]. Inset shows strong antibunching dip in autocorrelation measurement ($g^2(0) = 0.06$), which implies single photon emission. The red line represents a single exponential fit[96].

Cryogenic characterization shows symmetry-protected optical transitions for the synthesized GeV centers in NDs as shown Figure 2-10(a). Furthermore, ZPLs indicate a large splitting in the ground state (up to 870 GHz), which is 17 times larger than SiV[99,109], and 6 times larger than GeV in bulk[96,104,115], becoming close to SnV with 850 GHz[97]. In general, having SiV and GeV centers in NDs results larger energy split in the ground state compared to bulk diamonds (as shown in Figure 2-11) due to the strain conditions in nanocrystals. The larger energy split in the ground state implies a potentially longer spin

coherence due to the suppressed phonon-mediated transitions between the lower and upper branches[97,116]. Power dependency measurements at low temperature (shown in Figure 2-10(b)) exhibit ultrabright single photon count rates (> 2×10^6 counts/s at saturation) at ZPLs (i.e., ex-cluding phonon sideband) with clean single photon emission (strong antibunching dip of $g^2(0) = 0.06$).

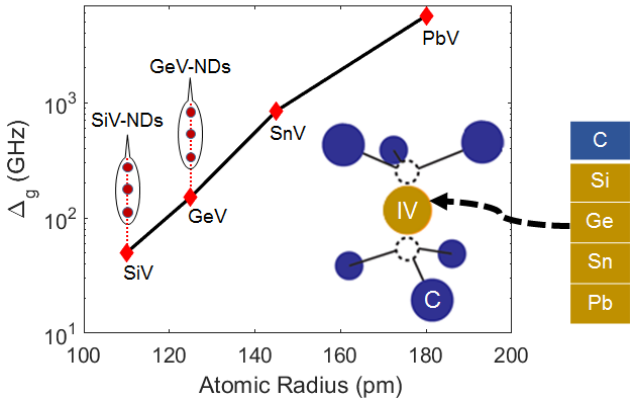

Figure 2-11 The ground state splitting of GeV-NDs compared to other group IV color centers. The values of Δ_g for color centers in bulk diamond, including SiV[99], GeV[96], SnV[97] and PbV[106], were adapted from the experimental results reported for the corresponding vacancies. The ground state splitting data for SiV-NDs were adapted from ref 102.

Chapter 3: Coupling of individual quantum emitters on a single chip

3.1 Atom-photon interactions

Efficient interfaces between single atoms and single photons are essential ingredients for building quantum optical networks, where atomic nodes (QEs) are linking together via flying photons (qubits)[117,118]. The key challenge here is to engineer atom-photon interactions in order to have control over individual QEs on a large scale. Combining isolated atoms with nanophotonic systems is a powerful approach to strongly enhance the atom-photon interaction due to a large cooperativity associated with nanoscale photonic devices[79-81]. In this approach, one can trap the atoms in tightly focused laser beams (optical tweezers) and bring them close to a nanophotonic cavity structure to confine the photons to a small mode volume and thereby to interact strongly with the atoms. Alternatively, an all solid-state approach has been developed, in which naturally trapped "atoms" (e.g., QDs) are coupled, created and multiplexed on a single chip[42,82-85]. Different techniques have been developed for deterministic positioning of QDs and NDs on a single chip[42,83-85]. In one approach, AFM tip was used to manipulate nanocrystals (e.g., NDs) containing QEs in order to make a hybrid emitter-waveguide or emitter-antenna plasmonic system[119]. One could also manage to develop deterministic coupling of site-

controlled QEs in two-dimensional (2D) materials for integration in quantum photonic networks[84]. Alternatively, electron beams have been used to excite QEs, and simultaneously in-situ electron beam lithography (EBL) for integration to photonic circuitry. In Figure 3-1, these techniques are compared in terms of controllability and scalability.

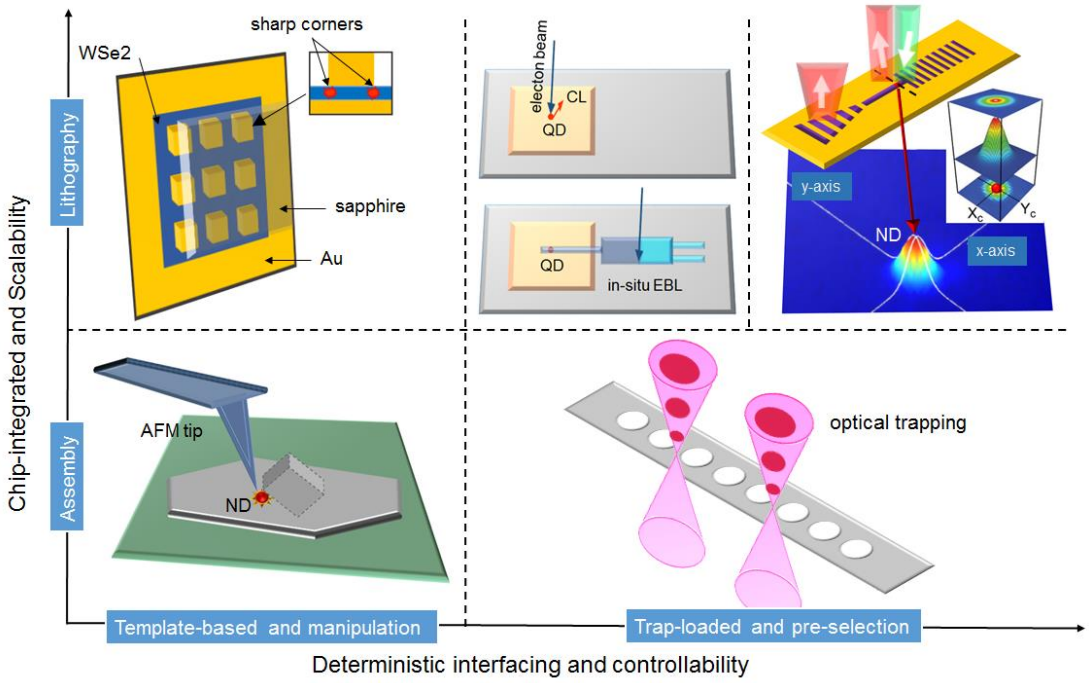

Figure 3-1 Deterministic photonic integration techniques for coupling of individual QEs in a single chip.

3.2 Top-down nanofabrication technique for deterministic integration

In this PhD thesis, an aligned lithography method is developed for accurate positioning of plasmonic waveguides on a single chip in order to have deterministic emitter-waveguide coupling at single-photon level. This technique is compatible to conventional top-down fabrication processes and enables the incorporation of several emitters. Even though two-step fabrication requires extremely accurate alignment, it has a great potential to realize fully scalable on-chip circuits for quantum applications. Positioning of QEs with respect to the coordinates of the markers, and deterministic placement of a waveguide embedding a pre-selected QE is illustrated in Figure 3-2. Figure 3-2(b) and

Figure 3-2(c) show fluorescent image from the emitter and the corresponding Gaussian fits for locating *x* and *y* position, respectively.

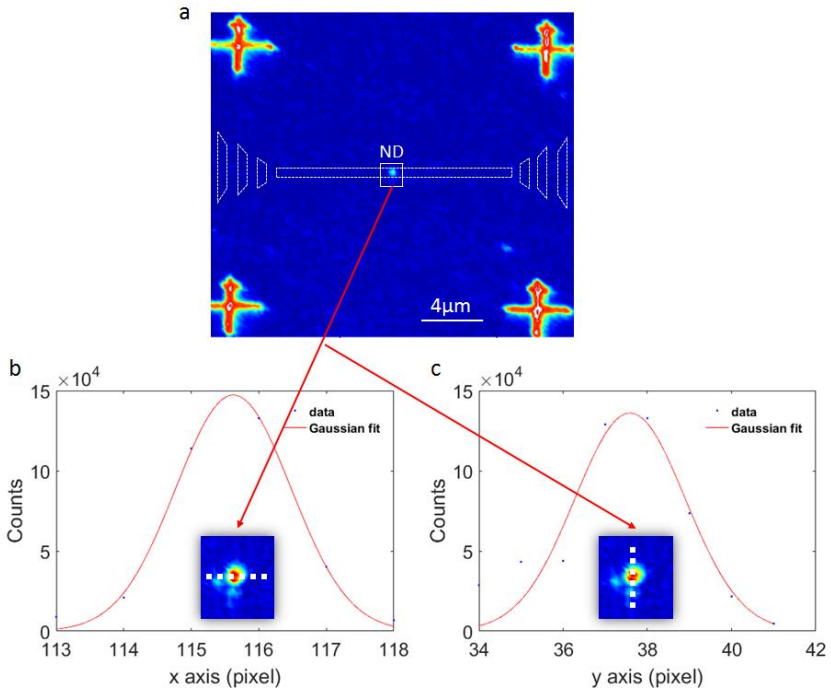

Figure 3-2 Controlled placement of plasmonic waveguides. (a) Fluorescence image from a selected region of the sample defined by four cross markers. The spot inside the square indicates a single QE. White dashed lines indicate location of a waveguide for a pre-determined ND. (b, c) Positioning of *x* and *y* coordinates for the QE using Gaussian fits.

3.3 Coupling of a single NV center into DLSPPW mode

Utilizing the top-down fabrication technique, DLSPP waveguides are built with nanometer precision around single emitters in NDs, whose locations are related to specifically designed and fabricated coordinate markers, using electron-beam lithography of hydrogen silsesquioxane (HSQ) resist spin-coated on a Ag layer (Figure 3-3). The NDs were pre-characterized to contain a single NV center, that is, to be a single photon source.

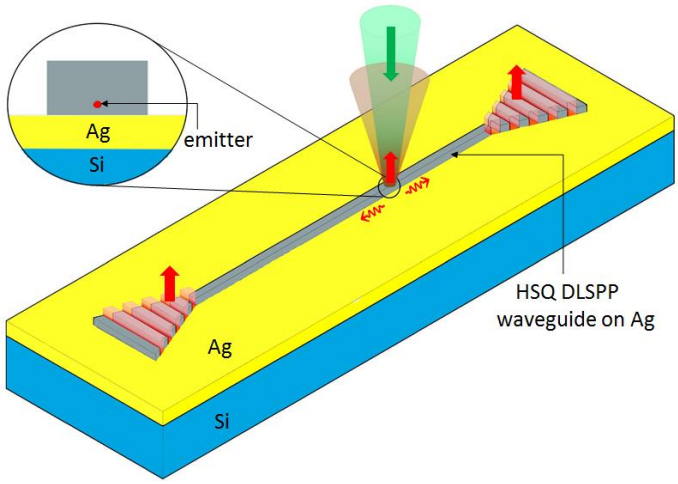

Figure 3-3 Schematic of the device layout and working principle. A preselected ND containing single NV emitter is embedded in a dielectric nanoridge waveguide fabricated atop Ag layer. Green laser light was used to excite the NV center. The excited NV center emits single photons and drives single plasmons propagating along the waveguide and outcoupled from output grating ends.

In the experiment, a silicon sample was coated with a silver (Ag) film of 250 nm thickness, on which Au markers were made, and subsequently, NDs (Microdiamant MSY 0−0.05 μm GAF) were spin coated. The sample was then characterized by scanning in a fluorescence confocal microscope. A detailed description of the experimental setup is available in Appendix A.2 (Figure A-2). In Figure 3-2, cross markers and a preselected ND can be observed from the fluorescence image obtained from confocal microscopy. Lifetime, spectrum, and correlation measurements were taken for the NDs. HSQ e-beam resist (Dow Corning XR 1541−006) was then spin coated (1200 rpm, 1 min) to make a 180 nm film on the Ag surface. Waveguide was fabricated using EBL onto the NDs, which was found to be a single photon emitter (see Appendix A.4 for further details of device fabriation). An atomic force microscope (AFM) image of the fabricated waveguide is illustrated in Figure 3-4(a). Postfabrication charge coupled device (CCD) camera image shows the coupling of the emitter to the DLSPP waveguide and subsequent emission from the gratings at the two ends (Figure 3-4(b)), when the NV center is excited. Figure 3-4(c) shows the emission spectra of the NV-center taken before and after coupling, as well as the spectrum of the out-coupled light from the grating end A. In Figure 3-4(d), lifetime of the NV-center before and after coupling is presented. A lifetime

reduction (from ~10 ns to ~6 ns) is observed for the coupled NV-center. The lifetimes are obtained by tail fitting of the measured data with a single exponential. First few ns of the data is avoided in the fitting, as it arises from background fluorescence. In different experiments, the lifetime changes in the range of 1.5 to 3.1 are observed, and on average, the lifetime decreased by a factor of ~2.5.

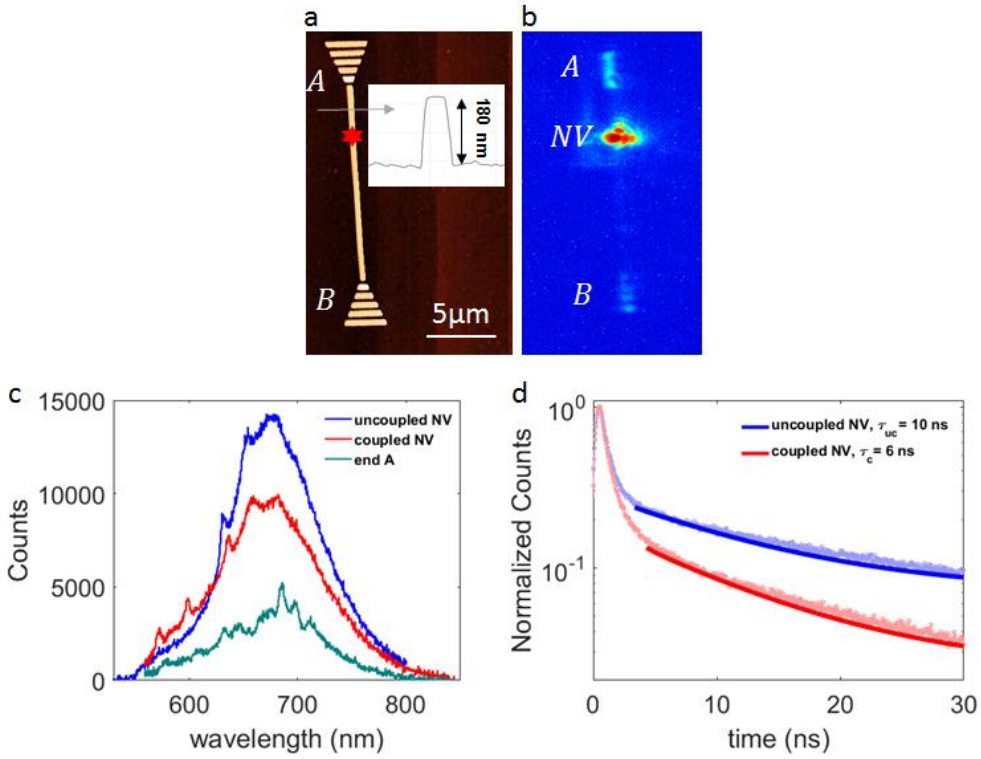

Figure 3-4 Coupling of a single NV center to DLSPPW mode. (a) AFM image of the fabricated waveguide. The inset shows thickness profile across the grey arrow and indicates a 180 nm height for the waveguide. (b) CCD camera image of the whole structure where the ND is excited and a fluorescence image of the focal plane is taken. Emission from the gratings at the ends of the waveguide, when ND is excited, confirms the coupling of NV center to the waveguide mode. (c) Spectrum taken from uncoupled NV (blue), coupled NV (red), and outcoupled light through the grating end A (green). (d) Lifetime of the NV center before (blue) and after (red) coupling.

Antibunching dip observed in the second-order correlation function of the NV-center both before (Figure 3-5(a)) and after (Figure 3-5(b)) fabrication of the waveguide, indicating a single photon emitter ($g^2(0) < 0.5$). The measured data was fitted with an exponential model presented in ref 91. The cross-correlation (featuring $g^2(0) < 0.5$)

between the out-coupled emission at the end B and the emission collected from the NV-center shows that the source of emission at ND spot and end B is the same, and that it is a single photon emitter (Figure 3-5(c)). This also means that the emission from NV center creates single plasmons in the guided mode that propagate to the ends of the waveguide and are scattered to the far field as single photons.

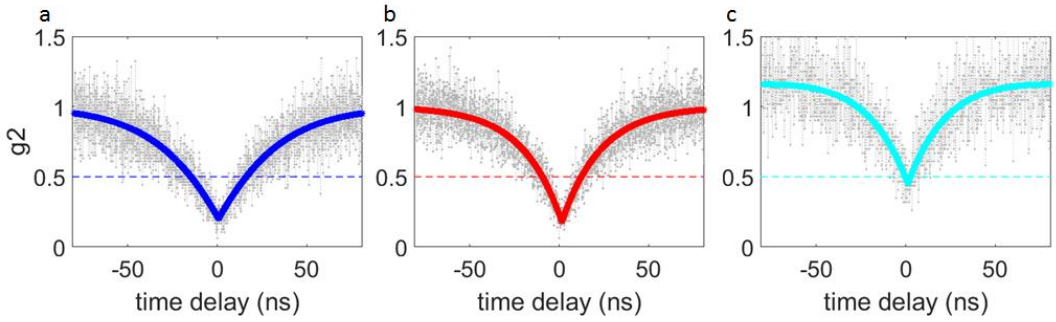

Figure 3-5 Antibunching measurements for the NV-DLSPPW coupled system. Autocorrelation for the NV center before (a) and after (b) coupling to the waveguide, and cross-correction between the outcoupled emission from the end B and the emission collected directly from the NV center (c).

In Figure 3-6, the histogram of lifetimes measured for NVs both on glass and on Ag film are compared. The result indicates an average lifetime reduction of ~2 for the Ag film (from ~18.1 ns on glass to ~9.4 ns on Ag film). This gives a ~5-fold enhancement in the total decay rate (Γ_{tot}).

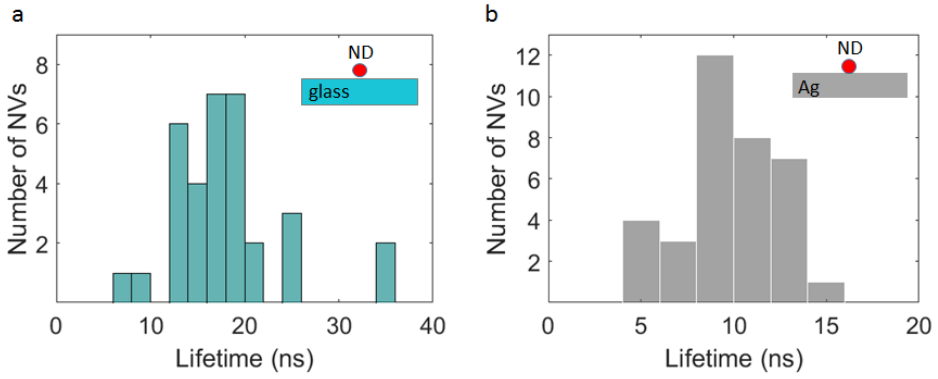

Figure 3-6 Histogram data statistics of lifetimes for the NV centers. Distribution of fluorescence lifetimes for single-photon NV emitters on glass (a) and on Ag film (b) indicating an average Purcell factor of 2 for the Ag film.

The propagation characteristics of the DLSPP waveguide for several waveguide samples of different lengths were measured by comparing the attenuation of fluorescence signals P_A and P_B at the two ends of waveguides and their corresponding propagation distances L_A and L_B from coupled NV centers. The 1/e propagation length, L_P, is extracted from the fluorescence signals at the two ends using $P_A/P_B = \exp[(L_A - L_B)/ L_P]$, assuming symmetric coupling in two directions, uniform losses across the waveguide and the same out-coupling efficiency at the grating ends. The collected data are fitted to obtain the propagation length of 20 ± 5 μm for the NV-DLSPPW system.

In simulations, the emitter's decay rate into the plasmonic mode (Γ_{pl}) guided by the DLSPP waveguide was calculated using 2D finite-element method (FEM) [120]. Normalized by the spontaneous emission decay rate in the vacuum (Γ_0), a 3-fold emission enhancement due to the plasmonic excitation is obtained (Figure 3-7(a)). Emission coupling efficiency (β factor) to the DLSPP waveguide was defined as the probability that the QE excites a single plasmonic mode. It can be described by the fraction of the emitted energy that is coupled to the plasmonic mode, that is, $\beta = \Gamma_{pl}/\Gamma_{tot}$, where Γ_{pl} is the plasmonic decay rate obtained from the 2D simulation result shown in Figure 3-7(a), and Γ_{tot} is the total decay rate, including radiative decay rate, nonradiative decay rate, and the plasmonic decay rate of the QE coupled to the DLSPP waveguide. A 3D FEM model with scattering boundaries surrounding the computational domain is implemented using COMSOL Multiphysics software and the total decay rate is extracted from the total power dissipation of the coupled emitter, as explained in refs 120 and 121. The coupling for a vertically oriented QE with a DLSPP waveguide is studied for two cases: (1) the distance of the emitter to the Ag surface is fixed to 35 nm, and the emitter is moved along *x* (Figure 3-7(b)); and (2) the emitter is moved upward from the surface of the metal along *y*-axis (Figure 3-7(c)). The distance dependence of the plasmonic decay rate (Γ_{pl}/Γ_0), and β factor for an emitter coupled to a DLSPP waveguide with 250 nm width, 180 nm height, and dielectric refractive index of n_d = 1.41, are calculated for both cases in Figure 3-7(b,c), respectively. The Palik's data[122] was used to simulate the refractive index of Ag layer. With optimized distance of the emitter to the Ag surface, the β factor can reach 63%.

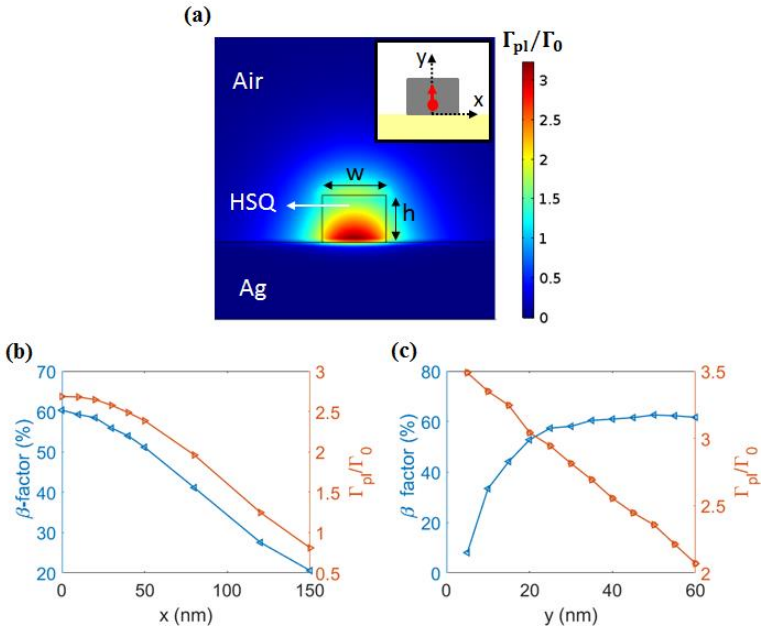

Figure 3-7 Simulated characteristics of the NV-DLSPPW coupled system. (a) Simulation result for plasmonic decay rate Γ_{pl}/Γ_0 shows a 3-fold emission enhancement at the optimal position of the emitter. The inset illustrates the NV center inside the DLSPP waveguide in the cross-section. Distance dependence of the plasmonic decay rate and spontaneous emission β factor for DLSPP waveguide coupled NV emitter with a vertically oriented dipole (y-polarized). (b) Emitter moved along x direction outward from the middle of the waveguide (y = 35 nm). (c) Emitter moved along the y-axis outward from the Ag surface.

In the experiment, one can calculate the apparent plasmonic coupling factor, β_{pl}, using $\beta_{pl} \simeq [I_A + I_B]/ [I_A + I_B + I_{NV}]$, where I_A and I_B are the emission intensity collected by galvanometric mirror scan at the ends of the waveguide and I_{NV} is the emission intensity measured at the NV center position (i.e., free space emission not coupled to the DLSPP mode). Here, one can assume same collection efficiency from the NV center as well as that from the ends, and ignore the nonradiative decay, as the changes in observed lifetimes are not very high. An apparent coupling factor of 48% is found for the NV- DLSPPW system shown in Figure 3-4. Taking the propagation length of the DLSPP waveguide into account, the corrected plasmonic coupling factor of 58% is obtained. This is in good agreement with the simulation result and predicts a satisfactory precision in deterministic positioning of the DLSPP waveguide onto the ND.

3.4 Coupling of a SiV center into DLSPPW mode

The Si-doped NDs are synthesized under a HPHT condition in a fluorohydrocarbon metal catalyst-free system following the recipe in ref 123. In Figure 3-8, the experimental measurements obtained for a HPHT SiV-ND embedded in a DLSPPW system is illustrated.

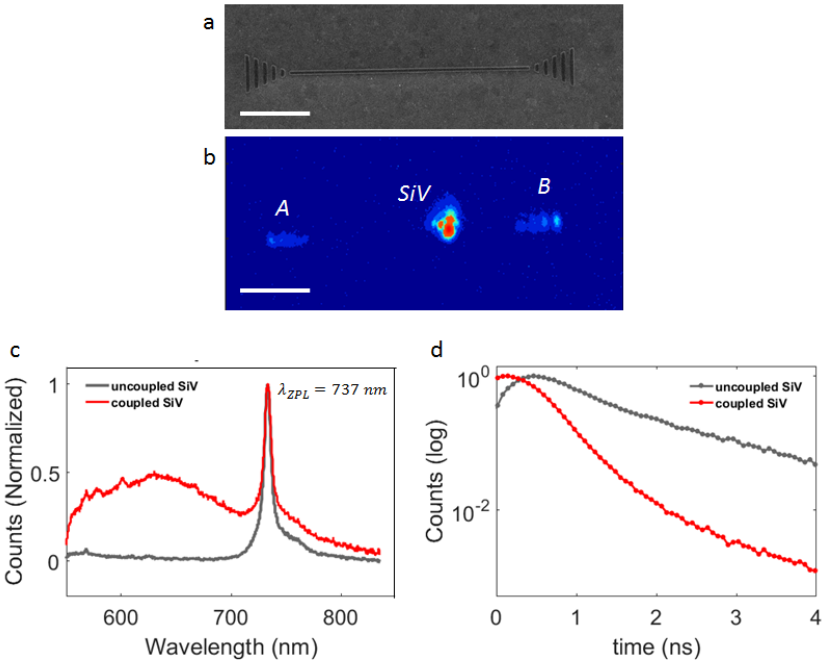

Figure 3-8 SiV-ND coupled to DLSPPW mode. (a) SEM image. (b) Galvanometric mirror scan image when the SiV-ND is excited with green pump laser and fluorescent light is collected. (c, d) Fluorescence spectra (c) and lifetimes (d) taken before (grey), and after coupling (red). The scale bars are 5 μm.

3.5 Coupling of a single GeV center into DLSPPW mode

In this section, the experimental results for the GeV-DLSPPW system is demonstrated. An atomic force microscopy (AFM) image of the HSQ waveguide is presented in Figure 3-9(a, left). The whole structure, when the GeV center was directly excited with green pump laser, was imaged using a CCD camera. The image shows three spots, GeV, A and B (Figure 3-9(a, right)). This shows excitation and emission of the GeV emitter (GeV), coupling of GeV emission to the DLSPPW mode, propagation and out-coupled radiation from the two ends (A and B). Figure 3-9(b) shows the normalized emission spectra of the

uncoupled (grey) and coupled (red) for the excitation power of 25 μW and an integration time of 300 s. Figure 3-9(c) shows the spectra from the out-coupling grating couplers A and B, indicating the on-chip transmission of the spectrally narrow surface plasmon mode excited by the GeV emitter. The antibunching dip of the correlation function, before (Figure 3-9(d)) and after (Figure 3-9(e)) coupling, indicating a single GeV emitter (g^2 (τ = 0) < 0.5). The data are analyzed with a single exponential fitting curve[96]. The lifetime of the GeV center before (Figure 3-9(e), grey) and after (Figure 3-9(e), red) coupling is measured, indicating a lifetime shortening from ~12.3 to ~3.8 ns for the coupled GeV center. The lifetimes are obtained by tail fitting of the measured data with a single exponential curve[96]. The lifetime decreased by a factor of ~3 ± 0.5, which is in addition to the two times reduction due to the Ag plane, giving, on average, a ~six fold Purcell enhancement.

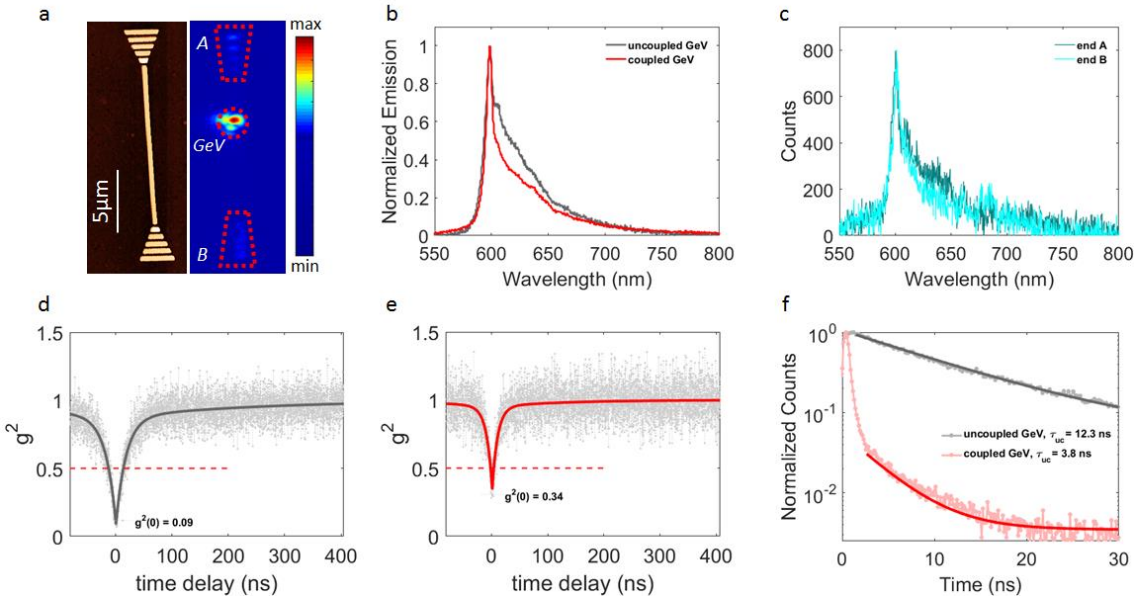

Figure 3-9 Excitation of a single GeV-ND embedded in a DLSPP waveguide. (a) AFM image of the fabricated waveguide (left), and CCD camera image of the whole structure where the ND is excited and a fluorescence image of the focal plane is taken (right). (b) Spectrum taken from uncoupled GeV (grey line) and coupled GeV (red line). (c) Spectrum from outcoupled light through the grating ends A and B (g). The integration time of the spectra is 300 s, and the excitation power is 25 μW. (d, e) Second order correlation of the GeV center before (d) and after (e) coupling to the waveguide. (f) Lifetime of the GeV center taken before (grey) and after (red) coupling.

The propagation length is estimated to be 9 ± 3 μm for the GeV–DLSPPW hybrid system on the Ag film, which is smaller than the NV–DLSPPW system due to the higher SPP loss at the lower wavelength region corresponding to emission from GeV centers (ZPL, λ = 602 nm). Using a single-crystalline Ag flake instead of the Ag film can significantly enhance the propagation length of SPPs[124]. The fabricated nanoridge atop Ag crystal even allows the propagation of SPPs at the green region (λ = 532 nm) as shown in Figure 3-10.The new platform paves the way for realization of remote excitation of integrated QEs for on-chip application (discussed in detail in section 3.6).

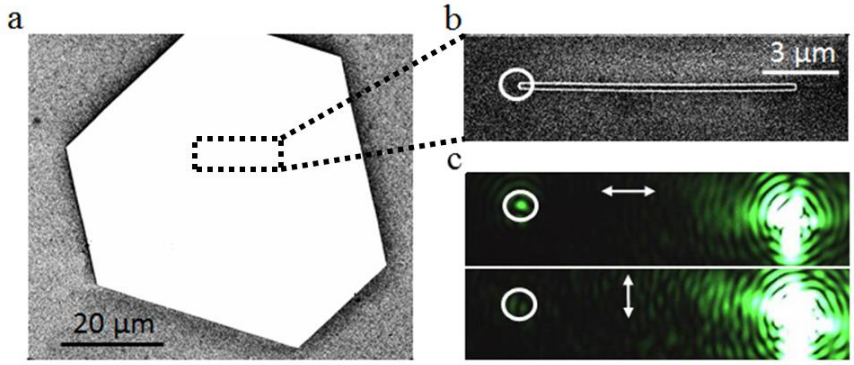

Figure 3-10 Transmission of the 532-nm pump laser light along the low-loss plasmonic platform. (a) SEM image of a Ag crystal flake. (b) SEM image of a fabricated nanoridge waveguide on Ag crystalline Ag flake (c) Optical characterization of the DLSPPW.

3.6 On-chip remote excitation of a single GeV center

Figure 3-11 shows a schematic of the device layout, introducing the working principle of on-chip remote excitation. The hybrid plasmonic configuration enabled the green laser light to propagate on-chip, in the DLSPPW, and reach to an embedded ND containing a single GeV center. The remote GeV emitter is thereby excited, and single photons are channeled to a DLSPPW mode.

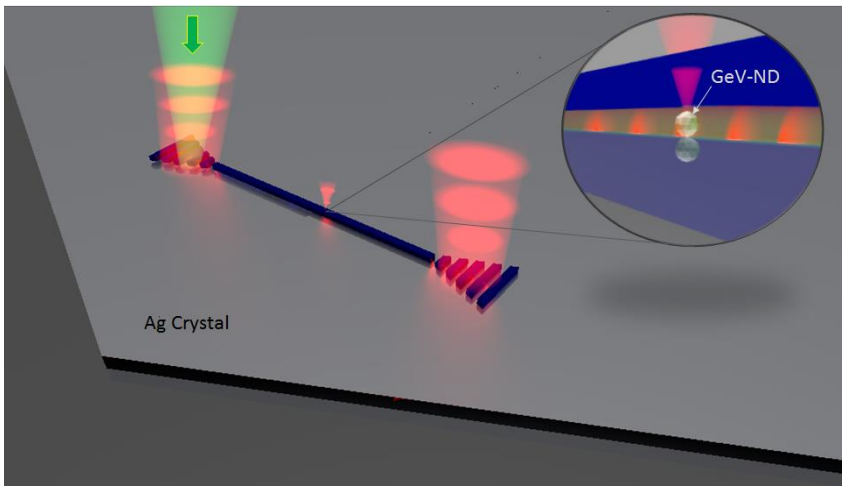

Figure 3-11 Schematic of the device layout and working principle for on-chip excitation of a ND carrying spectrally narrow single GeV QEs embedded in a DLSPP waveguide. A 532-nm pump laser light is coupled with a grating, propagates on-chip in the low loss DLSPPW and reaches an embedded ND that contains a single GeV center (GeV-ND). The remote GeV emitter is thereby excited, generating single optical plasmons propagating along the waveguide and outcoupling from the ends.

In the experiment, the capability of green light transmission in the DLSPPW on Ag crystals was employed to demonstrate remote excitation of GeV-ND embedded in low-loss DLSPPWs. A small amount of the synthesized solution of Ag crystal flakes was spin coated on a Ag-coated silicon wafer. A PAH layer was put on the Ag film to improve the adhesion of the Ag flakes to the substrate[112]. The markers were fabricated on Ag flakes, and the NDs with GeV centers were spin-coated. The sample fluorescence was then imaged using confocal microscopy. Spectra and correlation functions were taken for the NDs on Ag crystals. Using EBL, the HSQ waveguides were fabricated on the Ag crystal, embedding the selected single GeV-NDs. A schematic of the device layout and working principle for on-chip remote excitation is illustrated in Figure 3-12(a). Figure 3-12(b) shows an AFM image of the fabricated waveguide (left) and a galvanometric mirror scan image (right) when the waveguide is excited from end B with the green pump laser and the fluorescence emission detected at the focal plane. Emission from the embedded GeV-ND located inside the waveguide confirms a remote excitation of the GeV center, and out-coupled radiation from the two ends (A and B) indicates the coupling of the GeV center to the DLSPPW mode. Figure 3-12(c) illustrates the spectrum of the GeV emitter

before coupling (ND on the Ag crystal). The emission spectra after coupling for the remotely excited GeV center (solid line) and the spectrum for the same GeV center when excited directly (dotted line) is presented in Figure 3-12(d). CCD images for the coupled system when excited directly and with a linear polarizer placed in the detection path are presented in Figure 3-12(e). A comparison of the two images in Figure 3-12(e) clearly indicates a strongly polarized emission from the end of the waveguide due to the coupling of the emission to the fundamental TM mode of the DLSPP waveguide, propagation and subsequent scattering from the ends. Figure 3-12(f) shows the spectrum measured at the grating end A, when the GeV center is remotely excited (Figure 3-12(b)). In Figure 3-12(g), the second-order correlation function for the GeV center is presented, confirming single photon emission ($g^2(\tau = 0) < 0.5$).

The GeV decay rate into the DLSPPW mode was simulated using the FEM method. The GeV center was modelled as a single dipole emitting at 602 nm in the simulations. An up to four-fold decay rate to the plasmonic mode is predicted for a GeV center in the waveguide compared to its emission in vacuum. Figure 3-13(a) shows the plasmonic decay rate dependence for the optimum orientation of the dipole on its position in the waveguide. The emission efficiency (β factor) of the emitter to the DLSPPW mode is given by $\beta = \Gamma_{pl}/\Gamma_{tot}$, where Γ_{tot} denotes the total decay rate, and Γ_{pl} is plasmonic decay rate. The total decay rate is calculated from the time evolution of the total dissipated power[120]. The β factor for a y-oriented GeV coupled to a DLSPPW is simulated as a function of the position in the cross section (Figure 3-13(b)). Palik's data[122] were used for modelling of the Ag refractive index. The simulated results show that the β factor can reach 62%.

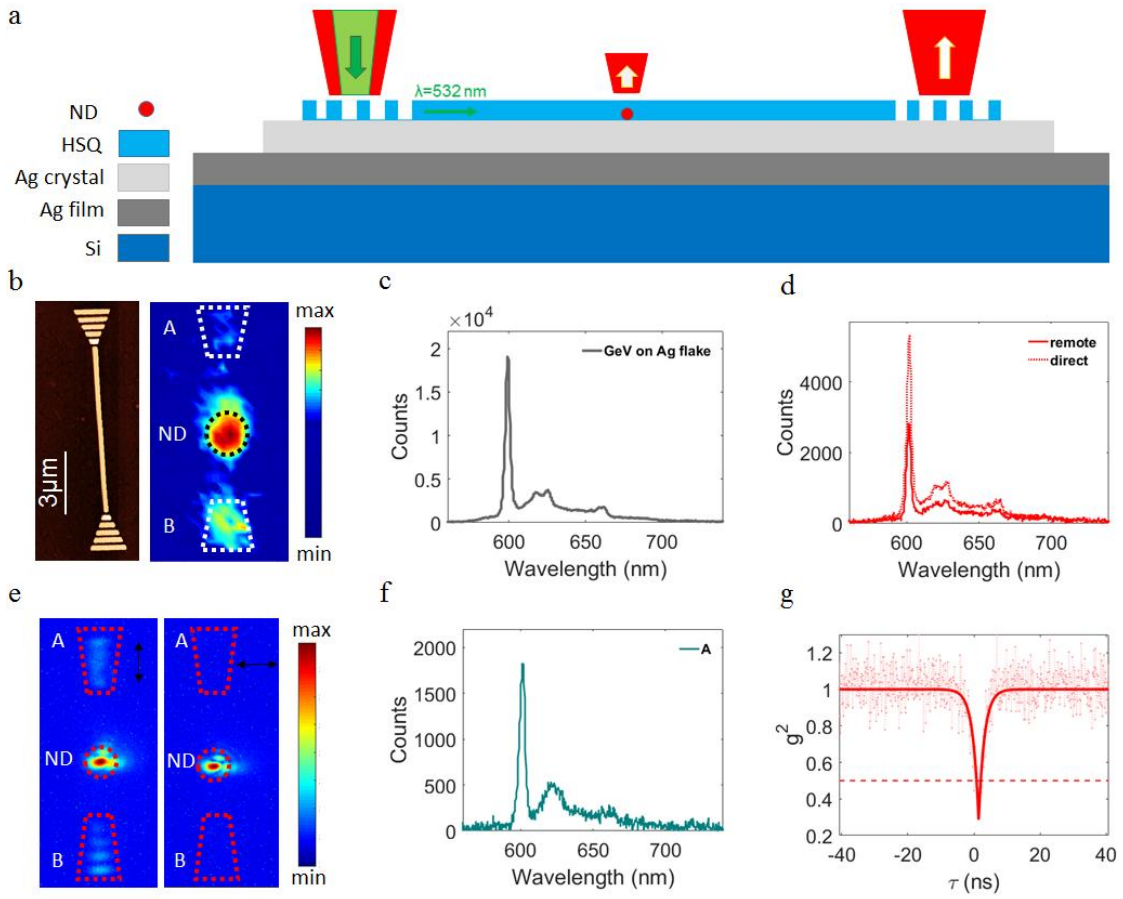

Figure 3-12 On-chip remote excitation of a single GeV-ND. (a) Schematic of a sample layout for on-chip remote excitation of a GeV-ND embedded in the plasmonic structure. (b) AFM image of the fabricated waveguide (b, left) and galvanometric mirror scan image showing the remote excitation of the embedded GeV where the pump laser light is illuminated at end B (b, right). Higher emission at end B is caused by the background fluorescence from the grating coupler exposed to the strong pump light. (c, d) Spectra taken from the uncoupled GeV, i.e. the ND on the Ag plate (c) and from coupled GeV when excited remotely (d, solid line) and in the case of direct excitation (d, dotted line). (e) CCD images for the coupled system when excited directly and with a linear polarizer placed in the detection path are presented for two orthogonal polarizations, parallel (left) and perpendicular (right) to the waveguide axis. (f) Spectrum taken from the outcoupled light through grating end A in the case of remote excitation. The integration time on the spectra data is 300 s, and the excitation powers are 2 μW (c, d) and 5 μW (f). (g) Second order correlation function of the GeV emitter confirming a single photon emission.

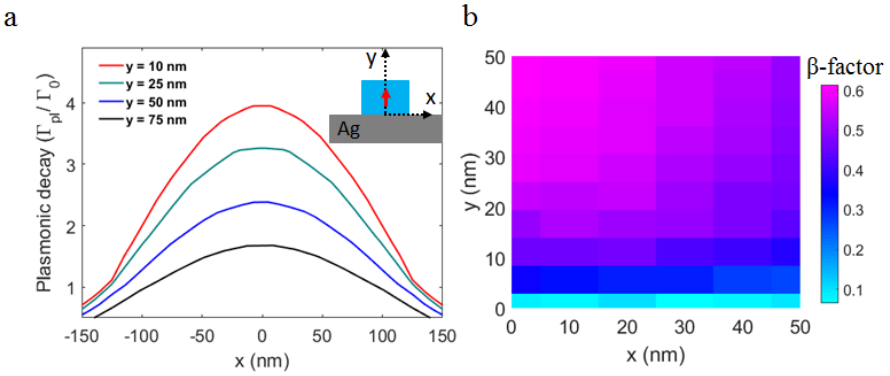

Figure 3-13 Simulated characteristics of the GeV-DLSPPW system. (a) Simulated plasmonic decay rate (Γ_{pl}/Γ_0) for the GeV-DLSPPW system. Inset shows the cross section of a *y*-oriented dipole emitter inside the DLSPP waveguide (top right). (b) Distribution profile of the β factor, i.e. Γ_{pl}/Γ_{tot}, for a distribution of the GeV center inside a ND, where each colored square represents the central value of the corresponding in-plane dipole position.

The apparent β factor (β_{pl}) was measured using $\beta_{pl} \simeq (I_A + I_B)/(I_A + I_B + I_{GeV})$, in which I_A and I_B are the out-coupled radiation at the ends A and B, respectively, and I_{GeV} is the measured intensity at the GeV center position. This gives a β factor of 56% for the GeV–DLSPPW system shown in Figure 3-12, which is in good agreement with the simulated β factor, indicating accurate alignment of the waveguide with respect to the GeV-ND. The 1/e propagation length of the GeV emission is measured along the DLSPPW on Ag crystal, the same way as described for Ag film, and a value of 33 ± 3 μm is obtained. This is significantly larger than DLSPPW on the polycrystalline Ag film and even higher than the propagation length of NV-DLSPPW system, indicating low material loss for the single crystalline Ag flakes.

The ability of a hybrid plasmonic system to realize efficient single-photon transmission can be quantified by a figure of merit (FOM) defined as the product of the propagation length, Purcell factor (Γ_{tot}/Γ_0) and and β factor, normalized by the operation wavelength (λ), as proposed in ref 43. The GeV-DLSPPW system reaches a value of 180 ± 25 ($\Gamma_{tot}/\Gamma_0 = 6 \pm 1$, $\beta = 0.56 \pm 0.03$, $L_p = 33 \pm 3$ μm, $\lambda = 602$ nm), clearly outperforming previous demonstrations of quantum emitter-plasmonic waveguide (QE-PW) coupled systems[42,43,48,125,126]. A careful comparison of GeV–DLSPPW on the Ag crystal with other hybrid systems of QE-PW is presented in Figure 3-14. The efficiency of the light–

matter interaction in the GeV–DLSPPW platform can also be compared to other colour center photonic platforms using the so-called cooperativity parameter (defined as $\Gamma_w/(\Gamma_{tot}-\Gamma_w)$, in which Γ_w is the decay rate into a waveguide mode). For the SiV-center incorporated cavity system described in ref 87 and for the GeV–based platform presented in ref 96, the cooperativity of $C = 1$ and $C = 0.1$ have been deduced, respectively. The cooperativity was estimated to be $C = 1.5$ in the GeV–DLSPPW platform, which should be understood as the upper cooperativity limit evaluated from our experiment at room temperature (as opposed to the cooperativity estimated at low temperatures[87,96]). This can be enhanced further by using the waveguide integrated cavity resonator[127] and/or using dielectric ridges with a larger refractive index, e.g. titanium dioxide (TiO_2) with a refractive index of ~2.4, and smaller cross section DLSPPW mode (and therefore stronger coupling).

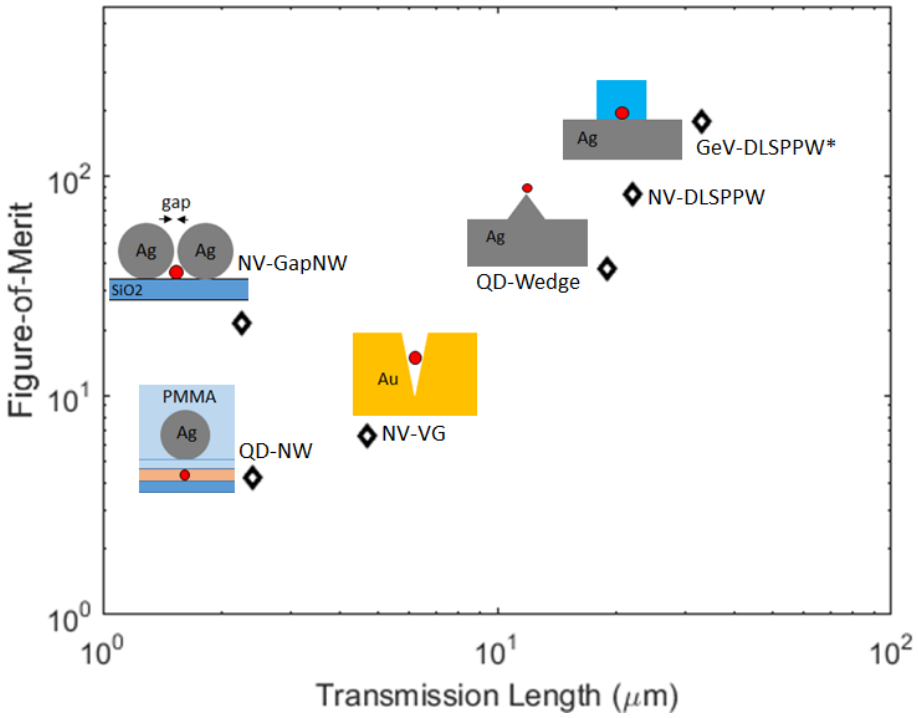

Figure 3-14 Efficiency of the GeV-DLSPPW platform compared with other hybrid quantum systems. Figure-of-merit (FOM) and transmission length of hybrid quantum plasmonic systems. The FOM of GeV–DLSPPW on the Ag crystal is compared with other demonstrated QE-PW hybrid systems, including QD-Ag nanowire (QD-NW)[42], NV-Gap Ag nanowire (NV-GapNW)[125], NV-V groove channel (NV-VG) waveguides [43], QD-Wedge waveguides (QD-wedge)[48] and NV–DLSPPW on a Ag film[126]. The black diamond markers in the graph are extracted from the experimental results reported for the corresponding hybrid systems.

3.7 Routing of single plasmons with directional couplers

When two DLSPP waveguides are placed in the vicinity to each other, their individual modes cease to exist and two modes called antisymmetric and symmetric modes are supported, as presented in Figure 3-15. The effective mode indices of the two modes are different and as the two modes propagate, the modes acquire a phase relative to the other mode. This results in a distribution of energy in the waveguides as a function of propagation distance, which can be used for routing of SPP modes, in case of DLSPP, from one DLSPPW to other. The coupling length L_c is given by $L_c = \lambda \cdot (n^+_{eff} - n^-_{eff})/2$, where n^+_{eff} and n^-_{eff} are the effective mode indices of symmetric and antisymmetric modes, respectively, and λ is the vacuum wavelength[128].

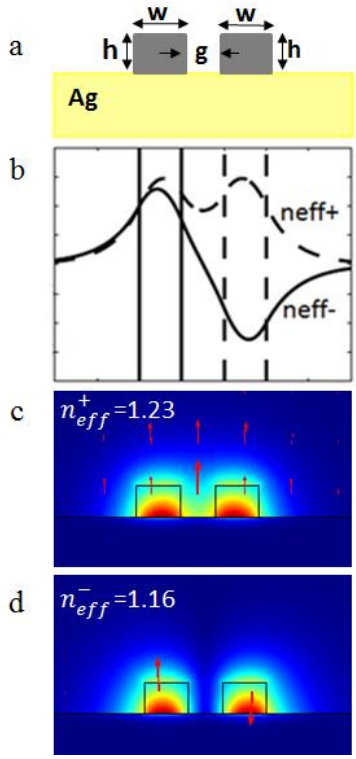

Figure 3-15 (a, b) DLSPP-based directional coupler (DC) structure consists of two rectangular DLSPP waveguides of height h = 180 nm, width w = 250 nm, refractive index n_d = 1.41, the separation gap at the parallel section is g = 200 nm (a). The length of the parallel section (coupling length) was designed to be L_c = 5.3 μm in order to impart a π phase shift, at λ = 700 nm, between the symmetric (n^{+}_{eff}) and anti-symmetric (n^{-}_{eff}) DLSPP modes supported by the structure (b). (c, d) Symmetric (c) and Antisymmetric modes (d). Surface shows electric field norm (V/m) profile and red arrows indicate E-field.

In Figure 3-16, a schematic of a DLSPPW-based DC system where emission from an embedded QE is coupled to a DLSPPW and routed to another DLSPPW is illustrated. In the experiment, the DLSPPW-based DC is fabricated onto a ND containing a single NV emitter. SEM image of the fabricated DC is presented in Figure 3-17(a, top). Postfabrication fluorescent emission imaged on a CCD camera, while the NV-center is excited, shows the coupling of the emitter to the structure, and subsequent emission from the grating at the three ends (Figure 3-17(a, bottom)). For emission at spot C, the emission from NV center creates single plasmons that first propagate in first waveguide, are routed to the second waveguide, propagate to end C, where it is scattered to the far field as single photons. Emission spectra of the NV center (before and after coupling) and the

outcoupled end C are shown in Figure 3-17(b). Lifetime measurements of the NV center, taken before and after coupling, show a reduction from 12 to 5 ns due to the emission enhancement of the coupled NV center (Figure 3-17(c)). Th antibunching dips in the second-order autocorrelation function of the coupled NV center are observed in the measurement results as shown in Figure 3-17(d), indicating single photon emission.

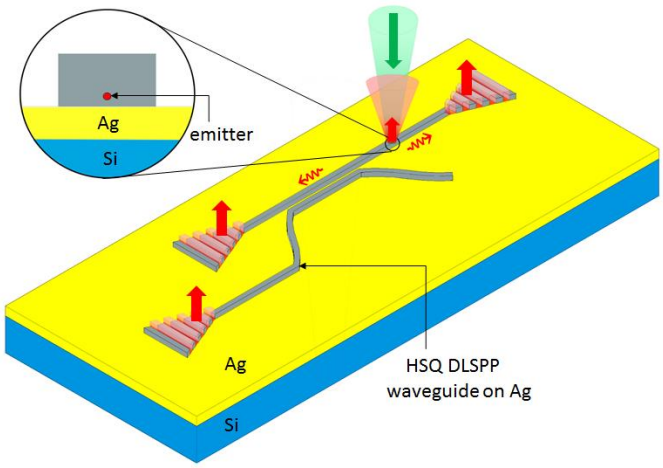

Figure 3-16 Schematic of a DLSPPW-based DC system where emission from an embedded QE is coupled to a DLSPPW and routed to another DLSPPW.

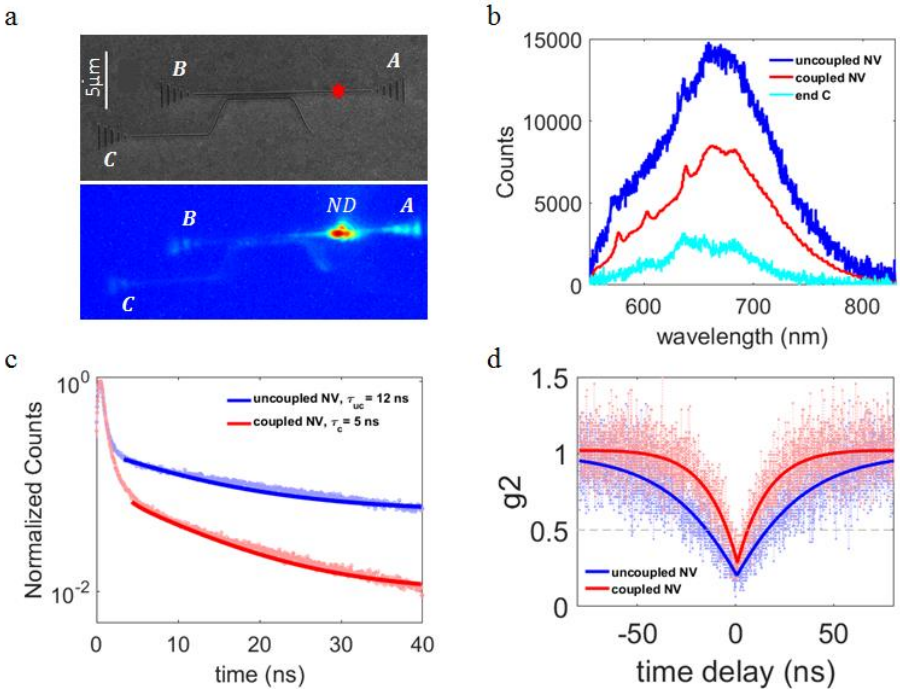

Figure 3-17 Routing of single plasmons in a DLSPPW-based DC (a) SEM image of the fabricated DLSPP-based DC (top). CCD camera image of the whole structure when the ND is excited with a continuous wave (532 nm) laser (bottom). (b) Spectrum taken from the uncoupled NV (blue), the coupled NV (red), and outcoupled end C (cyan). (c) Lifetime measured before (blue) and after (red) fabrication of the DC. (d) Autocorrelation from the uncoupled NV (blue), coupled NV (red).

Chapter 4: Cavity QED experiment with diamond nanocrystals

In this chapter, the top-down nanofabrication technique is employed to demonstrate compact photonic crystal cavities based of DLSPPWs that exhibit filtering abilities of reflecting Bragg gratings (RBG) to modify NV, SiV and GeV emissions. This technique enables to determine the in-plane position of QEs within ~30 nm, which provides the required length scale for accurate placement of an emitter inside a single-mode cavity resonator operating in the visible spectral range. The idea is to combine the SPP confinement with relatively low propagation loss by employing a hybrid plasmonic–photonic waveguide-cavity design and thereby to achieve a significant enhancement in the spontaneous emission rate of single photons at ZPLs. The schematic of the DLSPPW-based RBG cavity structure is shown in Figure 4-1. The DLSPPW-based RBG supports a fundamental SPP mode whose effective refractive index varies through the quarter wave stack layers of air/HSQ, creating a number of repeated pairs of low/high refractive indices needed to reflect the SPP mode.

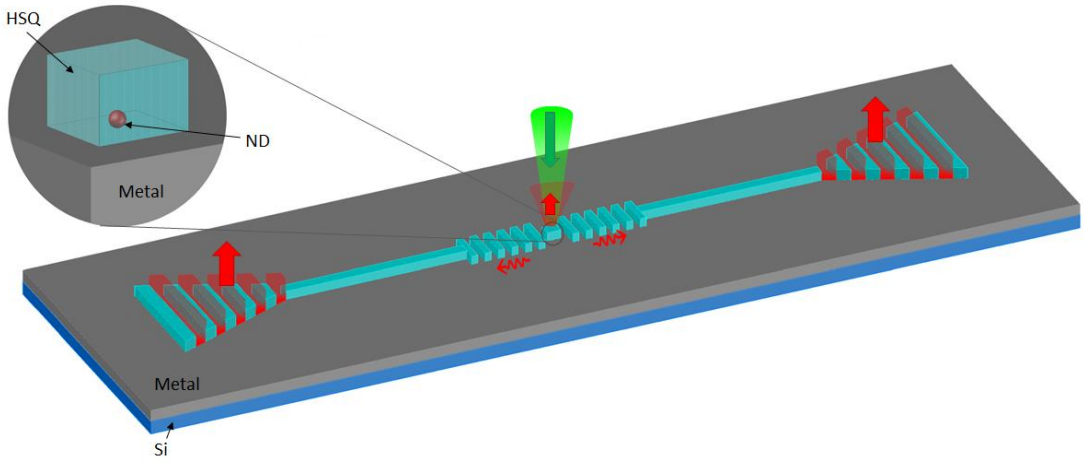

Figure 4-1 Schematic image of chip-integrated cavity-coupled single photon emitter in ND.

4.1 Characterization of DLSPPW-based photonic crystal bandgap

Figure 4-2(a) shows the RBG mirror structure atop metal layer. The HSQ waveguide ridges have a refractive index of 1.41, and dimensions of w_1 = 250 nm (width) and h = 180 nm (height) as shown in Figure 4-2(b). The dimensions of the nanoridges in the RBG are $\lambda_{DLSPP}/4$ in length, and 750 nm in width (w_2) as shown in Figure 4-2(c), and repeated with a period of $\Lambda = (\lambda_{SPP}/4) + (\lambda_{DLSPP}/4)$, where λ_{SPP} and λ_{DLSPP} are the effective wavelengths for SPP and DLSPP modes, respectively. In Figure 4-2(d, e), the simulated DLSPPW mode profiles corresponding to the HSQ nanoridges atop Ag layer with different widths of w_1 = 250 nm and w_2 = 750 nm are illustrated.

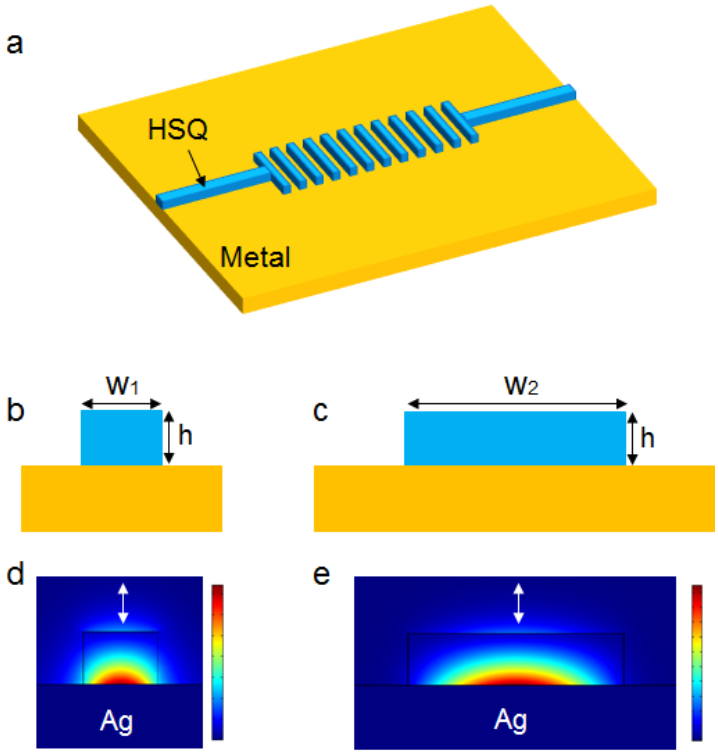

Figure 4-2 A one-dimensional photonic crystal structure on metal layer. (a) Schematic of the device layout. (b, c) Waveguide cross sections for different widths of w1 (b) and w2 (c). (d, e) Simulated DLSPPW mode profiles of the dielectric ridge waveguides on Ag layer with different widths of w_1 = 250 nm (d) and w_2 = 750 nm (e). The height of the ridges is h=180 nm and the refractive indices are n_d = 1.41 (HSQ) and n_{ag} = 0.14 + 4.52i (Ag layer, Palik's data at λ=700 nm).

Figure 4-3(a) shows a top view image of the RBG mirror structure. Finite-difference time-domain (FDTD) simulation results (Lumerical Solutions, Inc.) are shown in Figure 4-3(c), indicating stopband dips in the RBG transmission data (Figure 4-3(a)) corresponding to different Bragg periods (Λ) of 275 nm (cyan), 300 nm (light green), and 325 nm (dark green). The Palik's data[122] were used for modelling of the Ag refractive index. In the experiment, a silicon wafer was coated with a Ag film of 250 nm thickness (via thermal evaporation in a vacuum pressure of 2×10^{-7} Torr, and a rate of 4 nm s^{-1}). The HSQ e-beam resist (Dow Corning XR-1541-006) was then spin coated (1200 rpm, 1 min) to make a 180 nm film on the Ag layer and then the RBG mirrors structures were fabricated using EBL. SEM image of the fabricated device with the periodicity of 275 nm is shown in Figure 4-3 (b). Experimental characterization of the fabricated structures with different Bragg periods (Λ) of 275 nm (red), 300 nm (blue), and 325 nm (green) clearly

show the stopband transmissions for the RBG mirrors (Figure 4-3(d)) as predicted by the simulations. The transmission data in Figure 4-3(d) are normalized to the transmission through a straight waveguide (without Bragg gratings) as explained in Appendix A.5.

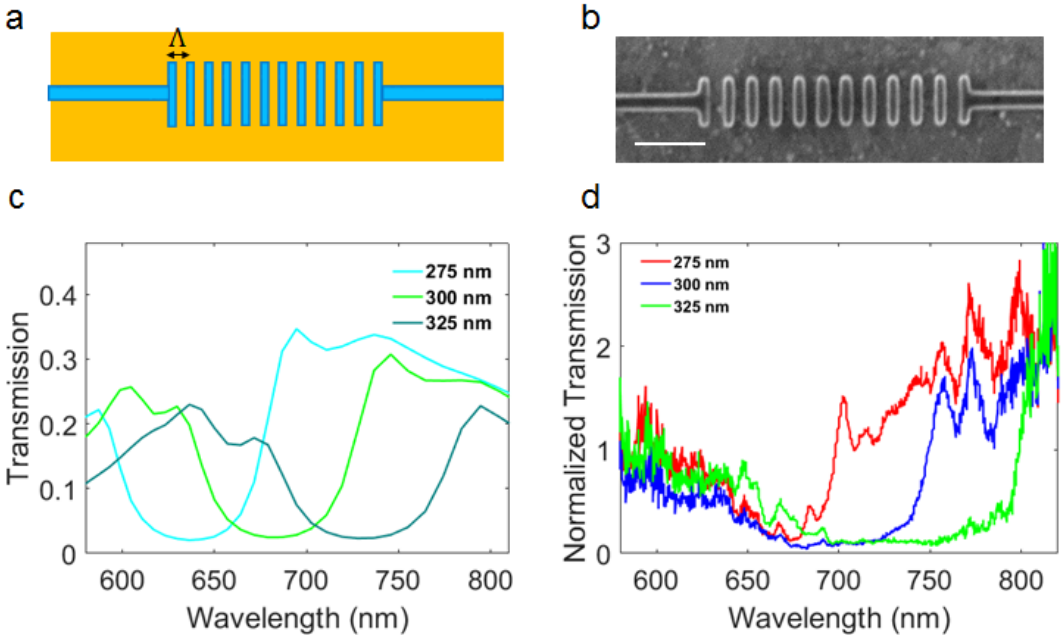

Figure 4-3 Characterization of one-dimensional photonic crystal structure on metal layer. (a) Top view of the device layout. (b) SEM image of the fabricated device with the periodicity of 275 nm. The scale bar is 1 μm. (c, d) Simulated and measured transmission spectra of the Bragg reflector for different periodicity of 275 nm, 300 nm, and 325 nm. The height of the HSQ nanoridges is h=180 nm, and the widths are w_1=250 nm (waveguide) and w_2=750 nm (Bragg grating). The metal layer is simulated based on Palik's data[122].

4.2 DLSPP-based unidirectional coupler for single GeV center

In this section, the lithographic alignment technique was employed to realize an integrated waveguide-mirror configuration with RBG, where the pre-selected GeV-ND is embedded in the waveguide and placed at the specific constructive interference point (at the distance of the second constructive point of the RBG mirror, i.e., $d = 3\lambda_n/4$, where λ_n is the wavelength of the plasmonic mode[129]) as shown in Figure 4-4.

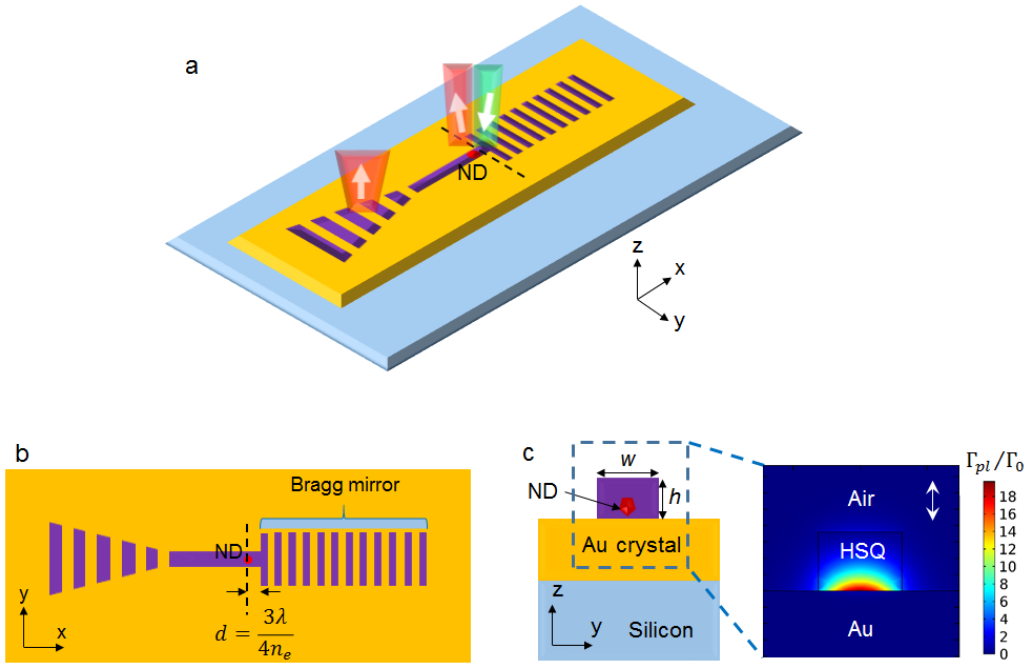

Figure 4-4 DLSPP-based unidirectional coupler for GeV center. (a) Schematic of the device layout and working principle. (b) Top view of the device layout. The dashed line in (b) shows *x* position of the embedded ND at the distance of the second constructive point of the RBG mirror, i.e., d = $3\lambda_n/4$, where λ_n is the wavelength of the DLSPP mode. (c) DLSPP mode profile at the constructive point, indicating the distribution of Purcell enhancement (Γ_{pl}/Γ_0, plasmonic decay rate) for the coupled system, while *w* = 250 nm and *h* = 180 nm.

In the experiment, colloidal Au crystals were grown on a silicon substrate using a thermolysis synthesis technique[113] (see details in Appendix A.3). Lithographic alignment markers were made on top of (and nearby) the Au crystals, and NDs were deposited on the substrate afterwards. The sample was then loaded on the cold-finger of a continuous flow helium cryostat, which was cooled to 4.7 K for confocal microscopy measurements (see cryogenic optical setup in Appendix A.2, Figure A-4). Fluorescence image was taken from a crystalline Au flake on which NDs containing single GeV centers were deposited. A single GeV emitter was selected based on fluorescence spectrum measurements, and its location was determined with respect to the markers. Utilizing the lithographic alignment technique, an intgrated waveguide-RBG configuration with GeV is demonstrated, where the pre-selected ND is embedded in the waveguide and placed at the specific constructive interference point. SEM image of the fabricated device is

illustrated in Figure 4-5(a). Excited with the green laser (λ = 532 nm), the fluorescence light was collected from the excitation point (GeV-ND) and away of it within several micometers using a galvanometric scanning mirror. The result is illustrated in Figure 4-5(b), showing two spots, one from the excited GeV emitter, and the other from the grating output at the end (outcoupler). This indicates coupling of GeV emission to the waveguide mode of the unidirectional SPP device. Fluorescence spectrum taken at the output grating was compared with the spectrum from the center (i.e., from part of the emission that is not coupled to the plasmon mode), indicating a narrower linewidth at the end (see Figure 4-5(c)). This can be explained with polarization properties of the propagating plasmon mode, for which out-of-plane component is dominant (see Appendix A.7, Figure A-9). Therefore, only compatible part of the emission (that is polarized either out-of-plane or along waveguide axis) is allowed to propagate along the plasmonic waveguide while the remaining power contributed to the far-field radiation collected at the center. Polarization selectivity of the unidirectional coupler was simulated by modeling the GeV emitter by an electric dipole oriented along different directions to excite the propagating mode in the waveguide (see Appendix A.7, Figure A-9). The direction of propagating single photons emitted from the GeV center (and in general all group IV color centers) can be controlled by using this way, an alternative approach to other propagation-direction-dependent techniques based on chiral interactions[130,131] or topological protection[132]. Lifetime measurements before and after structure fabrication (Figure 4-5(d, e)) indicate a 10-fold enhancement in the total decay rate of the GeV emitter, a remarkable record due to the interaction with the unidirectional SPP coupler. In order to verify the properties of the unidirectional SPP coupler, scanning near-field optical microscope (SNOM) measurements perfomed for the unidirectional device, indicating ~80% reflectance from the RBG mirror (see Appendix A.6).

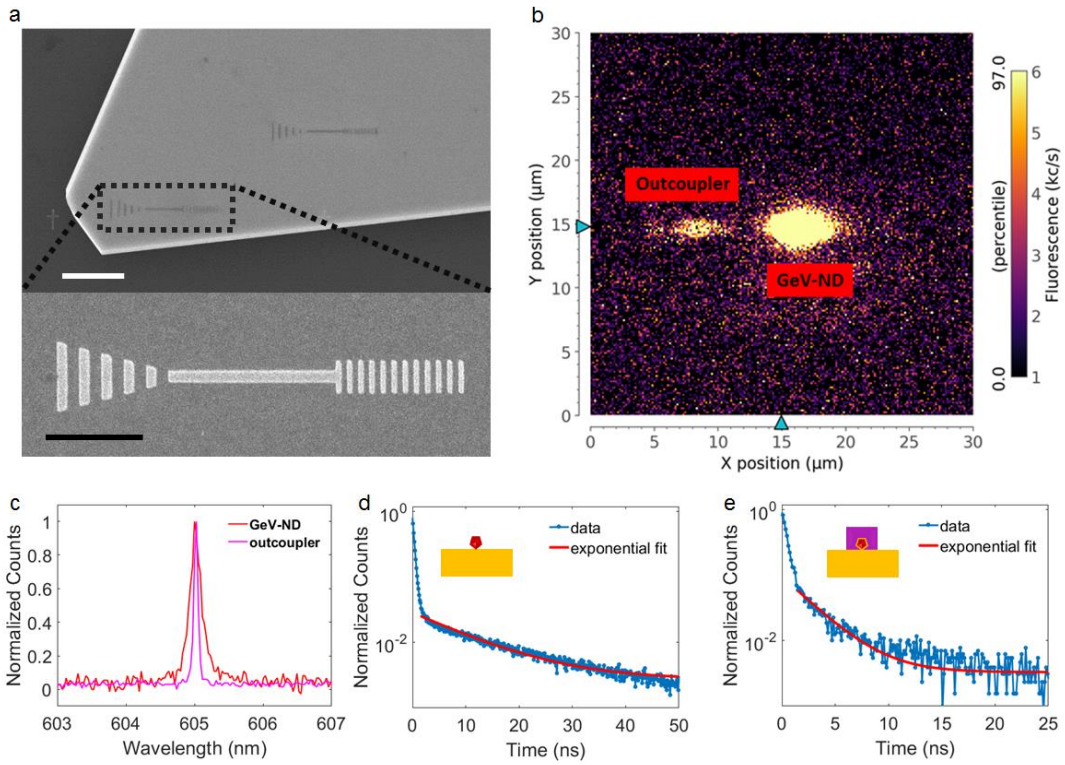

Figure 4-5 Unidirectional excitation of a single GeV color center in a ND. (a) SEM image of the fabricated device on Au crystal. The periodicity of the RBG is 240 nm. The scale bars for top and bottom images are 5 μm and 2 μm, respectively. (b) Galvanometric mirror scan image of the coupled system. (c) Spectra taken from the embedded GeV-ND (red) and from the outcoupled light at the end (purple). (d, e) Lifetime measurement data from uncoupled GeV (d, ND on Au crystal), and coupled GeV (c, ND embedded in the device). The data were analyzed with a single exponential function (I_{tot}=A·exp(−t/τ_A)+C, where τ_A indicates the lifetime, and A and C are constants[96,133]), indicating a 5-fold lifetime shortening from 11.2 ns (ND on Au flake) to 2.3 ns (ND embedded in device). Considering an additional 2-fold reduction due to the metal layer, one can estimate a 10-fold decay rate enhancement in total.

4.3 DLSPP-based unidirectional coupler for single NV center

The TM bandgap of the RBG mirror can be designed for other spectral regions (e.g., suited for NV, SiV, SnV and PbV centers). Simulated photonic bandgap of the RBG structure designed for NV center is illustrated in Figure 4-6 and compared with the transmission data measured by using a supercontinuum laser.

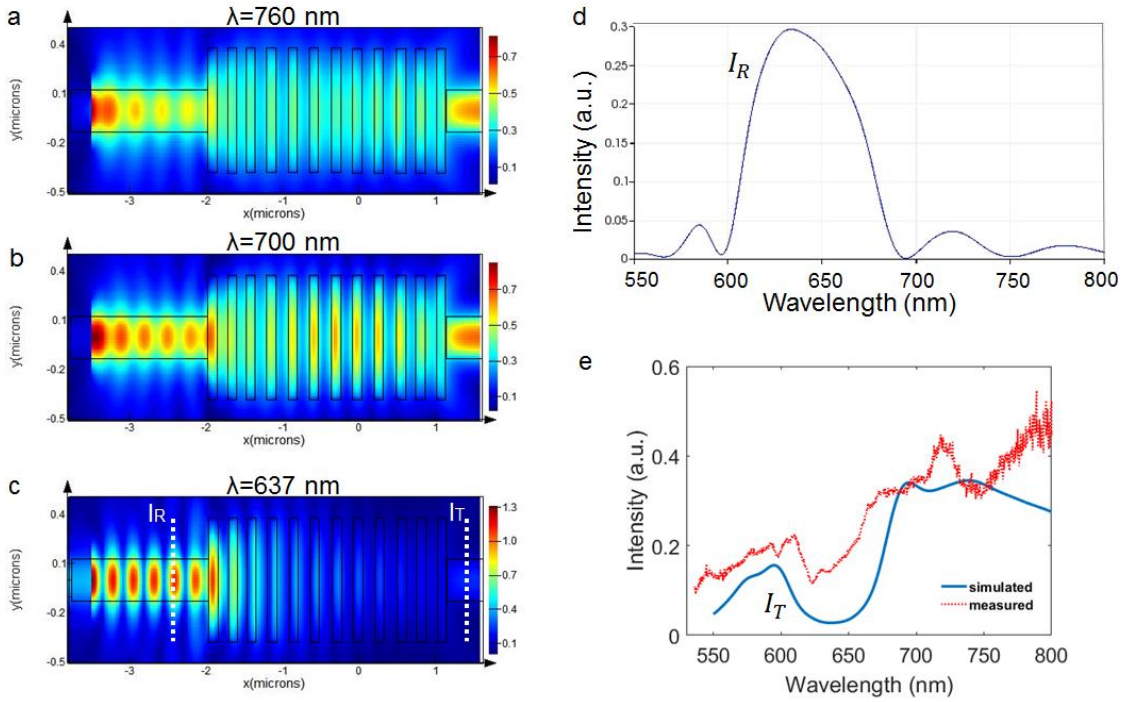

Figure 4-6 Optical characterization of the RBG structure designed for NV center. (a-c) Simulated E-field intensity profile for the structure, outside the TM bandgap, at λ = 760 nm (a) and λ = 700 nm, and inside the bandgap at λ = 637 nm (NV, ZPL). (c) Simulated result for the total intensity at the second hot spot (I_R). (d) Transmission data measured by using a supercontinuum laser (dotted red line) and the corresponding simulated result (I_T, blue line).

Figure 4-7 shows an experiment with a single NV center in ND (Microdiamant MSY 0−0.05 μm GAF) coupled to the unidirectional waveguide-RBG system. SEM image of the fabricated device and a fluorescence image of the focal plane was taken by a galvanometric mirror scan are illustrated in Figure 4-7(a), indicating a unidirectional interaction with propagating SPP mode. A remarkable record of 12-fold decay rate enhancement is achieved due to the 6-fold lifetime shortening of the coupled NV (from 26.3 ns to 4.3 ns as shown in Figure 4-7(b)), and an additional 2-fold reduction for the metal layer contribution. Lifetime date for the NV center were fitted with a double exponential function ($I_{tot} = A.\exp(-t/\tau_A) + B.\exp(-t/\tau_B)+C$, in which A, B and C are constants) and the lifetime values were calculated from $\tau = [A.\tau_A+B.\tau_B]/[A+B]$. Therefore, the unidirectional system delivered 2.5 times larger Purcell enhancement compared to the NV-in-waveguide system presented in section 3.4, counting as the RBG

mirror contribution. Fluorescence spectra taken before (uncoupled NV) and after fabrication of the structure (coupled NV) is shown in Figure 4-7(c). In Figure 4-7(d), autocorrelation measurement data taken from the NV center, confirming single-photon emission ($g^2(0) < 0.5$). The solid curve is a double exponential fit.

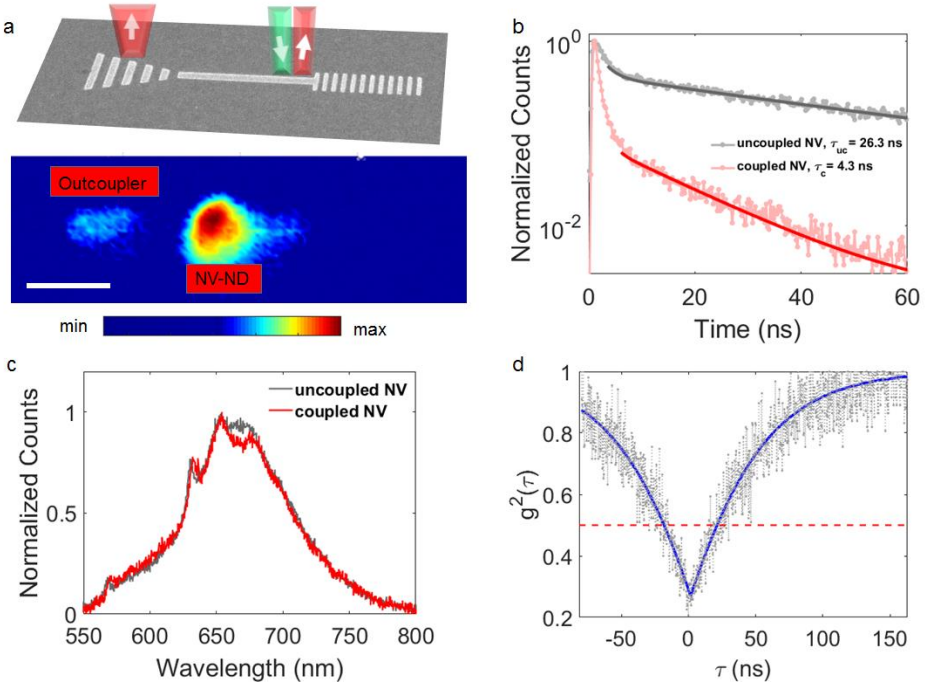

Figure 4-7 Experiment with a single NV center. (a) Galvanometric mirror scan image from the NV coupled system, indicating a unidirectional interaction with propagating SPP mode. (b) Lifetime measurements before (uncoupled NV) and after (coupled NV) coupling to the unidirectional device, indicating a 6-fold shortening in lifetime (from 26.3 to 4.3 ns) for the coupled NV, and 12-fold in total (due to the additional 2-fold reduction for the metal layer1). (c) Fluorescence spectra taken before (grey, uncoupled NV) and after fabrication of the structure (red, coupled NV). (d) Autocorrelation measurement data taken from the NV center, confirming single-photon emission ($g^2(0) < 0.5$). The solid curve is a double exponential fit.

4.4 Unidirectional excitation of a distant GeV center

The dielectric nanoridge structure fabricated on a monocrystalline Au provides a platform to excite a distant GeV color centers, for which the SPP mode excited by the green laser light at the input grating propagates along the waveguide and reaches an embedded ND. The resulting plasmon-emitter interaction directly exchange energy from SPP mode to excite GeV center as shown in Figure 4-8.

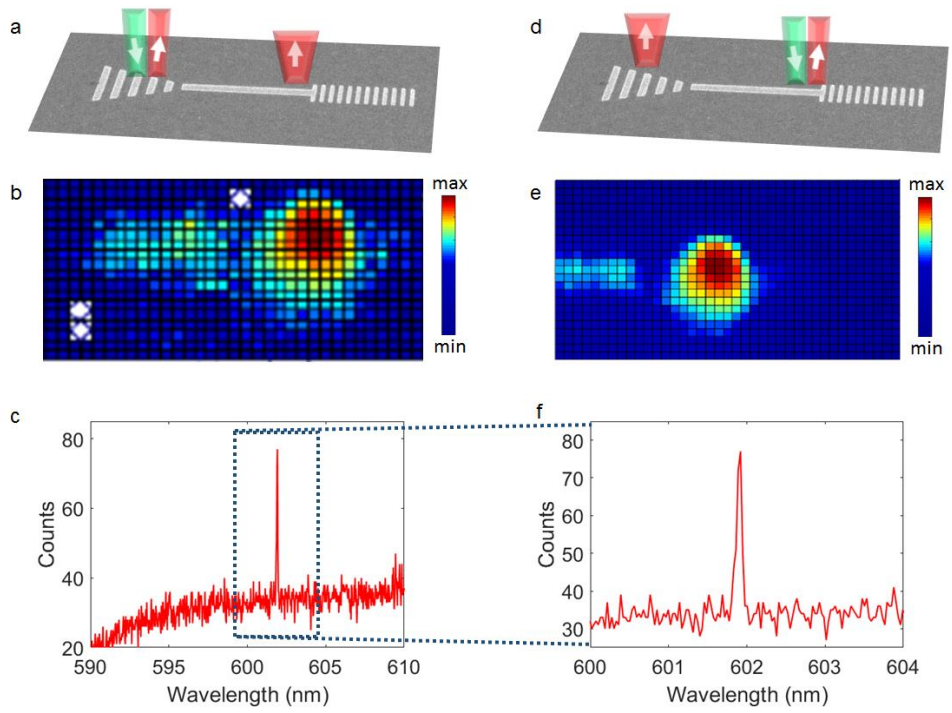

Figure 4-8 (a-c) Unidirectional excitation of a distant Ge-ND. (a) SEM image of the fabricated device. The arrows represent the working principle for the remote excitation of the GeV emitter. (b) Galvanometric mirror scan image from the remote-excited emitter. (c) Fluorescence spectrum taken at low-temperature from the remote-excited GeV center. (d) SEM image of the fabricated device. The arrows represent the working principle for the direct excitation of the GeV emitter. (e) Galvanometric mirror scan image from the direct-excited emitter. (f) A zoomed-in spectrum of the remote-excited GeV center.

4.5 Characterization of DLSPP-based photonic crystal cavity

As discussed in section 4.1, the DLSPPW-based RBG supports a fundamental SPP mode whose effective refractive index varies through the quarter wave stack layers of air/HSQ, creating a number of repeated pairs of low/high refractive index needed to reflect the SPP mode. In this section, a cavity resonator consists of two distributed Bragg mirrors that are integrated with a DLSPP waveguide, is presented. Figure 4-9(a) shows a top view of the cavity structure atop metal layer. The HSQ waveguide ridges have a refractive index of 1.41, and dimensions of w_1 = 250 nm (width) and h = 180 nm (height) as already shown in Figure 4-2(b). The dimensions of the nanoridges in both RBG mirrors are $\lambda_{DLSPP}/4$ in length, and 750 nm in width (w_2), and repeated with a period of $\Lambda = (\lambda_{SPP}/4) + (\lambda_{DLSPP}/4)$ in Figure 4-9(a), where λ_{SPP} and λ_{DLSPP} are the effective wavelengths for SPP and DLSPP

modes, respectively. The length of the HSQ rectangle in Figure 4-9(a) equals one-half of the DLSPP wavelength ($\lambda_{DLSPPW}/2$) in the longitudinal direction, and the gap between the HSQ rectangle and RBG is $\lambda_{SPP}/4$. In Figure 4-9(c), FDTD simulations indicate resonant features inside stopbands, in the cavity transmission, corresponding to different Bragg periods (Λ) of 275 nm (cyan), 300 nm (light green), and 325 nm (dark green). In the simulations, the metal layer (Ag refractive index) was modeled using Palik's data[122].

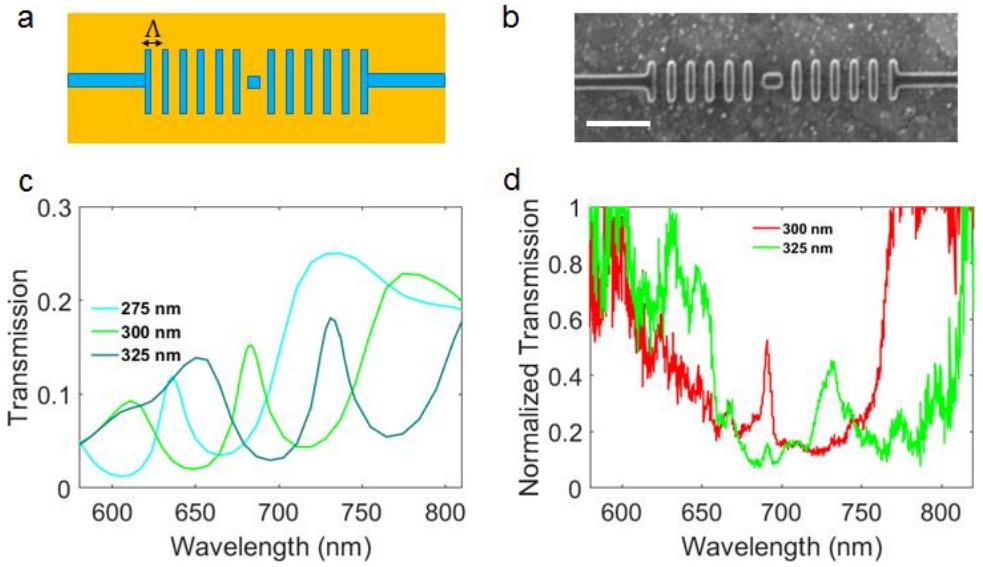

Figure 4-9 Characterization of one-dimensional photonic crystal cavity on metal layer. (a) Top view of the device layout. (b) SEM image of the fabricated device. The scale bar is 1 μm. (c, d) Simulated and measured transmission spectra of the cavity structure for different periodicity of 275 nm, 300 nm, and 325 nm. The height of the HSQ nanoridges is h=180 nm, and the widths are w_1=250 nm (waveguide) and w_2=750 nm (Bragg grating). The metal layer is simulated based on Palik's data[122] for Ag.

In the experiment, a silicon wafer was coated with a Ag film of 250 nm thickness (via thermal evaporation in a vacuum pressure of 2×10^{-7} Torr, and a rate of 4 nm s^{-1}). The HSQ e-beam resist (Dow Corning XR-1541-006) was then spin coated (1200 rpm, 1 min) to make a 180 nm film on the Ag layer and then the cavity structures were fabricated using EBL. SEM image of the fabricated cavity device with the periodicity of 275 nm is shown in Figure 4-9(b). Experimental characterization of the fabricated structures with different Bragg periods (Λ) of 300 nm (red), and 325 nm (green) clearly show the resonant peaks inside the bandgaps of the cavity structures (see Figure 4-9(d)) as predicted by the

simulations. The transmission data in Figure 4-9(d) are normalized to the transmission through a straight waveguide (without Bragg gratings) as explained in Appendix A.5.

4.6 DLSPP-based cavity coupled to a single NV center

NV-centers can be incorporated into the cavity resonators whose resonant wavelength can be selected by appropriately tuning the grating period of the DBRs. In the experiment, a silicon wafer was coated with a Ag film of 250 nm thickness, on which Au markers are made, and subsequently, NV-NDs (Microdiamant MSY 0–50 nm GAF) are spin coated. The sample with dispersed NDs was characterized by scanning in a fluorescence confocal microscope and lifetime, spectrum and autocorrelation measurements are performed for the NV-centers contained in NDs. The HSQ e-beam resist was then spin coated and the waveguide-cavity structure was fabricated using EBL onto the pre-selected ND, which was found to be a single-photon emitter. SEM image of the fabricated waveguide-cavity system is illustrated in Figure 4-10(a).

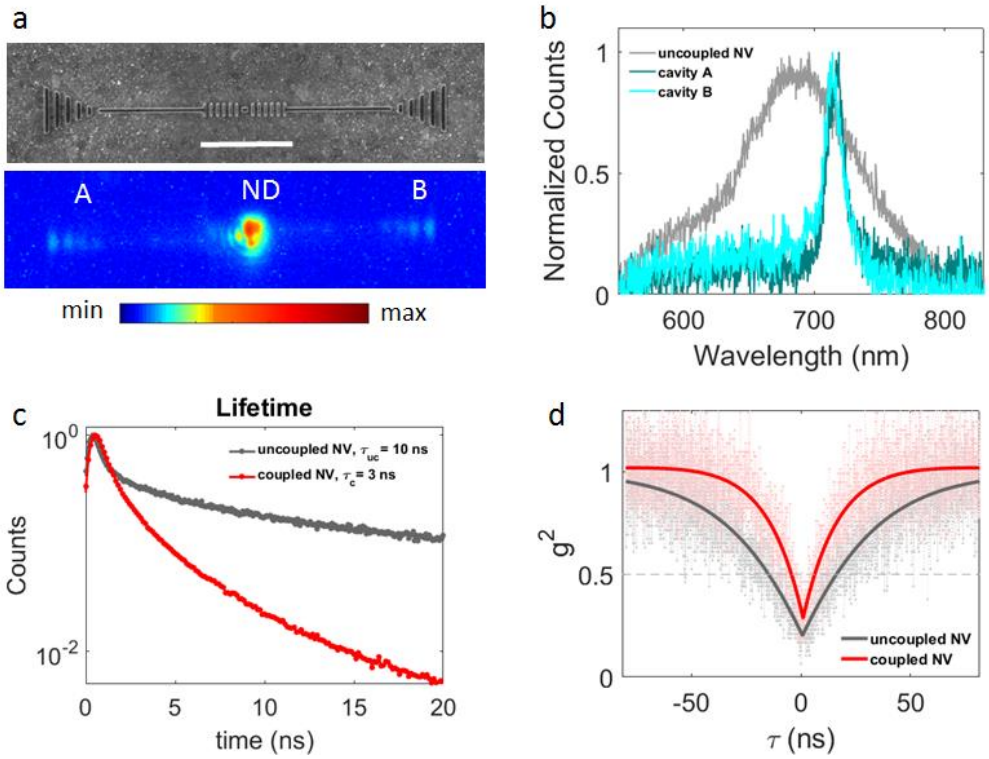

Figure 4-10 Cavity-coupled single NV emission. (a) The SEM image of the fabricated device (top), and the CCD camera image of the whole structure when the ND is excited with a continuous wave (532 nm) laser (bottom). (b) Spectrum taken from uncoupled NV center (grey), and from the coupled NV at out-of-cavity ends of *A* (dark green) and *B* (cyan). (c) Lifetime of the NV-center taken before (grey) and after (red) coupling. (d) Autocorrelation of the NV center before (grey) and after (red) coupling.

Figure 4-10(a, top). CCD camera image in Figure 4-10(a, bottom) shows the coupling of the emitter to the DLSPPW structure, and subsequent emission from the gratings at the two ends. The antibunching dip in the second-order autocorrelation function of the NV-center is observed both before (grey) and after (red) fabrication of the waveguide (Figure 4-10(d), indicating a single-photon emission ($g^2(0) < 0.5$). The experimental correlation data are taken at 30 μw excitation pump power and fitted using a well-stablished model[91]. In Figure 4-10(c), the lifetime of the NV-center before and after coupling is presented. A lifetime reduction (from ~10 ns to ~3 ns) is observed with a single exponential tail fitting of the measured data where the first few ns of the data is avoided in the fitting, as it arises from background fluorescence. On average, the lifetime is decreased by a factor of ~2.5 ± 0.5, in addition to the 2-fold reduction due to the Ag surface, and gives a factor of ~5

± 1 for the total decay rate enhancement of a broadband NV emitter coupled to the waveguide (Γ_{tot}/Γ_0). This enhancement is similar in magnitude to the enhancement observed for a straight waveguide. This is expected because the emission from the NV-center is much broader than the cavity resonance peak[134-136]. For the NV center in a cavity, the emission is enhanced at the cavity resonance, and suppressed in the stopband of RBG. Figure 4-10(c) shows the emission spectra obtained from the uncoupled NV center (grey), and from the coupled NV at out-of-cavity ends of *A* (dark green) and *B* (cyan). The fluorescence spectra from the ends show significant modifications that can be related to the transmission spectrum features of the device. This gives a *Q* factor of ∼70 for the fabricated cavity, i.e. ∼10 nm full width at half maximum (FWHM). The emission intensity at the cavity resonance, I_r, is notably higher (by ∼2.5 times) than the intensity outside of the stopband I_{out}. Compared with the transmitted intensity on resonance, T_r, measured by the supercontinuum laser, and that outside of the stopband, T_{out}, this gives a 6 ± 1 fold radiative decay rate enhancement due to the cavity on resonance (Γ_r) using $\Gamma_r = (I_r/I_{out})(T_{out}/T_r)$, where I_r, and I_{out} are normalized with the baseline fluorescence emission of the NV-center[136].

In Figure 4-11, the narrow band enhancement of a cavity is compared with a reference straight waveguide, which shows a 6-fold enhancement for the cavity resonance peak at ZPL due to the finesse of the cavity. This narrowband enhancement ($\Gamma_r = 6 \pm 1$), combined with the broadband enhancement ($\Gamma_{tot}/\Gamma_0 = 5 \pm 1$), results in the overall decay rate enhancement ($\Gamma = \Gamma_r\Gamma_{tot}/\Gamma_0$) being as high as 42 at the cavity resonance peak.

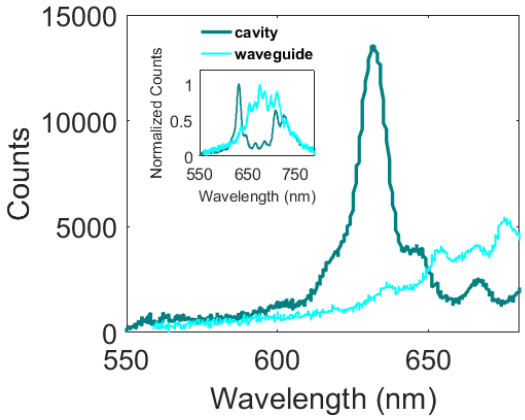

Figure 4-11 Narrowband enhancement of the emission rate for the DLSPP cavity-coupled NV (green) compared with DLSPP straight waveguide (cyan). The result indicates a 6-fold enhancement due to the cavity fineness. Inset shows the broadband emission of NV-center coupled to DLSPP waveguide (cyan), and cavity (dark green), respectively.

In the simulations, the overall decay rate at the cavity resonance was decomposed into two components associated with the longitudinal and transverse confinements. The SPP propagation length (L_{SPP}) at the cavity resonance wavelength can be obtained from the relation $L_{SPP} = Q \cdot \lambda_{SPP}/2\pi$, in which λ_{SPP} is the effective SPP wavelength[136]. The Q factor is calculated from FDTD simulations, and λ_{SPP} from the effective mode index using FEM method[120], and thereby L_{SPP} is deduced to be ~7.5 μm (λ = 680 nm). This length is less than the value of 20 ± 5 μm estimated for the NV-DLSPPW system length in Section 3.3, due to the presence of the quarter wave stack in the longitudinal direction of the proposed cavity structure. The longitudinal enhancement (Γ_{long}) of the plasmonic cavity is then given by L_{SPP}/L_{eff}, where L_{eff} is the effective cavity length and can be obtained from the effective mode volume (~0.18 $(\lambda_{SPP})^3$) and the effective area of the SPP mode (~0.12 $(\lambda_{SPP})^2$)[136]. This gives the longitudinal enhancement to be 7 ± 1 (the number of roundtrips of a single plasmon in the cavity). The enhancement associated with the lateral confinement (Γ_{trans}) by simulating the total decay rate (Γ_{tot}/Γ_0) as explained in Section 3.3 and obtain a value in the range of 4–7.5 for the lateral enhancement using $\Gamma_{trans} = \Gamma_{tot}/\Gamma_0$. Combining these two factors ($\Gamma = \Gamma_{long}\Gamma_{trans}$), an up to 60-fold spontaneous emission enhancement at the cavity resonance is estimated in overall. The difference in simulated and experimentally observed enhancement at the resonance wavelength can be due to the

differences in position and alignment of NV-center dipoles or quantum efficiency of NV being below one. The influence of NV-center position on the lateral plasmonic decay rate (Γ_{pl}/Γ_0) and the longitudinal enhancement (Γ_{long}) is shown in Figure 4-12.

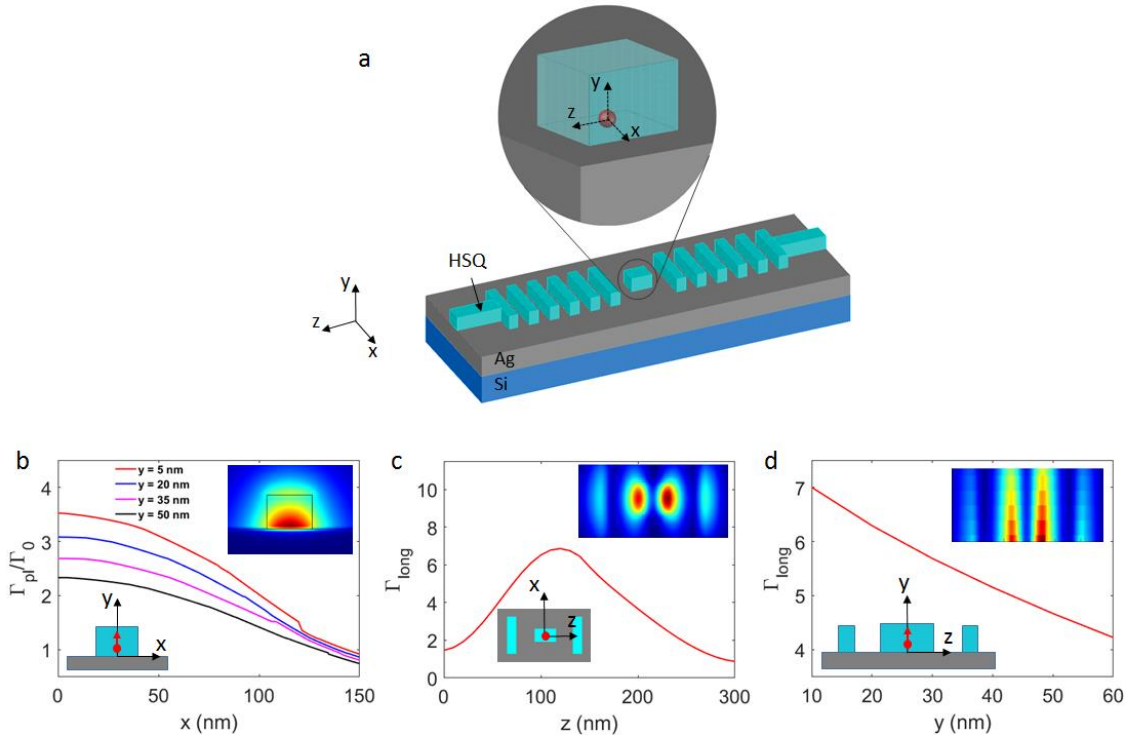

Figure 4-12 Position dependence of the plasmonic decay rate for the DLSPP cavity-coupled NV emitter with a vertically oriented dipole (*y*-polarized) (a) Schematic of the device layout. (b) Simulated plasmonic decay rate enhancement of coupled NV due to the lateral confinement of DLSPP rectangle waveguide (Γ_{pl}/Γ_0) when emitter's position changed along *x* axis for different *y* positions. Inset shows the distribution profile of the plasmonic decay rate for the DLSPPW coupled NV center in *xy*-plane. (c) Plasmonic decay rate enhancement coupled NV due to the longitudinal confinement of Bragg cavity (Γ_{long}) for when emitter's position changed along *z*-axis (y=25 nm, x=0 nm). Inset shows the distribution profile of longitudinal plasmonic decay rate for the cavity coupled NV center in *xz*-plane. (d) Influence of NV position on longitudinal enhancement when emitter moved along *y*-axis. Inset shows the distribution profile of longitudinal plasmonic decay rate for the cavity coupled NV center in *yz*-plane.

Full tunability of the stopband and cavity over the entire emission range of the NV-center is ensured by varying the periodicity of the RBG as explained before in simulated and measured transmission data (see Figure 4-9). In the experimental results shown in Figure 4-13, the quarter wave stack period is designed to tune the cavity resonance in our

desired wavelengths including the ZPL of NV (λ = 637 nm, Figure 4-13(a)), the NV emission peak (λ = 680 nm, Figure 4-13(b)), and the ZPL of SiV (λ = 737 nm, Figure 4-13(c)). Emission into the ZPL is important for the photon-mediated entanglement of internal quantum states of multiple emitters[108]. The proposed cavity-coupled system gives us an opportunity to enhance the emission properties of other colour centers in diamond, and in particular the narrow-band SiV and GeV centers as shown experimentally in Sections 4.7 and 4.8.

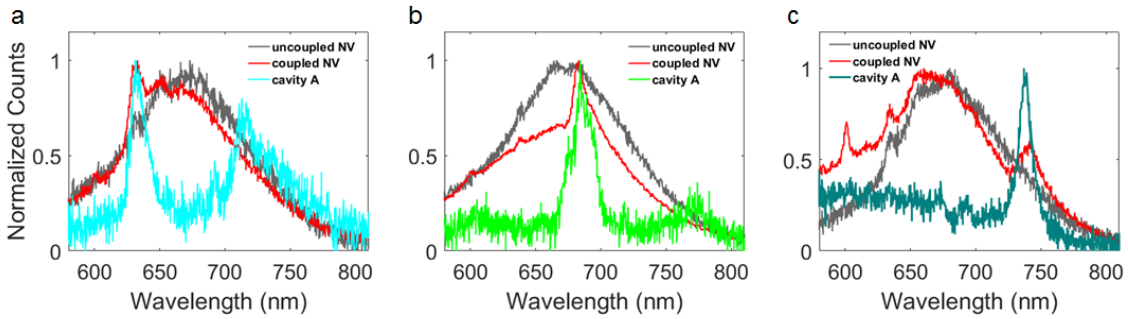

Figure 4-13 Tunable narrowband Bragg grating cavity. (a-c) Experimental results for the cavity-coupled NV emitter for different Bragg periods (Λ) of 275 nm (cyan), 300 nm (light green), and 325 nm (dark green) corresponding to the NV-ZPL (a, λ = 637 nm), the NV emission peak (b, λ = 680 nm), and the SiV-ZPL (c, λ = 737 nm), respectively.

4.7 DLSPP-based cavity coupled to a SiV center

In the experiment, a ND with a SiV center is characterized (Figure 4-14, grey) and coupled to the cavity (Figure 4-14, red) that is designed to resonate at the ZPL of SiV. Spectra taken from the grating outputs, end A (dark green) and end B (cyan), indicating a FWHM of ~10 nm (Q = 74) for the cavity structure.

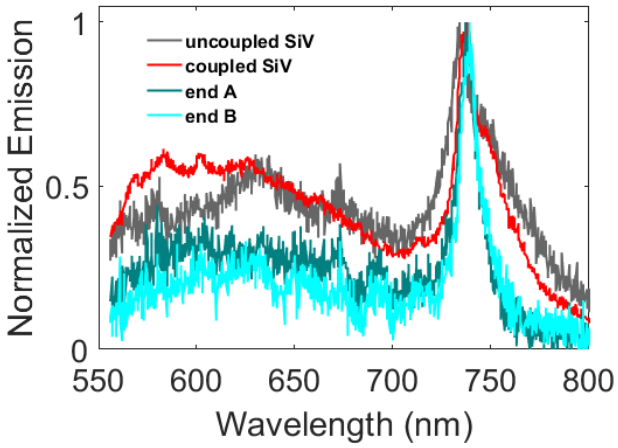

Figure 4-14 Cavity-coupled SiV emission. Out-of-cavity emission spectra measured from grating outputs (end A and end B) indicate a FWHM of ~10 nm (Q = 74) for the cavity structure.

4.8 DLSPP-based cavity coupled to a GeV center

In the experiment, a ND with dual color center (tentatively dual-charge state GeV center) with ZPLs at 602 nm (GeV negative charge state) and 619 nm (tentatively GeV neutral charge state[137]) is characterized as shown in Figure 4-15 (d, grey line). A Bragg cavity is designed and fabricated to selectively enhanced the GeV negative charge state by tuning the cavity resonance at λ= 602 nm as shown in Figure 4-15 (d, red line). Simulated reflection (dotted black line) and transmission (red line) for the designed cavity is shown in Figure 4-15(b). Lifetime shortening from 11.9 ns (grey) to 3.8 ns (red) is achieved after coupling to the cavity resonance as shown in Figure 4-15(c).

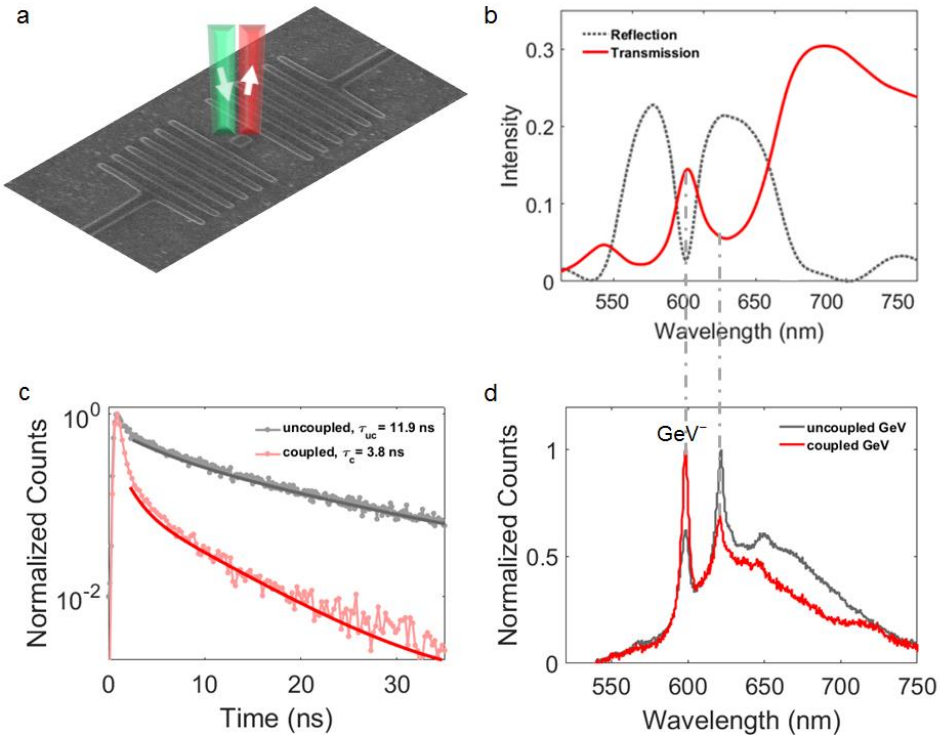

Figure 4-15 Cavity-coupled a dual color center. (a) Schematic of the cavity device composed of two RBG mirrors placed in front of each other at a distance of one wavelength and ND at the constructive interference point. (b) Simulated reflection (dotted black line) and transmission (red line) for the cavity designed to resonate at λ= 602 nm (GeV-ZPL). (c) Lifetime shortening from 11.9 ns (grey) to 3.8 ns (red) is achieved after coupling to the cavity resonance. (d) Fluorescence spectra taken from the emitter before (grey) and after (red) coupling to the cavity.

Chapter 5: Conclusions and outlook

In this thesis, nanofabrication of photonic components based on DLSPPWs excited by single color centers (NV, SiV, and GeV) in NDs has been demonstrated. The extraordinary long propagation length for the green pump laser has been achieved with DLSPPWs on Ag crystals, enabling thereby the remote excitation of GeV centers through propagating DLSPPW mode in a plasmonic chip. The main advantage of remote excitation is that propagating SPPs can directly interact with GeV center and exchange energy. This opens the way for the integration of an excitation laser, QE and plasmonic circuit on the same chip. The performance of the GeV–DLSPPW hybrid system with respect to efficient single-photon transmission has been quantified with the FOM of 180 by a ~six-fold Purcell enhancement, ~56% coupling efficiency and ~33 μm transmission length, which indicates a superior performance in comparison with the previously demonstrated systems.

Furthermore, single GeV centers in diamond nanocrystals have been investigated at low temperature, indicating symmetry-protected and ultrabright (> 2×10^6 counts/s at saturation) zero-phonon optical emission. A large energy split of 870 GHz in the ground state has been determined for the GeV centers in highly strained ND samples, that is ~6 times larger than that in bulk diamonds. An integrated crystalline Au-based nanophotonic

platform has been realized, on which GeV centers in NDs interface with highly confined SPP modes, resulting in a remarkable 10-fold Purcell enhancement in a unidirectional manner,. The unidirectional interaction enables efficient guiding control of the emitted single photons, revealing the potential of this approach for realizing entanglement between an optical photon and a spin qubit.

Finally, a DLSPPW-based cavity coupled to a diamond-based NV emitter has been demostrated, achieving an up to 42-fold decay rate enhancement of spontaneous emission at the ZPL. The plasmonic configuration described features such as enhanced total decay rate and improved spectral purity of the coupled NV emitter, thereby promising potential applications in on-chip realization of quantum-optical networks.

Outlook

Further enhancement of the Purcell factor is possible by using a larger refractive index dielectric (e.g., TiO_2 with a refractive index of ~2.4 at the wavelength of 600 nm) with smaller dimensions in the DLSPPW cross section. This way can potentially increase plasmonic decay rate about 10 times, from ~4.5 for HSQ-made waveguide to ~45 for TiO_2 waveguide as shown in Figure 5-1.

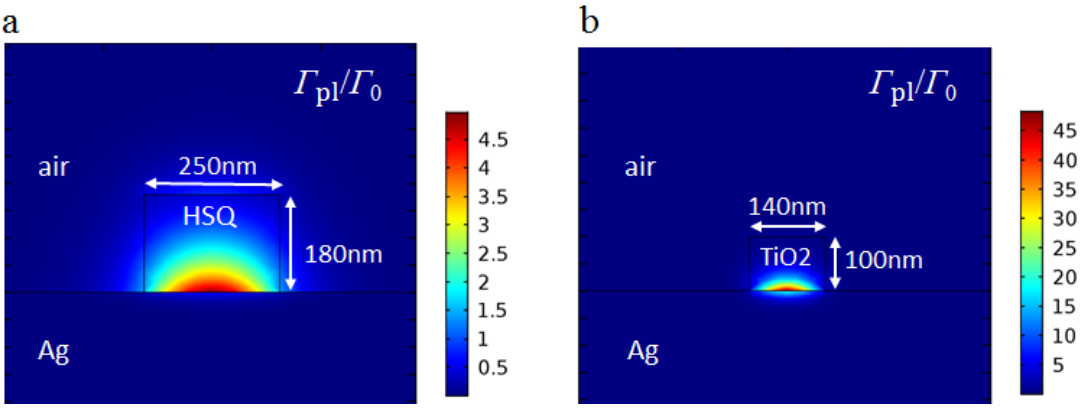

Figure 5-1 Plasmonic decay rate (Γ_{pl}/Γ_0) of the GeV-coupled DLSPPW system. (a) HSQ waveguide with dimensions of 180 nm by 250 nm, and refractive of index n = 1.4, (b) TiO_2 waveguide with smaller dimensions of 100 nm by 140 nm, and larger refractive index of n = 2.4.

Furthermore, the on-chip excitation approach can be further expanded to include several QEs that can be excited simultaneously, micometers away from excitation spot

and has great potential for integration of laser source and single-plasmon nanocircuits. This ability provides great flexibility in designing functional plasmonic structure. The demonstrated DLSPPWs on single crystalline Ag plates provide the largest reported propagation length for green light and can be further expanded by interfacing DLSPPW and photonic waveguide[21,138,139], and eventually coupling to an optical fibers as shown in Figure 5-2.

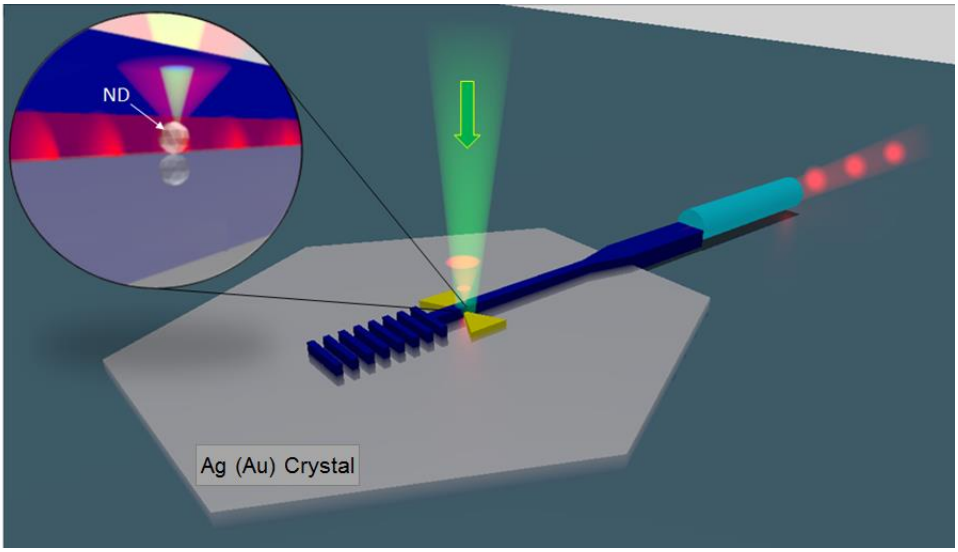

Figure 5-2 Schematic of a DLSPP waveguide coupled to a dielectric waveguide and eventually to an optical fiber.

A. Appendices

A.1 Growth of nanodiamonds

Imitating the natural formation of diamonds underneath the Earth, diamond crystals were grown at the scale of nanometer, under a HPHT condition, and Ge defect atoms were added during the growth in a hydrocarbon metal catalyst-free system based on homogeneous mixtures of naphthalene $C_{10}H_8$ (Chemapol) with tetraphenylgermanium $C_{24}H_{20}Ge$ (Sigma-Aldrich)[133]. The synthesis was performed in a high-pressure apparatus of the Toroid type. Cylindrical samples of the initial material (5 mm diameter and 3 mm height) obtained by cold pressing were put into graphite containers, which also served as a heater for the high-pressure apparatus. The experimental procedure consisted in loading the apparatus up to 8 GPa, heating up to the synthesis temperature and short isothermal exposure under constant load for 1-5 s. The obtained diamond products are then isolated by quenching to room temperature under pressure. The recovered samples have been characterized by X-ray diffraction, Raman spectroscopy, SEM and TEM. The results of such characterization of the obtained products, which are mixtures of nano- and submicrometer-size fraction of diamond, show high, practically 100%, yield in the formation of diamond. Size-fractional separation of diamonds was carried out in several

stages that consisted of ultrasonic dispersing of the diamond particles using UP200Ht dispersant (Hielscher Ultrasonic Technology), chemical treatment of the samples in mixture of three acids (HNO_3-$HClO_4$-H_2SO_4), and subsequent centrifugation of aqueous or alcohol dispersion of diamond powders. TEM and SEM images of the synthesized NDs are illustrated in Figure A-1.

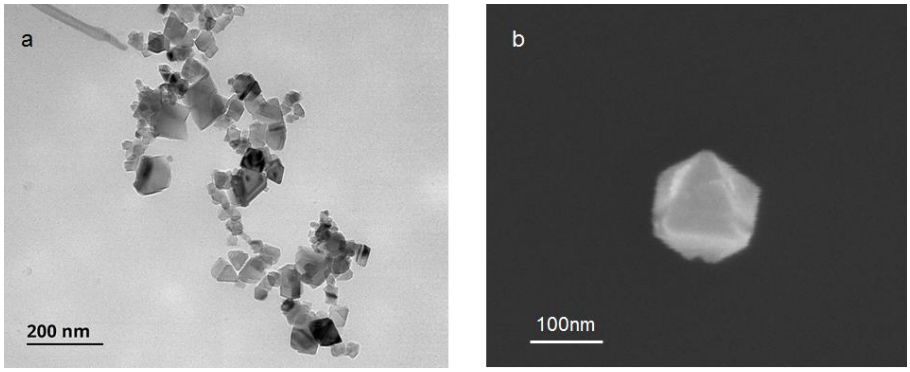

Figure A-1 HPHT diamond nanocrystals containing GeV color centers. (a) TEM image. (b) SEM image. The images are taken after the chemical and ultrasonic treatment. Chemical treatment was carried out with three highly concentrated acids, HNO_3, $HClO_4$ and H_2SO_4 (at 200 °C for 3 h), to remove traces of graphite. The ultrasonic treatment was done with a UP200H device (Hielscher).

A.2 Confocal optical setup

The experimental set-up used for the room-temperature characterization of QEs in NDs and their coupling to DLSPPWs is presented in Figure A-2.

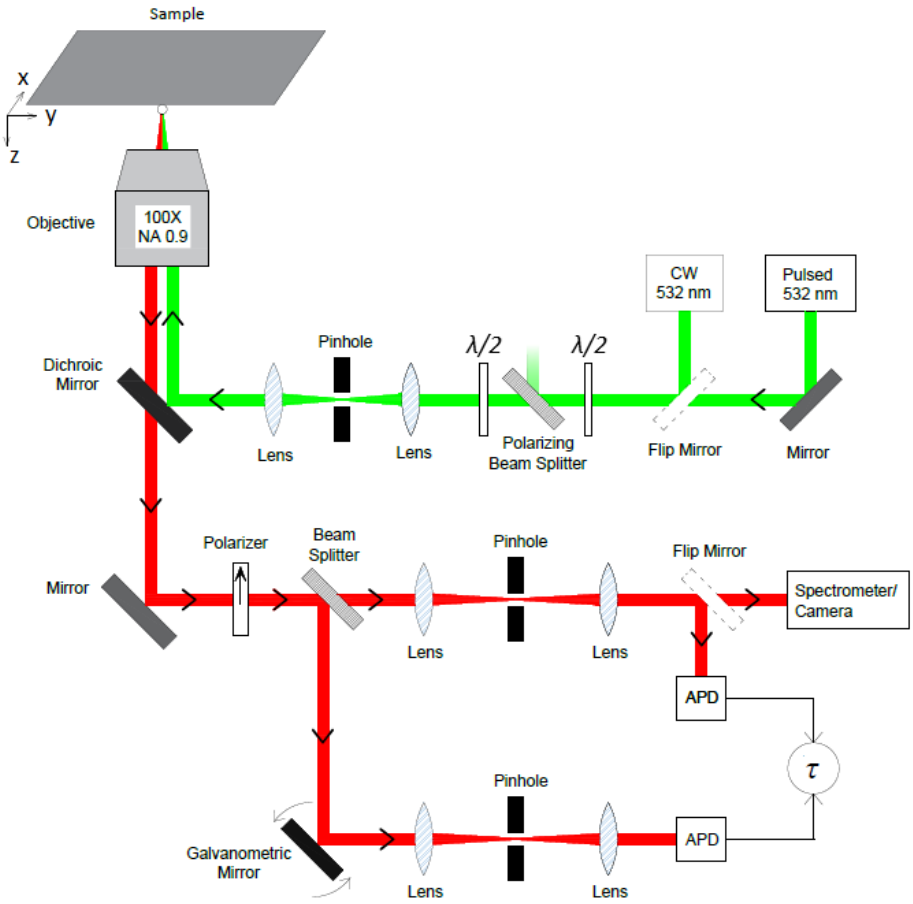

Figure A-2 Schematic of experimental setup for quantum measurements. Green line indicates excitation path from 532 nm continuous-wave (CW) or pulsed lasers (chosen by a flip mirror (FM)) onto the sample, which is focused by a 100× (NA 0.90) objective. The pump polarization is controlled by a halfwave plate in the excitation light path. The fluorescence light, indicated by red line, is collected by the same objective, and passed through a dichroic mirror (DM), polarizer (analyzer) and then BS. The analyzer introduced in the detection path probes the polarization of emitted photons. When illuminated by a CW laser, the emission from a single QE is split into two channels through the beam-splitter and then detected by two identical avalanche photodiodes (APDs) where one can record time delay across the APDs to generate an intensity autocorrelation signal $g^2(t) = \langle I(t')I(t'-t)\rangle$. Lifetime measurements are performed using pulsed excitation with pulse width/period of ~50 ps/400 ns. Postfabrication measurements are performed to show coupling of the emitter to the DLSPP waveguide where the ND is excited and a fluorescence image of the focal plane is taken by either a charge-coupled device (CCD) camera or a galvanometric mirror scan. Fluorescence spectrum of GeV-waveguide system is taken by a grating spectrometer.

For the low-temperature measurements, the sample was loaded on the cold-finger of a continuous flow helium cryostat (as shown in Figure A-3), which was cooled to 4.7 K for confocal microscopy measurements. Schematic of the cryogenic setup for confocal microscopy is illustrated in Figure A-4. Experimental control was provided by the Qudi software suite[140]. The GeV centers were off resonantly excited by linearly polarized 532 nm green laser to map the fluorescence of GeV ZPL. Band pass filter (599/13 nm) was placed in front of the APD. Spectra were measured after a 560 nm long pass filter.

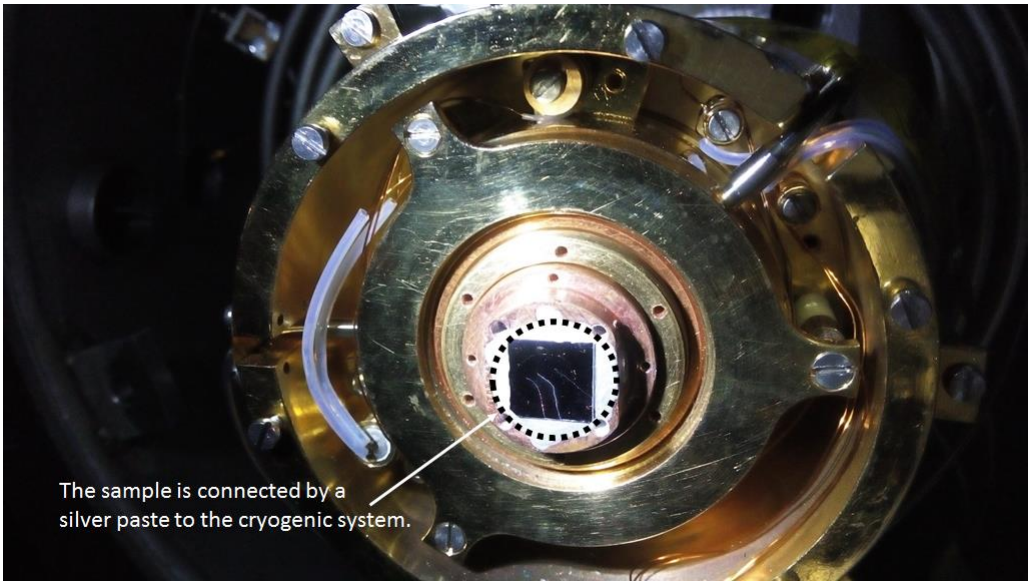

Figure A-3 A photo taken from the sample when it is loaded on the cold-finger of a continuous flow helium cryostat. The sample is connected to the cryogenic system by an Ag paste.

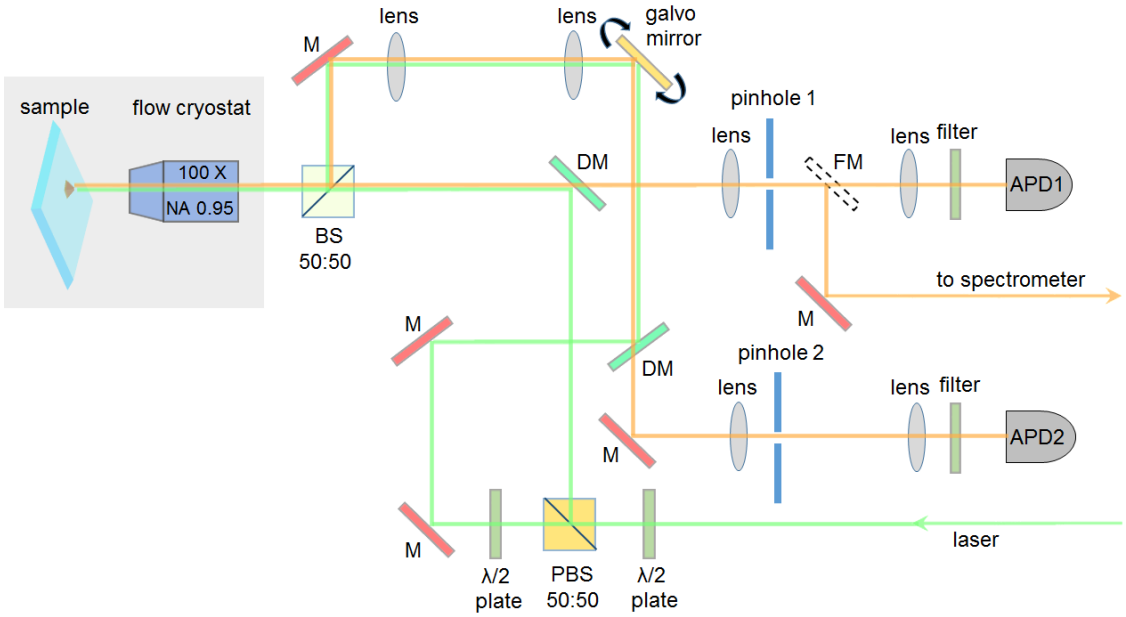

Figure A-4 Schematic of the cryogenic setup for confocal microscopy at low temperature. M: Mirror, BS: Beam splitter, DM: Dichroic mirror, FM: Flip mirror, PBS: Polarizing beam splitter, APD: Avalanche photodiode, NA: Numerical aperture.

A.3 Synthesis of colloidal gold crystals

Au monocrystalline flake samples were obtained following the modified Brust–Schiffrin method[141], for colloidal Au synthesis via thermolysis. As described in ref 113, an aqueous solution of chloroauric acid ($HAuCl_4 \cdot 3H_2O$), in concentration of 0.5 g/mol, was used as the precursor and mixed with a solution of tetraoctylammonium bromide (TOABr) in toluene. After stirring for 10 minutes at 5000 rpm, the mixture was left in rest for 10 minutes, allowing aqueous and organic phases to separate. Simultaneously, the substrate was prepared: a silicon substrate was cleaned by ultrasonication in acetone, isopropyl alcohol (IPA) and ultrapure water (Milli-Q). After drying with nitrogen gas, the substrate was pre-baked on a hot plate at 200°C for approximately 5 minutes for dehydration purposes. In the following step, few microliters of the organic phase were drop-casted onto a substrate, which was then kept on the hot-plate at 150°C for 1 hour. After that, the sample was cleaned in toluene at 75°C temperature, acetone and IPA. As a result, sample contains wide variety of plate-like Au crystals, as shown in Figure A-5.

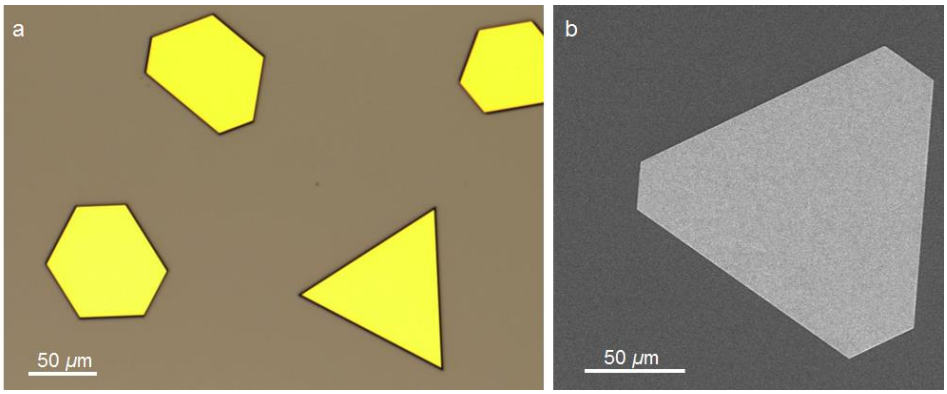

Figure A-5 Synthesized crystalline Au flakes. (a) Optical microscope image. (b) SEM image.

A.4 Device fabrication

For the top-down nanofabrication, direct e-beam writing was performed using a negative tone e-beam resist comprised of 6% solution of HSQ diluted in methyl isobutyl ketone (MIBK) solvent (Dow Corning XR-1541−006). Using a standard spin-on coating equipment, HSQ was deposited on the substrate with the speed of 1200 rpm (1 min), and subsequently the solvent was boiled off during a hotplate bake process (170^{o}C, 2 min). This resulted in a 180 nm film on Au crystal flakes. Using a single exposure tool with 30 KeV beam energy and area doses from 400 to 700 μC/cm^2, the HSQ film was patterned, with capability to define features as small as 6 nm, and nanoridge waveguides were defined and accurately positioned onto preselected NDs, whose locations were determined with respect to the specifically designed and prefabricated alignment markers. Then, the HSQ film was developed in tetramethylammonium hydroxide (Sigma-Aldrich, 25 wt. percentage solution in water), a standard aqueous base developer. After the development, HSQ turned to silicon dioxide (SiO_2). For fabrication of the markers, a positive tone e-beam resist of 950 polymethyl methacrylate (PMMA) A4 (MicroChem) was used.

A.5 Far-field measurements

Far-field characterization of the DLSPP waveguide-integrated cavities for two different Bragg wavelengths of $\lambda = 680$ nm (NV^- emission peak) and $\lambda = 737$ nm (SiV center, ZPL) are illustrated in Figure A-6, and Figure A-7, respectively. The transmission is measured using a super continuum source to excite one grating end, whereas the other one monitor the transmission of the guided SPP mode through the structure. The transmission data for each device is normalized to the average transmission through a set of DLSPP straight reference waveguides (Figure A-6(a)) that are patterned on the same sample and measured under the same coupling conditions. The transmission through the straight waveguide is influenced by the propagation loss and the grating coupler efficiency.

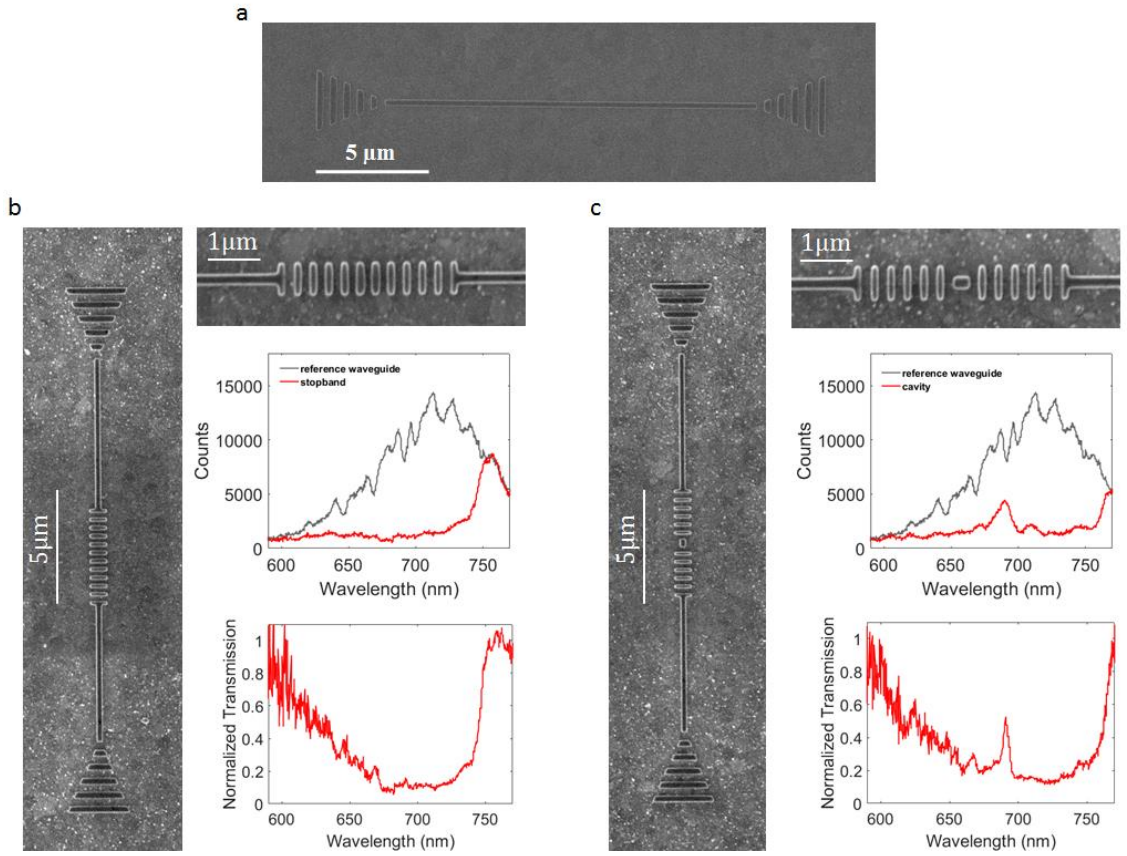

Figure A-6 Far-field characterization of DLSPP waveguide-integrated cavity. (a) SEM image of a straight DLSPP waveguide (reference waveguide). (b) SEM image of a DLSPPW-based reflecting Bragg gratings (RBG, left), transmission data for reference waveguide and RBG (top right), and normalized transmission of RBG (bottom left). (c) SEM image of a DLSPPW-based cavity (left), transmission data for reference waveguide and cavity (top right), and normalized transmission of cavity (bottom left). The quarter wave stack period of 300 nm is designed to have resonance at λ=680nm (NV^- peak).

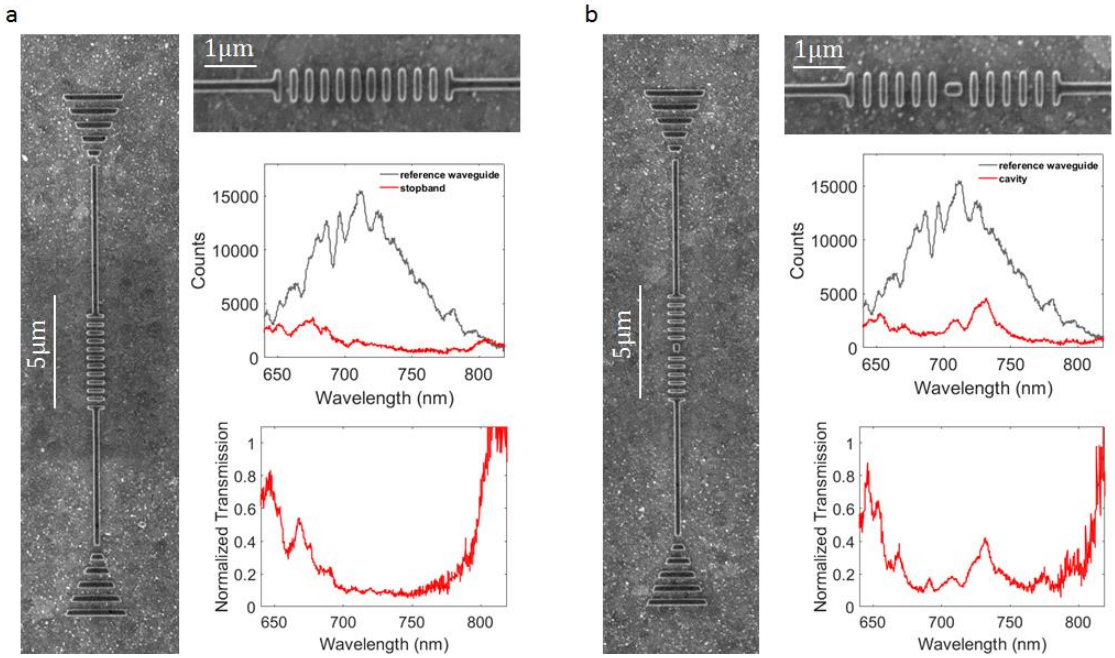

Figure A-7 Far-field characterization of DLSPP waveguide-integrated cavity. (a) SEM image of a DLSPPW-based distributed Bragg reflector (left), transmission data for reference waveguide and RBG (top right), and normalized transmission of RBG (bottom left). (b) SEM image of a DLSPPW-based cavity (left), transmission data for reference waveguide and cavity (top right), and normalized transmission of cavity (bottom left). The quarter wave stack period of 325 nm is designed to have resonance at $\lambda = 737$nm (SiV, ZPL).

A.6 Near-field measurements

SNOM measurements was performed with a titanium sapphire laser source (wavelength 775-1000 nm). Because the SNOM setup was operating in a transmission configuration with sample illuminated from below, a grating was fabricated in the Au layer for efficient excitation of plasmonic mode (see schematic in Figure A-8). An SEM image of the fabricated device and an AFM image of the excitation point are shown in Figure Figure A-8(b) and Figure A-8(c), respectively. The RBG mirror period was modified to produce strong back-reflection at the central operating wavelength (Figure A-8(e), $\lambda = 850$ nm), while no reflection was observed outside the TM bandgap (Figure A-8(f), $\lambda = 1000$ nm). Mode parameters (effective mode index, propagation length, and reflection coefficient) were extracted from near-field maps, obtained for different laser wavelengths, using a simple fitting procedure[142-145]. The resulting SNOM measurements indicate ~80% reflectance from the RBG mirror (Figure A-8(g)).

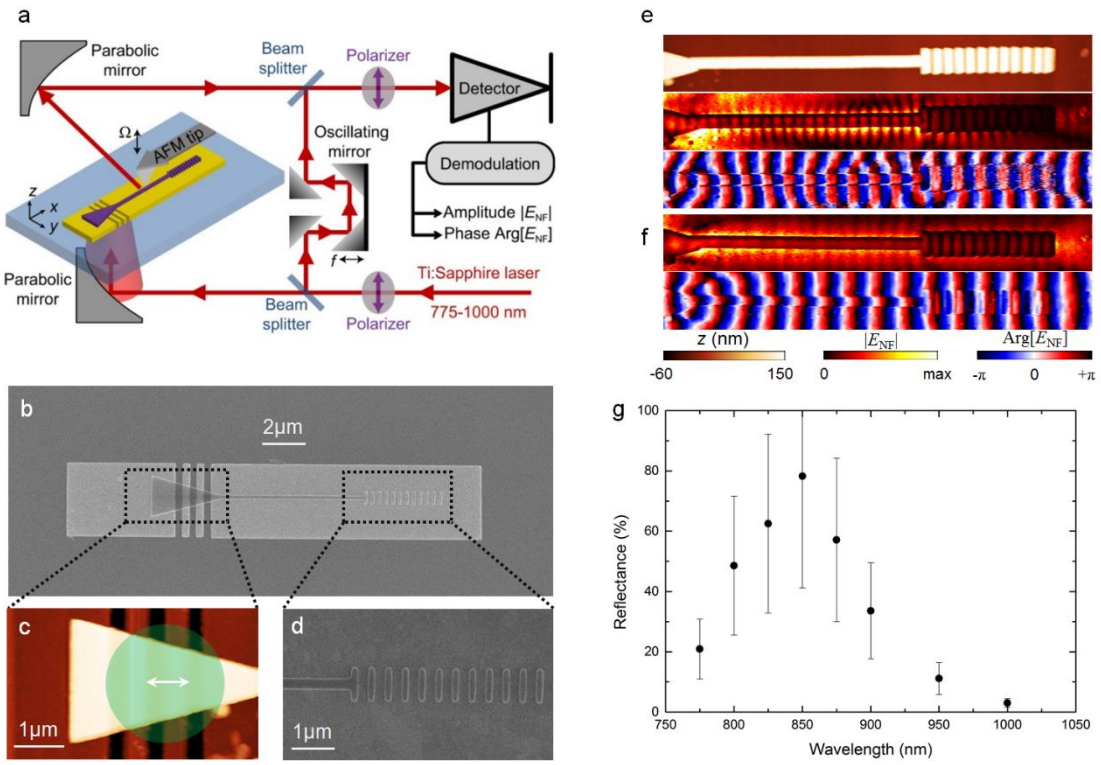

Figure A-8 Near-field investigation of the RBG mirror (a) Schematic of the near-field optical setup. (b) SEM image of the fabricated device, namely dielectric nanoridge atop a patterned Au rectangular layer. (c) AFM image of the input grating, overlapped with dielectric funnel for excitation of DLSPP mode. Green circle and white arrow illustrate approximate position of incident illumination spot (not to scale) and its polarization, respectively. (d) Zoomed-in SEM image of RBG. (e, f) Topography z (top), near-field amplitude $|E_{NF}|$ (middle), and phase Arg $[E_{NF}]$ (bottom) of the unidirectional SPP coupler, recorded at λ = 850 nm (e, inside the TM bandgap) and λ = 1000 nm (e, outside the TM bandgap). (g) Reflectance of RBG, evaluated from SNOM maps.

A.7 Simulated characteristics of GeV-DLSPPW configuration

The emitter's decay rate (Γ_{pl}) into the plasmonic mode guided by a metallic waveguide along z direction can be calculated using $\Gamma_{pl}/\Gamma_0 = [3\pi c\varepsilon_0|\boldsymbol{E}(x,y).\hat{\boldsymbol{n}}_D|^2]/[2k_0^2\iint S_z(x,y)dA]$, where $\boldsymbol{E}(x,y)$ is the electric field associated with the guided plasmon mode, $\hat{\boldsymbol{n}}_D$ is a unit dipole embedded in the waveguide at position (x, y), c is the speed of light in vacuum and k_0 denotes the propagation constant in free space. Also, Γ_0 represents the spontaneous emission decay rate in vacuum and S_z denotes the z component of the average of the instantaneous Poynting vector, i.e. $\langle \boldsymbol{S} \rangle = \frac{1}{2} Re(\boldsymbol{E} \times \boldsymbol{H}^*)$, in which $\boldsymbol{H}^*$ denotes the complex conjugate of the magnetic field associated with the guided plasmon mode as formulated in ref 120. In simulations, the emitter's decay rate into the plasmonic mode guided by the DLSPP waveguide was calculated using 2D FEM method. The emission coupling efficiency, $\beta = \Gamma_{\mathrm{pl}}/\Gamma_{\mathrm{tot}}$, where Γ_{tot} is the total decay rate is simulated by a 3D FEM model with scattering boundaries surrounding the computational domain using COMSOL Multiphysics software. The total decay rate is extracted from the total power dissipation of the coupled emitter as explained in refs 120 and 121. Polarization selectivity of the GeV-DLSPPW configuration is simulated by modeling the GeV emitter with a unit dipole that can be oriented in three different axes of x, y, and z. The results are shown in Figure A-9.

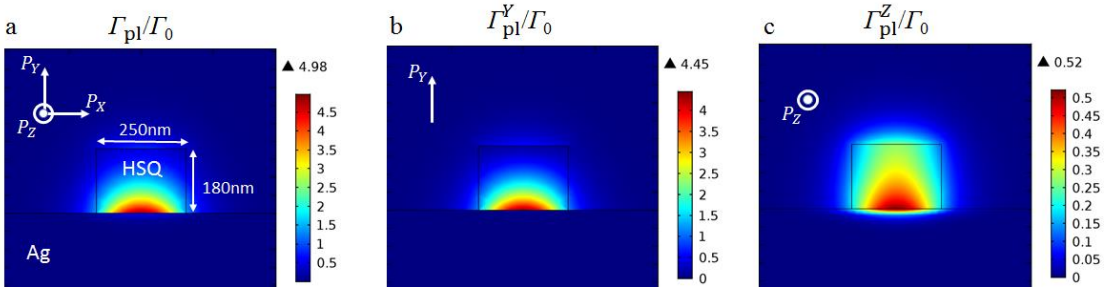

Figure A-9 Simulated plasmonic decay of coupled GeV center for different polarization axes. (a-c) Plasmonic decay (Γ_{pl}/Γ_0) of GeV emission to the fundamental TM mode of the DLSPP waveguide is maximized for the polarization axis normal to the Ag plane, i.e. y-axis (b). There is also a ~10% contribution from in-plane polarization axis along the waveguide axis (z-axis) to the DLSPPW mode (c) which can be added efficiently in the plasmonic decay by proper alignment of the waveguide axis along the dominant dipole component (e.g. along $\theta = \pi/6$ in the GeV-ND shown in Figure 2d in the manuscript). Dipole axis has similar effect on β-factor (Γ_{pl}/Γ_0), i.e. the main contribution is belong to the normal axis (y-axis) polarization.

The reflection and propagation losses of the grating out-coupler of the waveguide is simulated, resulting in the reflection around 8% at 600 nm and propagation losses (due to the absorption through the grating) around 12% (Figure A-10). This gives a ~80% out-coupling efficiency. For the estimation, the reflection loss ($|R|$) is formulated using $I = |E_{in} + E_r|^2$, where $E_{in} = E_0 exp(-ikx)$, $E_r = E_0 exp(-ikL) R. exp(-ik(L-x))$, and L is 2.8 μm. Also, k and E_0 denote the wavenumber, and the incident field, respectively. The simulation is performed based on Palik's data[122] for modeling of Ag plate and therefore provides an overestimation for the propagation losses of crystalline metal flakes. For the grating structure that is made on Ag crystal, 4% losses due to the propagation is estimated, and therefore 88% out-coupling efficiency is achieved.

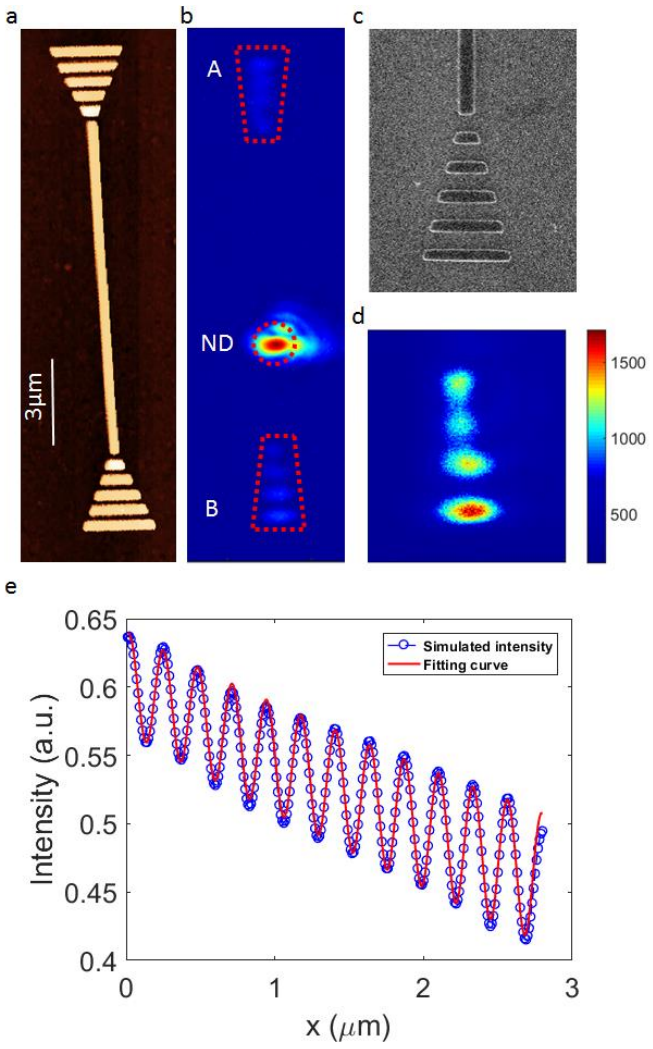

Figure A-10 Reflection and propagation losses of the grating out-coupler. AFM image of the fabricated waveguide on Ag flake (a), and CCD camera image of the whole structure where the ND is excited and a fluorescence image of the focal plane is taken (b). The 1/e propagation length, L_P, is extracted from the fluorescence signals at the two ends using $P_A/P_B = \exp[(L_A - L_B)/L_P]$, in which L_A = 8 μm and L_B = 4 μm, assuming symmetric coupling in two directions, uniform losses across the waveguide and the same out-coupling efficiency at the grating ends. The collected data are fitted to obtain the propagation length of 33 ± 3 μm for the GeV-DLSPPW hybrid system on Ag crystal flake that is even higher than the NV- DLSPPW system on Ag film, indicating a low material loss for the single crystalline Ag flakes. (c, d) SEM image of the grating outcoupler and the corresponding CCD image. (e) Simulated intensity I (blue) at the distance of x from the waveguide end to the beginning of the outcoupler).

The waveguide-GeV system in a DLSPPW configuration is simulated at room and low temperatures, indicating a larger coupling efficiency at low temperature due to the

suppressed SPP losses as shown in Figure A-11. For the estimation, temperature-dependent conductivity values of the metal are used to scale the collision frequency (γ) of the free electrons at a cryogenic temperature[146-148]. The scaling factor represented by γ/γ_{300K}. The coupling efficiency is deffined as $\beta = \Gamma_{pl}/\Gamma_{tot}$, where Γ_{pl} and Γ_{tot} denote the guided decay rate and the total decay rate, respectively[120,133]. The cooperativity defined as $\beta/(1-\beta)$.

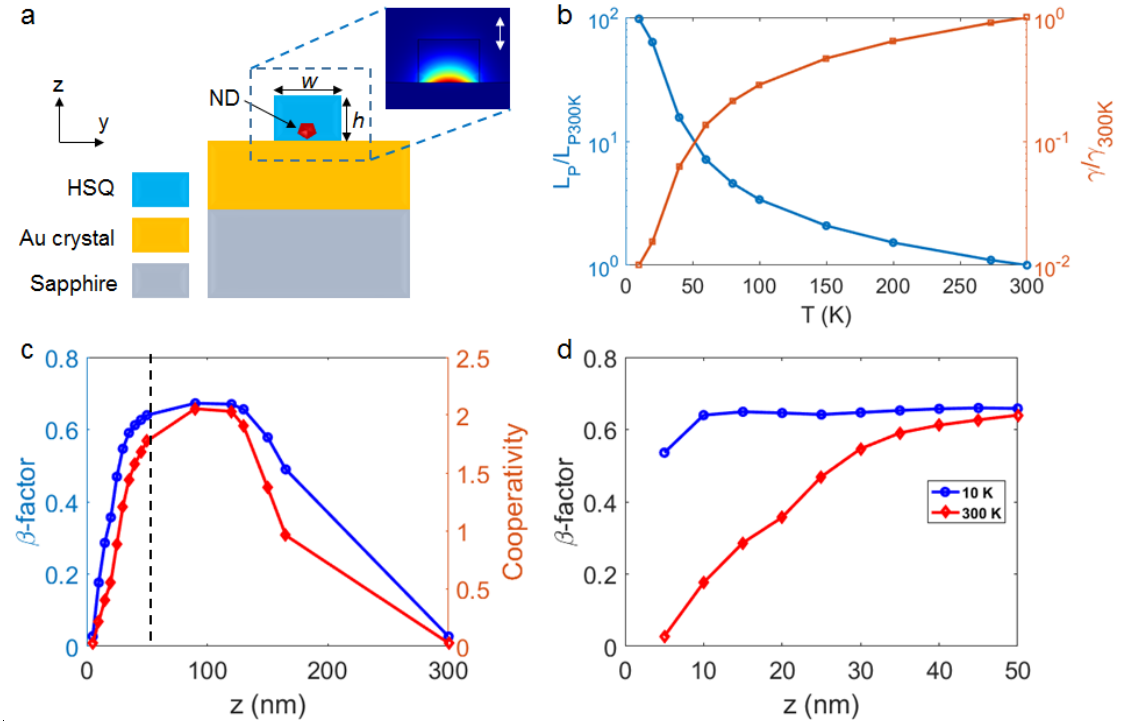

Figure A-11 Simulated characteristics of the DLSPP mode coupled to a GeV QE. (a) Schematic of the device layout (cross section). (b) Temperature dependency results for the propagation length (L_p) of the DLSPP mode at λ=602 nm (ZPL, GeV). For the estimation, temperature-dependent resistivity values of the metal are used to scale the collision frequency (γ) of the free electrons at a cryogenic temperature[146-148]. (c) Simulated coupling efficiency (β-factor) and cooperativity. (d) Simulated coupling efficiency at low temperature (10 K, blue line) is compared with room temperature results (red line), indicating larger β-factor at low temperature (for z<50 nm region) due to the suppressed SPP losses.

For the estimation, temperature-dependent resistivity values of the metal (as shown in table A-1) are used to scale the collision frequency (γ) of the free electrons at a cryogenic temperature[146-148]. Table A-1 gives the electrical resistivity, in units of 10^{-8} Ω·m, for

polycrystalline samples of Au and Ag as a function of temperature. The low-temperature values refer to samples of specified purity and treatment as the electrical resistivity at low temperatures (especially below 50 K) is extremely sensitive to sample purity[149].

Table A-1 Electrical resistivity of pure metals. The electrical resistivity values are in units of 10^{-8} Ω·m (from ref 149).

T/K	Gold	Silver
1	0.0220	0.00100
10	0.0226	0.00115
20	0.035	0.0042
40	0.141	0.0539
60	0.308	0.162
80	0.481	0.289
100	0.650	0.418
150	1.061	0.726
200	1.462	1.029
273	2.051	1.467
293	2.214	1.587
298	2.255	1.617
300	2.271	1.629
400	3.107	2.241
500	3.97	2.87

List of publications

The following publications have resulted from this PhD project.

- Journal articles

1. H. Siampour, O. Wang, V. A. Zenin, S. Boroviks, P. Siyushev, Y. Yang, V. A. Davydov, L. F. Kulikova, V. N. Agafonov, N. A. Mortensen, F. Jelezko and S. I. Bozhevolnyi, Unidirectional single-photon emission from germanium-vacancy zero-phonon lines: Deterministic emitter-waveguide interfacing at plasmonic hot spots, *arXiv:1903.05446* (2019)

2. H. Siampour, S. Kumar, V. A. Davydov, L. F. Kulikova, V. N. Agafonov and S. I. Bozhevolnyi, On-chip excitation of single germanium vacancies in nanodiamonds embedded in plasmonic waveguides, *Light: Science & Applications* **7**, 61 (2018)

3. H. Siampour, S. Kumar and S. I. Bozhevolnyi, Chip-integrated plasmonic cavity-enhanced single nitrogen-vacancy center emission, *Nanoscale* **9**, 17902-17908 (2017)

4. H. Siampour, S. Kumar and S. I. Bozhevolnyi, Nanofabrication of plasmonic circuits containing single photon sources, *ACS Photonics* **4**, 1879-1884 (2017)

- Conference contributions

1. H. Siampour, O. Wang, V. A. Davydov, V. N. Agafonov, F. Jelezko, and S.I. Bozhevolnyi, Nanophotonics platform for cavity QED with diamond nanocrystals, *Quantum Nanophotonics, Benasque, Spain, 2019, Mar 17-23* (Oral)

2. H. Siampour, O. Wang, V.A. Zenin, S. Boroviks, P. Siyushev, Y. Yang, V.A. Davydov, L.F. Kulikova, V.N. Agafonov, N.A. Mortensen, F. Jelezko and S.I. Bozhevolnyi, A unidirectional surface plasmon coupler for strong interface with integrated quantum emitters, *7th International Topical Meeting on Nanophotonics and Metamaterials (NANOMETA), Seefeld, Austria, 2019, January 3-6* (Best Poster Award)

3. V.A. Zenin, H. Siampour, S.I. Bozhevolnyi, and N.A. Mortensen, Quantitative near-field characterization of dielectric-loaded SPP waveguides: phase-resolved measurements, Fourier analysis, and fitting, *9th International Conference on Surface Plasmon Photonics (SPP), Copenhagen, Denmark, 2019, May 26-31*

4. H. Siampour and S.I. Bozhevolnyi, Plasmon-based integrated quantum platform containing bright fluorescent nanodiamonds, *Prospects of Plasmonics for Quantum Technologies, Aspenäs, Sweden, 2018, June 25-27*

5. H. Siampour, S. Kumar and S.I. Bozhevolnyi, Controlled excitation of diamond color centers using low-loss dielectric-loaded surface plasmon polariton waveguides, *Proc. SPIE, Quantum Technologies, SPIE Photonics Europe, Strasbourg, France, 2018, March 29- April 2* (Oral)

6. H. Siampour, Slam on bit rate, *Science Slam, 662. WE-Heraeus-Seminar on Quantum Networks-from building blocks to application, Physikzentrum Bad Honnef, Germany, 2018, February, 5-7* (Science Slam Award)

7. H. Siampour, S. Kumar and S.I. Bozhevolnyi, On-chip plasmonic cavity-enhanced spontaneous emission rate at the zero-phonon line, *662. WE-Heraeus-Seminar on Quantum Networks-from building blocks to application, Physikzentrum Bad Honnef, Germany, 2018, February 5-7*

8. H. Siampour, S. Kumar and S.I. Bozhevolnyi, On-chip plasmonic cavity-enhanced quantum emitters, *24th Central European Workshop on Quantum Optics, Lyngby, Denmark, 2017, June 26-30*

9. H. Siampour, S. Kumar and S.I. Bozhevolnyi, Deterministic fabrication of dielectric loaded waveguides coupled to single nitrogen vacancy centers in nanodiamonds, *6th International Topical Meeting on Nanophotonics and Metamaterials, Seefeld, Austria, 2017, January 4-7*

Bibliography

1. Moore, G.E. Cramming More Components Onto Integrated Circuits. *Proceedings of the IEEE* **86**, 82-85 (1998).
2. Madou, M.J. *Fundamentals of microfabrication: the science of miniaturization*, (CRC press, 2002).
3. Sah, C.-T. *Fundamentals of Solid State Electronics*, -1 (World Scientific Publishing Company, 1996).
4. Li, Y. *Microelectronic applications of chemical mechanical planarization*, (John Wiley & Sons, 2008).
5. Chen, G. et al. Predictions of CMOS compatible on-chip optical interconnect. *Integration* **40**, 434-446 (2007).
6. Haurylau, M. et al. On-Chip Optical Interconnect Roadmap: Challenges and Critical Directions. *IEEE Journal of Selected Topics in Quantum Electronics* **12**, 1699-1705 (2006).
7. Zia, R., Schuller, J.A., Chandran, A. & Brongersma, M.L. Plasmonics: the next chip-scale technology. *Materials Today* **9**, 20-27 (2006).
8. Brongersma, M.L. & Shalaev, V.M. The Case for Plasmonics. *Science* **328**, 440-441 (2010).
9. Gramotnev, D.K. & Bozhevolnyi, S.I. Plasmonics beyond the diffraction limit. *Nat Photon* **4**, 83 (2010).
10. Ozbay, E. Plasmonics: Merging Photonics and Electronics at Nanoscale Dimensions. *Science* **311**, 189-193 (2006).

11. Jackson, J.D. *Classical electrodynamics*, (John Wiley, 1975).

12. Raether, H. *Surface Plasmons on Smooth and Rough Surfaces and on Gratings*, (Springer-Verlag, 1988).

13. Siampour, H. & Dan, Y. Si nanowire phototransistors at telecommunication wavelengths by plasmon-enhanced two-photon absorption. *Optics Express* **24**, 4601-4609 (2016).

14. Guan, B. et al. Nanoscale Nitrogen Doping in Silicon by Self-Assembled Monolayers. *Scientific Reports* **5**, 12641 (2015).

15. Tan, S.L., Zhao, X. & Dan, Y. High-sensitivity silicon nanowire phototransistors. in *SPIE NanoScience + Engineering* Vol. 9170 (SPIE, 2014).

16. Verhagen, E., Spasenović, M., Polman, A. & Kuipers, L. Nanowire Plasmon Excitation by Adiabatic Mode Transformation. *Physical Review Letters* **102**, 203904 (2009).

17. Dionne, J.A., Lezec, H.J. & Atwater, H.A. Highly Confined Photon Transport in Subwavelength Metallic Slot Waveguides. *Nano Letters* **6**, 1928-1932 (2006).

18. Steinberger, B. et al. Dielectric stripes on gold as surface plasmon waveguides: Bends and directional couplers. *Applied Physics Letters* **91**, 081111 (2007).

19. Holmgaard, T. & Bozhevolnyi, S.I. Theoretical analysis of dielectric-loaded surface plasmon-polariton waveguides. *Physical Review B* **75**, 12 (2007).

20. Krasavin, A.V. & Zayats, A.V. Silicon-based plasmonic waveguides. *Optics Express* **18**, 11791-11799 (2010).

21. Briggs, R.M., Grandidier, J., Burgos, S.P., Feigenbaum, E. & Atwater, H.A. Efficient Coupling between Dielectric-Loaded Plasmonic and Silicon Photonic Waveguides. *Nano Letters* **10**, 4851-4857 (2010).

22. Jung, K., Teixeira, F.L. & Reano, R.M. Surface Plasmon Coplanar Waveguides: Mode Characteristics and Mode Conversion Losses. *IEEE Photonics Technology Letters* **21**, 630-632 (2009).

23. Bozhevolnyi, S.I., Volkov, V.S., Devaux, E., Laluet, J.-Y. & Ebbesen, T.W. Channel plasmon subwavelength waveguide components including interferometers and ring resonators. *Nature* **440**, 508 (2006).

24. Pile, D.F.P. et al. Theoretical and experimental investigation of strongly localized plasmons on triangular metal wedges for subwavelength waveguiding. *Applied Physics Letters* **87**, 061106 (2005).

25. Moreno, E., Rodrigo, S.G., Bozhevolnyi, S.I., Martín-Moreno, L. & García-Vidal, F.J. Guiding and Focusing of Electromagnetic Fields with Wedge Plasmon Polaritons. *Physical Review Letters* **100**, 023901 (2008).

26. Sorger, V.J. et al. Experimental demonstration of low-loss optical waveguiding at deep sub-wavelength scales. *Nature Communications* **2**, 331 (2011).

27. Oulton, R.F., Sorger, V.J., Genov, D.A., Pile, D.F.P. & Zhang, X. A hybrid plasmonic waveguide for subwavelength confinement and long-range propagation. *Nature Photonics* **2**, 496 (2008).

28. Han, Z. & Bozhevolnyi, S.I. Radiation guiding with surface plasmon polaritons. *Reports on Progress in Physics* **76**, 016402 (2013).

29. Buckley, R. & Berini, P. Figures of merit for 2D surface plasmon waveguides and application to metal stripes. *Optics Express* **15**, 12174-12182 (2007).

30. Gosciniak, J., Holmgaard, T. & Bozhevolnyi, S.I. Theoretical Analysis of Long-Range Dielectric-Loaded Surface Plasmon Polariton Waveguides. *Journal of Lightwave Technology* **29**, 1473-1481 (2011).

31. Sorger, V.J., Oulton, R.F., Ma, R.-M. & Zhang, X. Toward integrated plasmonic circuits. *MRS Bulletin* **37**, 728-738 (2012).

32. Shalf, J.M. & Leland, R. Computing beyond Moore's Law. *Computer* **48**, 14-23 (2015).

33. Bennett, C.H. & DiVincenzo, D.P. Quantum information and computation. *Nature* **404**, 247-255 (2000).

34. Bozhevolnyi, S.I., Martin-Moreno, L. & Garcia-Vidal, F. *Quantum Plasmonics*, (Springer Switzerland, 2017).

35. Tame, M.S. et al. Quantum plasmonics. *Nat Phys* **9**, 329-340 (2013).

36. Xu, D. et al. Quantum plasmonics: new opportunity in fundamental and applied photonics. *Advances in Optics and Photonics* **10**, 703-756 (2018).

37. Bozhevolnyi, S.I. & Mortensen, N.A. Plasmonics for emerging quantum technologies. *Nanophotonics* **6**, 1185-1188 (2017).

38. Johannes, T. A Decade of Economic Stagnation Looms as Moore's Law Ends While Quantum Computing Is Developed. in *Philosophy Workout* (philosophyworkout.blogspot.com, 2016).

39. Jacob, Z. & Shalaev, V.M. Plasmonics Goes Quantum. *Science* **334**, 463-464 (2011).

40. Bozhevolnyi, S.I. & Khurgin, J.B. The case for quantum plasmonics. *Nat Photon* **11**, 398-400 (2017).

41. Kolesov, R. et al. Wave-particle duality of single surface plasmon polaritons. *Nat Phys* **5**, 470-474 (2009).

42. Akimov, A.V. et al. Generation of single optical plasmons in metallic nanowires coupled to quantum dots. *Nature* **450**, 402-406 (2007).

43. Bermudez-Urena, E. et al. Coupling of individual quantum emitters to channel plasmons. *Nat Commun* **6**, 7883 (2015).

44. Di Martino, G. et al. Quantum Statistics of Surface Plasmon Polaritons in Metallic Stripe Waveguides. *Nano Letters* **12**, 2504-2508 (2012).

45. Altewischer, E., van Exter, M.P. & Woerdman, J.P. Plasmon-assisted transmission of entangled photons. *Nature* **418**, 304-306 (2002).

46. Huck, A. et al. Demonstration of Quadrature-Squeezed Surface Plasmons in a Gold Waveguide. *Physical Review Letters* **102**, 4 (2009).

47. Fakonas, J.S., Lee, H., Kelaita, Y.A. & Atwater, H.A. Two-plasmon quantum interference. *Nat Photon* **8**, 317-320 (2014).

48. Kress, S.J.P. et al. Wedge Waveguides and Resonators for Quantum Plasmonics. *Nano Letters* **15**, 6267-6275 (2015).

49. Wu, X. et al. On-Chip Single-Plasmon Nanocircuit Driven by a Self-Assembled Quantum Dot. *Nano Letters* **17**, 4291-4296 (2017).

50. Gosciniak, J. et al. Thermo-optic control of dielectric-loaded plasmonic waveguide components. *Optics Express* **18**, 1207-1216 (2010).

51. Holmgaard, T., Gosciniak, J. & Bozhevolnyi, S.I. Long-range dielectric-loaded surface plasmon-polariton waveguides. *Optics Express* **18**, 23009-23015 (2010).

52. Smith, C.L.C., Stenger, N., Kristensen, A., Mortensen, N.A. & Bozhevolnyi, S.I. Gap and channeled plasmons in tapered grooves: a review. *Nanoscale* **7**, 9355-9386 (2015).

53. Robinson, J.T., Manolatou, C., Chen, L. & Lipson, M. Ultrasmall Mode Volumes in Dielectric Optical Microcavities. *Physical Review Letters* **95**, 143901 (2005).

54. Benson, O. Assembly of hybrid photonic architectures from nanophotonic constituents. *Nature* **480**, 193-199 (2011).

55. Englund, D. et al. Deterministic Coupling of a Single Nitrogen Vacancy Center to a Photonic Crystal Cavity. *Nano Letters* **10**, 3922-3926 (2010).

56. Kolchin, P. et al. High Purcell Factor Due To Coupling of a Single Emitter to a Dielectric Slot Waveguide. *Nano Letters* **15**, 464-468 (2014).

57. Acín, A. et al. The quantum technologies roadmap: a European community view. *New Journal of Physics* **20**, 080201 (2018).

58. Afzelius, M., Gisin, N. & de Riedmatten, H. Quantum memory for photons. *Physics Today* **68**, 42-47 (2015).

59. Distante, E. et al. Storing single photons emitted by a quantum memory on a highly excited Rydberg state. *Nature communications* **8**, 14072-14072 (2017).

60. Reiserer, A., Ritter, S. & Rempe, G. Nondestructive Detection of an Optical Photon. *Science* **342**, 1349 (2013).

61. Raymer, M.G. & Srinivasan, K. Manipulating the color and shape of single photons. *Physics Today* **65**, 32-37 (2012).

62. Walker, T. et al. Long-Distance Single Photon Transmission from a Trapped Ion via Quantum Frequency Conversion. *Physical Review Letters* **120**, 203601 (2018).

63. Brassard, G., Chuang, I., Lloyd, S. & Monroe, C. Quantum computing. *Proceedings of the National Academy of Sciences* **95**, 11032 (1998).

64. Cour, B.R.L. & Ott, G.E. Signal-based classical emulation of a universal quantum computer. *New Journal of Physics* **17**, 053017 (2015).

65. Jozsa, R. & Linden, N. On the role of entanglement in quantum-computational speed-up. *Proceedings of the Royal Society of London. Series A: Mathematical, Physical and Engineering Sciences* **459**, 2011-2032 (2003).

66. Bennett, C.H. & DiVincenzo, D.P. Quantum information and computation. *Nature* **404**, 247 (2000).

67. Jozsa, R. Quantum algorithms and the Fourier transform. *Proceedings of the Royal Society of London. Series A: Mathematical, Physical and Engineering Sciences* **454**, 323-337 (1998).

68. Ekert, A.K. Quantum cryptography based on Bell's theorem. *Physical Review Letters* **67**, 661-663 (1991).

69. Aharonovich, I., Englund, D. & Toth, M. Solid-state single-photon emitters. *Nat Photon* **10**, 631-641 (2016).

70. Fattal, D. Stanford University (2005).

71. Santori, C., Fattal, D., Vučković, J., Solomon, G.S. & Yamamoto, Y. Indistinguishable photons from a single-photon device. *Nature* **419**, 594-597 (2002).

72. Loudon, R. *The Quantum Theory of Light*, (Oxford University Press, 2000).

73. Hong, C.K., Ou, Z.Y. & Mandel, L. Measurement of subpicosecond time intervals between two photons by interference. *Physical Review Letters* **59**, 2044-2046 (1987).

74. Slachter, A. Single Photon Emitters. (University of Groningen, 2005).

75. Bacon, D.M. Decoherence, Control, and Symmetry in Quantum Computers. *arXiv:quant-ph/0305025* (2003).

76. Saeedi, K. et al. Room-Temperature Quantum Bit Storage Exceeding 39 Minutes Using Ionized Donors in Silicon-28. *Science* **342**, 830 (2013).

77. Amoroso, R.L. *Universal Quantum Computing: Supervening Decoherence - Surmounting Uncertainty*, (World Scientific, 2017).

78. Childress, L. & Hanson, R. Diamond NV centers for quantum computing and quantum networks. *MRS Bulletin* **38**, 134-138 (2013).

79. Thompson, J.D. et al. Coupling a Single Trapped Atom to a Nanoscale Optical Cavity. *Science* **340**, 1202 (2013).

80. Gullans, M. et al. Nanoplasmonic Lattices for Ultracold Atoms. *Physical Review Letters* **109**, 235309 (2012).

81. Tiecke, T.G. et al. Nanophotonic quantum phase switch with a single atom. *Nature* **508**, 241 (2014).

82. Lodahl, P. et al. Controlling the dynamics of spontaneous emission from quantum dots by photonic crystals. *Nature* **430**, 654 (2004).

83. Badolato, A. et al. Deterministic Coupling of Single Quantum Dots to Single Nanocavity Modes. *Science* **308**, 1158-1161 (2005).

84. Luo, Y. et al. Deterministic coupling of site-controlled quantum emitters in monolayer WSe2 to plasmonic nanocavities. *Nature Nanotechnology* **13**, 1137-1142 (2018).

85. Schnauber, P. et al. Deterministic Integration of Quantum Dots into on-Chip Multimode Interference Beamsplitters Using in Situ Electron Beam Lithography. *Nano Letters* **18**, 2336-2342 (2018).

86. Thorgrimsson, B. et al. Extending the coherence of a quantum dot hybrid qubit. *npj Quantum Information* **3**, 32 (2017).

87. Sipahigil, A. et al. An integrated diamond nanophotonics platform for quantum-optical networks. *Science* **354**, 847-850 (2016).

88. Balasubramanian, G. et al. Ultralong spin coherence time in isotopically engineered diamond. *Nature Materials* **8**, 383 (2009).

89. Doherty, M.W. et al. The nitrogen-vacancy colour centre in diamond. *Physics Reports* **528**, 1-45 (2013).

90. Schröder, T., Schell, A.W., Kewes, G., Aichele, T. & Benson, O. Fiber-Integrated Diamond-Based Single Photon Source. *Nano Letters* **11**, 198-202 (2011).

91. Kurtsiefer, C., Mayer, S., Zarda, P. & Weinfurter, H. Stable Solid-State Source of Single Photons. *Physical Review Letters* **85**, 290-293 (2000).

92. Sharma, S., Hovde, D., Douglas, H.B. & Alghannam, F. Imaging Strain and Electric Fields in NV Ensembles using Stark ShiftMeasurements. *arXiv:1802.08767* (2018).

93. Chu, Y. & Lukin, M.D. Quantum optics with nitrogen-vacancy centers in diamond. *arXiv:1504.05990* (2015).

94. Sipahigil, A. & Lukin, M.D. Quantum optics with diamond color centers coupled to nanophotonic devices. *arXiv:1712.06693* (2017).

95. Rogers, L.J. et al. Electronic structure of the negatively charged silicon-vacancy center in diamond. *Physical Review B* **89**, 235101 (2014).

96. Bhaskar, M.K. et al. Quantum Nonlinear Optics with a Germanium-Vacancy Color Center in a Nanoscale Diamond Waveguide. *Physical Review Letters* **118**, 223603 (2017).

97. Iwasaki, T. et al. Tin-Vacancy Quantum Emitters in Diamond. *Physical Review Letters* **119**, 253601 (2017).

98. Trusheim, M.E. et al. Lead-Related Quantum Emitters in Diamond. *arXiv:1805.12202* (2018).

99. Hepp, C. et al. Electronic Structure of the Silicon Vacancy Color Center in Diamond. *Physical Review Letters* **112**, 036405 (2014).

100. Ditalia Tchernij, S. et al. Single-Photon Emitters in Lead-Implanted Single-Crystal Diamond. *ACS Photonics* **5**, 4864-4871 (2018).

101. Sipahigil, A. et al. Indistinguishable Photons from Separated Silicon-Vacancy Centers in Diamond. *Physical Review Letters* **113**, 113602 (2014).

102. Rogers, L.J. et al. Single SiV Centers in Low-Strain Nanodiamonds with Bulklike Spectral Properties and Nanomanipulation Capabilities. *Physical Review Applied* **11**, 024073 (2019).

103. Pingault, B. et al. Coherent control of the silicon-vacancy spin in diamond. *Nature Communications* **8**, 15579 (2017).

104. Siyushev, P. et al. Optical and microwave control of germanium-vacancy center spins in diamond. *Physical Review B* **96**, 081201 (2017).

105. Sukachev, D.D. et al. Silicon-Vacancy Spin Qubit in Diamond: A Quantum Memory Exceeding 10 ms with Single-Shot State Readout. *Physical Review Letters* **119**, 223602 (2017).

106. Trusheim, M.E. et al. Lead-related quantum emitters in diamond. *Physical Review B* **99**, 075430 (2019).

107. Babinec, T.M. et al. A diamond nanowire single-photon source. *Nature Nanotechnology* **5**, 195 (2010).

108. Evans, R.E. et al. Photon-mediated interactions between quantum emitters in a diamond nanocavity. *Science* **362**, 662 (2018).

109. Rogers, L.J. et al. Single SiV centers in low-strain nanodiamonds with bulk-like spectral properties and nano-manipulation capabilities. *arXiv:1802.03588* (2018).

110. Szenes, A. et al. Improved emission of SiV diamond color centers embedded into concave plasmonic core-shell nanoresonators. *Scientific Reports* **7**, 13845 (2017).

111. Elke, N. et al. Low-temperature investigations of single silicon vacancy colour centres in diamond. *New Journal of Physics* **15**, 043005 (2013).

112. Hoang, T.B., Akselrod, G.M. & Mikkelsen, M.H. Ultrafast Room-Temperature Single Photon Emission from Quantum Dots Coupled to Plasmonic Nanocavities. *Nano Letters* **16**, 270-275 (2016).

113. Boroviks, S. et al. Interference in edge-scattering from monocrystalline gold flakes [Invited]. *Optical Materials Express* **8**, 3688-3697 (2018).

114. Clark, C.D., Kanda, H., Kiflawi, I. & Sittas, G. Silicon defects in diamond. *Physical Review B* **51**, 16681-16688 (1995).

115. Iwasaki, T. et al. Germanium-Vacancy Single Color Centers in Diamond. *Scientific Reports* **5**, 12882 (2015).

116. Jahnke, K.D. et al. Electron–phonon processes of the silicon-vacancy centre in diamond. *New Journal of Physics* **17**, 043011 (2015).

117. Humphreys, P.C. et al. Deterministic delivery of remote entanglement on a quantum network. *Nature* **558**, 268-273 (2018).

118. Wehner, S., Elkouss, D. & Hanson, R. Quantum internet: A vision for the road ahead. *Science* **362**, eaam9288 (2018).

119. Bogdanov, S.I. et al. Ultrabright Room-Temperature Sub-Nanosecond Emission from Single Nitrogen-Vacancy Centers Coupled to Nanopatch Antennas. *Nano Letters* **18**, 4837-4844 (2018).

120. Chen, Y., Nielsen, T.R., Gregersen, N., Lodahl, P. & Mørk, J. Finite-element modeling of spontaneous emission of a quantum emitter at nanoscale proximity to plasmonic waveguides. *Physical Review B* **81**, 125431 (2010).

121. Perera, C.S., Vernon, K.C. & Mcleod, A. Simulations of the spontaneous emission of a quantum dot near a gap plasmon waveguide. *Journal of Applied Physics* **115**, 054314 (2014).

122. Palik, E. *Handbook of Optical Constants of Solids*, (Academic Press, 1985).

123. Davydov, V.A. et al. Production of nano- and microdiamonds with Si-V and N-V luminescent centers at high pressures in systems based on mixtures of hydrocarbon and fluorocarbon compounds. *JETP Letters* **99**, 585-589 (2014).

124. Wang, C.-Y. et al. Giant colloidal silver crystals for low-loss linear and nonlinear plasmonics. *Nature Communications* **6**, 7734 (2015).

125. Kumar, S., Huck, A. & Andersen, U.L. Efficient Coupling of a Single Diamond Color Center to Propagating Plasmonic Gap Modes. *Nano Letters* **13**, 1221-1225 (2013).

126. Siampour, H., Kumar, S. & Bozhevolnyi, S.I. Nanofabrication of Plasmonic Circuits Containing Single Photon Sources. *ACS Photonics* **4**, 1879-1884 (2017).

127. Siampour, H., Kumar, S. & Bozhevolnyi, S.I. Chip-integrated plasmonic cavity-enhanced single nitrogen-vacancy center emission. *Nanoscale* **9**, 17902-17908 (2017).

128. Holmgaard, T., Chen, Z., Bozhevolnyi, S.I., Markey, L. & Dereux, A. Design and Characterization of Dielectric-Loaded Plasmonic Directional Couplers. *Journal of Lightwave Technology* **27**, 5521-5528 (2009).

129. López-Tejeira, F. et al. Efficient unidirectional nanoslit couplers for surface plasmons. *Nature Physics* **3**, 324 (2007).

130. Söllner, I. et al. Deterministic photon–emitter coupling in chiral photonic circuits. *Nature Nanotechnology* **10**, 775 (2015).

131. Lodahl, P. et al. Chiral quantum optics. *Nature* **541**, 473 (2017).

132. Barik, S. et al. A topological quantum optics interface. *Science* **359**, 666 (2018).

133. Siampour, H. et al. On-chip excitation of single germanium vacancies in nanodiamonds embedded in plasmonic waveguides. *Light: Science & Applications* **7**, 61 (2018).

134. Faraon, A., Barclay, P.E., Santori, C., Fu, K.-M.C. & Beausoleil, R.G. Resonant enhancement of the zero-phonon emission from a colour centre in a diamond cavity. *Nat Photon* **5**, 301-305 (2011).

135. Faraon, A., Santori, C., Huang, Z., Acosta, V.M. & Beausoleil, R.G. Coupling of Nitrogen-Vacancy Centers to Photonic Crystal Cavities in Monocrystalline Diamond. *Physical Review Letters* **109**, 033604 (2012).

136. de Leon, N.P. et al. Tailoring Light-Matter Interaction with a Nanoscale Plasmon Resonator. *Physical Review Letters* **108**, 226803 (2012).

137. Thiering, G. & Gali, A. Ab Initio Magneto-Optical Spectrum of Group-IV Vacancy Color Centers in Diamond. *Physical Review X* **8**, 021063 (2018).

138. Chen, Y. et al. Efficient interfacing photonic and long-range dielectric-loaded plasmonic waveguides. *Optics Express* **23**, 9100-9108 (2015).

139. Kumar, A. et al. Dielectric-loaded plasmonic waveguide components: Going practical. *Laser & Photonics Reviews* **7**, 938-951 (2013).

140. Binder, J.M. et al. Qudi: a modular python suite for experiment control and data processing. *SoftwareX* **6**, 85-90 (2017).

141. Brust, M., Walker, M., Bethell, D., Schiffrin, D.J. & Whyman, R. Synthesis of thiol-derivatised gold nanoparticles in a two-phase Liquid–Liquid system. *Journal of the Chemical Society, Chemical Communications*, 801-802 (1994).

142. Andryieuski, A. et al. Direct Characterization of Plasmonic Slot Waveguides and Nanocouplers. *Nano Letters* **14**, 3925-3929 (2014).

143. Zenin, V.A., Malureanu, R., Radko, I.P., Lavrinenko, A.V. & Bozhevolnyi, S.I. Near-field characterization of bound plasmonic modes in metal strip waveguides. *Optics Express* **24**, 4582-4590 (2016).

144. Zenin, V.A. et al. Hybrid plasmonic waveguides formed by metal coating of dielectric ridges. *Optics Express* **25**, 12295-12302 (2017).

145. Siampour, H. et al. Unidirectional single-photon emission from germanium-vacancy zero-phonon lines: Deterministic emitter-waveguide interfacing at plasmonic hot spots. *arXiv:1903.05446* (2019).

146. Hill, M.T. et al. Lasing in metallic-coated nanocavities. *Nature Photonics* **1**, 589 (2007).

147. Seo, M.-K., Kwon, S.-H., Ee, H.-S. & Park, H.-G. Full Three-Dimensional Subwavelength High-Q Surface-Plasmon-Polariton Cavity. *Nano Letters* **9**, 4078-4082 (2009).

148. Kim, M.-K. et al. Low-loss surface-plasmonic nanobeam cavities. *Optics Express* **18**, 11089-11096 (2010).

149. Lide, D.R. *CRC Handbook of Chemistry and Physics*, (CRC Press, 2005).